

https://dspace.org/

Hunting the hidden: exploring different dark matter scenarios

Prat, Clarisse

2025
University of the Witwatersrand, Johannesburg
https://hdl.handle.net/10539/50285
Prat, Clarisse. (2025). Hunting the hidden: exploring different dark matter scenarios [Master's dissertation, University of the Witwatersrand, Johannesburg]. WIReDSpace. https://hdl.handle.net/10539/50285

Downloaded from a DSpace repository. https://dspace.org/



Hunting the hidden:

exploring different dark matter scenarios

Clarisse Prat
2331957

School of Physics

Supervisor: Professor Deepak Kar

November 14, 2025

Declaration

I, Clarisse Prat, student number 2331957, am a registered student for the Master of Science (Physics) degree in the academic year 2025. I hereby declare the following:

- I am aware that plagiarism, the use of someone else's work without their permission and/or without acknowledging the original source, is wrong.
- I have not used generative AI in any of the work presented here.
- I confirm that all the work submitted for assessment for the above course is my own unaided work except where I have explicitly indicated otherwise.
- I have followed the required conventions in referencing the thoughts and ideas of others.
- I understand that the University of the Witwatersrand may take disciplinary action against me if there is a belief that this is not my own unaided work or that I have failed to acknowledge the source of the ideas of words in my writing.

Clarisse Prat

10.11.2025

Abstract

This thesis explores searches for Dark Matter at colliders through a phenomenological and experimental approach. Following an introduction to the Standard Model and Beyond the Standard Model theories relevant to the work in this thesis, the Large Hadron Collider and the ATLAS experiment are introduced. Important components of event generation are discussed, along with specifics of the event generators and analysis tools used.

The first work completed and shown is work done as a Summer Student at CERN in 2024, working on the ATLAS Trigger Menu. This is followed by the work done as part of an ATLAS search for a new hypothetical particle, using simulated events based on Run 2 data and 139 fb^{-1} of data, as well as a discussion of the model it is based on.

The last two parts discuss phenomenological studies performed over the past months, and are relevant in the context of Dark Matter searches in colliders, specifically at the Large Hadron Collider.

Acknowledgements

Doing my Masters in was never a question: I started my undergrad knowing that I wanted to end up working for one of the collaborations based at CERN, and was adamant on getting there. The road has not been easy, but the immense pride and joy I feel make every late-night and difficult discussion worth it. Completing this would not have been possible without the help and support of the following people, whom I would like to thank.

Firstly, my supervisor Deepak. I walked into your office three years ago and refused to leave before you agreed to be my supervisor. You have seen me at my worst, and at my best, yet your support has never wavered. You have helped me strive for excellence, but have been quick to note when I should slow down and focus on maintaining balance. Your encouragement after I struggled for days with computer setups and issues helped me stay on track, even though I was very close to logging out of LXPlus forever. You fostered an environment where I felt seen and respected, and empowered me to speak my mind when I felt it necessary. I am incredibly grateful for your guidance throughout this process (even though you were on sabbatical for a year) and have you to thank for the path that has opened up for me. You have been an incredible supervisor, mentor and ultimately a friend.

Next, the PhD student and postdoc that I jokingly call my real bosses, Hannah and Sukanya. Hannah, thank you for taking me onto the analysis and guiding me through TWiki pages. You brightened up most of our meetings, and I knew that I could always count on you if I had any issues. Sukanya, thank you for always being there to guide me through the tougher bits, and for also providing me countless links that I definitely read.

Then, Stefanie and Sofia. Thank you for choosing me to be your Summer Student and showing me that Trigger operations is actually fun. My time at CERN was a highlight of the past two years, and I owe it all to you. I look forward to seeing you on JIRA tickets in the future, and recreating our photo-shopped picture at any poster presentation.

Louie and Benjamin. Thank you for coming up with a project that I not only thoroughly enjoyed, but taught me the importance of good code documentation. Louie, you were always there to help with any questions I had, even when we ultimately had to go to Benjamin to figure things out. Working with you has been an immense pleasure, and I look forward to seeing how we can continue collaborating in the future. Benjamin, your kindness and hospitality during my visit in Paris meant a lot to me, and I hope that our paths cross again (although it might not be in a D&D campaign). Thank you both for seeing something in me that lead to the extended project, and supporting me throughout. I would also like to thank Mark in Paris for helping me with my setup, and all three of you for dealing with my ability to anger the computer gods.

To all other academics that I have met through the schools and workshops that I was lucky

enough to attend, specifically CHACAL and MCNet, thank you for showing me a different side to academia: a side where questionable song choices can be made at a karaoke bar, and for letting me ask questions about QCD over a couple of beers.

Moving on to family. None of this would have been possible without the support of my parents. To my mom, who never once let me forget how important I am to her - going so far as to proof-read my thesis. Thank you for sacrificing your time and energy to make sure that I can succeed, and supporting me every step of the way. You raised me to be a confident, strong, smart woman, and thank you for giving me the space to become that. À mon père, merci de me faire comprendre de toujours faire de mon mieux. Merci de me dire que tu es fière de moi, et que je suis une petite Jean-Michel, qui es capable de atteindre mes objectifs et de accèder à mes rêves. Catherine, merci de toujours avoir confiance en moi, et pour tout ce que tu fais pour moi. Madeleine and Estelle, thank you for being there to help me navigate this crazy life, and reminding me that there is life outside of work. I love you guys.

I want to thank the cat I got around the time I joined Deepak's group. Higgs sat on my lap and kept me warm while writing most of my thesis. I could have done this without him, but he made it so much more fun.

Finally, I want to extend my gratitude to the NRF iThemba Labs SA-CERN programme for providing me with the funding to carry out this research. Receiving the Excellence Scholarship allowed me to focus on this research, and without the support that the programme offers I would not have been able to visit CERN.

Contents

Declaration i

Abstract ii

Acknowledgements iii

1 Introduction 1

2 The Standard Model 3
- 2.1 Elementary Particles in the Standard Model . . . 3
  - 2.1.1 Fermions . . . 3
  - 2.1.2 Vector Bosons . . . 4
  - 2.1.3 Higgs Boson . . . 5
  - 2.1.4 Asymptotic Freedom and Confinement . . . 5
- 2.2 The Standard Model Lagrangian . . . 5
  - 2.2.1 The Brout-Englert-Higgs Mechanism . . . 6
  - 2.2.2 Components of the SM Lagrangian . . . 6
- 2.3 Standard Model Interactions . . . 8
  - 2.3.1 Feynman Diagrams and Mandelstam Variables . . . 9
  - 2.3.2 Perturbation Theory and Cross Section Calculations . . . 10
- 2.4 Generating and Analysing Standard Model Processes . . . 11
  - 2.4.1 Matrix-element Generator: MadGraph5 . . . 11
  - 2.4.2 Parton Showering and Hadronisation: Pythia8 . . . 13
  - 2.4.3 Analysis Frameworks: RIVET, MadAnalysis5 and ROOT . . . 14

3 Extending the Standard Model 15
- 3.1 Missing Pieces in the Standard Model . . . 15
  - 3.1.1 The Hierarchy Problem . . . 15
  - 3.1.2 Dark Energy and Dark Matter . . . 16
- 3.2 The Dark Sector . . . 17
  - 3.2.1 Simplified Dark Sector . . . 18
  - 3.2.2 Extended Dark Sector . . . 20
- 3.3 Generating BSM events and Exploring New Models . . . 22
  - 3.3.1 FeynRules . . . 22
  - 3.3.2 Pythia8 Hidden Valley . . . 22
  - 3.3.3 Reinterpretation Using CONTUR and MadAnalysis5 . . . 23

4 The LHC and ATLAS 25

4.1 The Large Hadron Collider . . . 25
4.1.1 Coordinates at the LHC . . . 25
4.2 The ATLAS Detector . . . 26
4.2.1 Inner Detector . . . 26
4.2.2 Calorimeter System . . . 27
4.2.3 Muon Spectrometer . . . 27
4.2.4 Magnet Systems . . . 27
4.3 The ATLAS Trigger System . . . 28
4.3.1 Level-1 Trigger . . . 28
4.3.2 High-Level-Trigger . . . 29
4.3.3 The ATLAS Trigger Menu . . . 30
4.4 Event and Object Reconstruction in ATLAS . . . 30
4.4.1 Jets . . . 30
4.4.2 Electrons and Photons . . . 32
4.4.3 Muons . . . 33
4.4.4 Missing Transverse Momentum . . . 33
4.5 It's All About the Rates or A Summer Working on the Trigger Menu . . . 34
4.5.1 Developing an analysis of rate usage . . . 34
4.5.2 Overlap between Two Streams . . . 34
4.5.3 Unique Contribution of a Chain to a Stream . . . 36
4.5.4 Overlap between Two Chains . . . 37
4.5.5 Unique Rate of a Set of Chains . . . 38
4.5.6 Conclusion . . . 39

5 ATLAS Search for a Maverick Top Partner Decaying to a Dark Photon 40
5.1 Vector-like Quarks . . . 40
5.2 Dark Photons . . . 41
5.3 Theoretical Framework . . . 44
5.4 Lepton Jets in ATLAS . . . 46
5.5 Analysis Strategy . . . 47
5.5.1 Final State Topology and Signal Characteristics . . . 47
5.5.2 Event Generation . . . 48
5.5.3 Object Selection and Event Reconstruction . . . 49
5.5.4 Event Selection . . . 51
5.5.5 Contributing Background Processes . . . 52
5.6 Preliminary Results . . . 52
5.6.1 Muon Studies . . . 53
5.6.2 Kinematic Distributions . . . 59
5.7 Conclusions . . . 61

6 Placing Constraints on a t-Channel Dark Matter Model 63
6.1 Theoretical Framework . . . 64
6.1.1 Minimal Setup . . . 64
6.1.2 Extending using Ideas of Compositeness . . . 65
6.1.3 Final Simplification and Model Setup . . . 66
6.2 Process Generalities and Event Generation . . . 66
6.2.1 The Three Contributing Processes . . . 66
6.2.2 Dependency on the BSM Coupling . . . 67

6.2.3 Event Generation . . . 68
6.3 Results . . . 69
6.3.1 Reduced Parameter Space . . . 69
6.3.2 Extended Parameter Space . . . 71
6.4 Conclusions . . . 74

7 Constraints on Dark-QCD Models **76**
7.1 Theoretical Framework . . . 76
7.2 Novel Detector Final States . . . 77
7.2.1 Dark Jets . . . 79
7.2.2 Semi-Visible Jets . . . 79
7.3 Probing the sensitivity of SVJs to current LHC measurements using the CONTUR toolkit . . . 80
7.3.1 SVJ Generation . . . 80
7.3.2 Constraints on SVJs . . . 81
7.3.3 Summary . . . 86

8 Conclusions **88**

1 Introduction

The Standard Model (SM) of particle physics is an incredible achievement: it is the most well-tested and best predictive theory that theoretical physicists have come up with [1, 2], and attempts to explain all of the interactions between the fundamental particles. After the discovery of the Higgs boson at the Large Hadron Collider (LHC) [3,4], the success of the SM was cemented and accepted as the best theory we have for current achievable energy scales in colliders.

For all of its success, the SM also has very critical missing elements. Observational astronomical evidence shows that Dark Matter (DM) makes up around 27% of the universe [5], but it has not been directly detected by any experiment, and is not accounted for in the SM. DM does not interact via the electroweak or strong force, and so its existence is only inferred by its gravitational effects on baryonic matter [6].

A class of theoretical models in particle physics are trying to expand on the SM to address the issues mentioned above. These Beyond the Standard Model (BSM) theories cover a range of hypothetical solutions to problems in the SM, including the existence of DM. BSM theories can help us understand the nature of DM, and provide a theoretical framework in which DM can be detected indirectly in particle colliders, such as the LHC. These theories open the door to explore the nature of DM in particle colliders, and allows us to study their phenomenology.

The work in this thesis is split into six chapters. The first chapter introduces the SM, discussing the elementary particles and the interactions they experience, before discussing some of the formulations behind this model as well as the representation of different processes. The chapter ends by briefly touching on the event generation process for SM processes, and introduces two useful analysis frameworks. The second chapter is used to explore models and features that are beyond the scope of the SM, discussing the missing pieces in the SM, as well as one of the promising research areas in the field. The chapter then concludes by discussing event generation and simulation for BSM processes. The third introductory chapter discusses the ATLAS experiment and detector, and contains work that was completed as a summer student working on the ATLAS Trigger System in 2024.

The remaining chapters discuss the experimental and phenomenological work that has been completed. The first chapter introduces an ATLAS search for a hypothetical particle that has a novel final state topology in the detector. The chapter discusses the theoretical model on which the search is based, and shows preliminary results for the analysis. The second chapter is a phenomenological study that was completed using a model that has been studied by the LHC DM Working Group, and using different event generation and analysis tools available. The third chapter is a phenomenological study that is specifically geared towards exploring a

novel final state in detectors, based on a specific class of BSM models.

2 The Standard Model

A success of modern physics, the Standard Model (SM) of particle physics provides a unified picture of all elementary particles and the forces between them, excluding gravitational interactions between the particles. First attempts at constructing this unified model started in 1961, with Glashow's attempt to connect the electromagnetic and weak nuclear forces [7]. Gell-Mann [8] and Zweig [9] introduced quarks in 1964, the same year that Greenberg introduced the concept of colour charge [10]. The famed Brout-Englert-Higgs mechanism was developed in 1964 as well, by Brout and Englert [11], Higgs [12, 13] and Guralnik, Hagen and Kibble [14]. In 1967, the Brout-Englert-Higgs mechanism was incorporated into the electroweak interaction by Weinberg [15] and Salam [16], and the development of asymptotic freedom in Quantum Chromodynamics in the 1970s (Gross, Wilzcek [17] and Politzer [18]) brought the model to the form we see it in today.

The development of the theory building up the SM was accompanied by the experimental confirmation of many of its predictions. The observation of neutral currents in the Gargamelle bubble chamber [19], the discovery of the τ lepton in 1975 [20], the bottom quark in 1977 [21], the $W^{\pm}$ and Z bosons in 1983 [22–24] and the top quark in 1995 [25] solidified the validity of the SM.

2.1 Elementary Particles in the Standard Model

The SM consists of seventeen fundamental particles, grouped into two broad categories depending on their spin: fermions, with half-integer spins, and bosons, with integer spins. The fermions are split up into quarks and leptons, each of which have three generations. The bosons are either spin-1 vector bosons, or spin-0 scalar bosons. The only scalar boson in the SM is the Higgs boson.

2.1.1 Fermions

The first group of the fundamental particles are the fermions. Fermions have half-integer spins and obey the Pauli Exclusion Principle, and are split into two categories: the quarks and the leptons. There are six flavours of quarks, shown in the outer upper half of Figure 2.1, and six flavours of leptons, shown in the outer bottom half of the same figure. Quarks can be up-type (up, charm, top quarks), or down-type (down, strange, bottom quarks). The up-type quarks carry a charge of +2/3, while the down-type quarks carry a charge of -1/3. Leptons are split into two groups: the electrically-charged electron, muon and τ in one, and their corresponding neutral (and almost massless) neutrinos in the other.

The fermions are also ordered by masses, in what is called a generation. The first generation

(up and down quarks, electron and electron neutrino) are the lightest, followed by the charm and strange quarks, the muon and the muon neutrino in the second generation. Finally the heaviest particles are in the third generation (top and bottom quarks, the τ and τ-neutrino). Each of these fundamental fermions have an anti-particle associated to them, with the same properties but carrying opposite charge.

The properties of these twelve fermions are determined by the types of forces that they experience. All twelve fermions experience the weak nuclear force and undergo weak interactions. The quarks and the charged leptons all participate in the electromagnetic interaction of Quantum Electrodynamics (QED), while the neutrinos are unaffected due to their lack of electric charge. Quarks are the only particles that carry the colour charge, the Quantum Chromodynamics (QCD) equivalent of electric charge, and are therefore the only particles that experience the strong force.

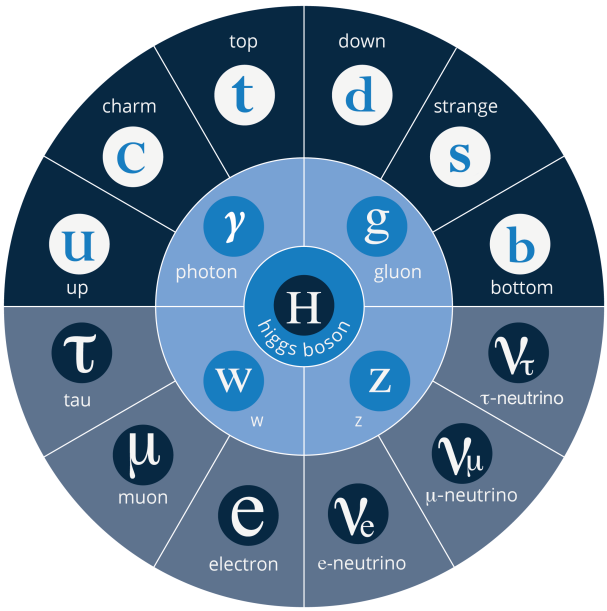


Figure 2.1: The elementary particles comprising the Standard Model [26].

2.1.2 Vector Bosons

The fundamental forces (strong and weak nuclear forces and electromagnetism) are also represented in Figure 2.1, via their force-carrying bosons. Each of the three forces is built on a Quantum Field Theory (QFT) [27], which dictates the interactions between particles and forces, which are mediated by spin-1 gauge bosons. The QED vector-boson is the photon, and the QCD vector-boson is the gluon[1], both of which are massless, shown in the upper smaller circle in Figure 2.1. The W^+ and W^- bosons mediate the weak charged-current interaction, and the weak neutral-current interaction is mediated by the electrically neutral Z boson. The three mediators for the weak interaction are massive, and are indicated in the lower smaller circle in Figure 2.1. The $W^{\pm}$ and Z boson masses are of the order of 100 GeV, which is referred to as the electroweak (EW) scale.

[1]QCD has eight gluon fields, or colour charges, which make up the gluon-octet. Photons are neutral and so there is only one photon field.

2.1.3 Higgs Boson

The Higgs boson was the last missing piece of the SM and was discovered by the ATLAS and CMS collaborations based at the Large Hadron Collider (LHC) in 2012 [3, 4]. The Higgs boson is the only scalar spin-0 boson in the SM and its mass is measured to be 125 GeV [28]. The importance of the discovery of the Higgs boson cannot be overstated: the Brout-Englert-Higgs mechanism [11–13] provides the mechanism by which all particles acquire their mass, and the discovery of the Higgs boson solidified the validity of the SM at energies up to the EW scale.

2.1.4 Asymptotic Freedom and Confinement

Leptons can be observed as free particles, but this is not the case with quarks. Quarks are subject to colour confinement, which means that coloured objects are always confined to colour singlet states and no object with non-zero colour charge can propagate as a free particle [29]. This is due to gluon self-interactions: gluons carry colour charge and interact with each other. When two free quarks are pulled apart, virtual gluons are exchanged.[2] However these gluons experience an attractive force, and the colour field is confined or squeezed together between the two quarks, as seen in Figure 2.2. The energy stored in the field is proportional to the separation of the quarks, and it would take an infinite amount of energy to separate two quarks completely. Colour confinement therefore means that coloured objects group themselves into bound (colourless) hadronic states, with no colour fields between the objects, and so quarks are always confined to colourless hadrons. There are also strong restrictions on the bound states that are able to form from the quark and antiquark combinations: mesons $q\bar{q}$, baryons qqq and anti-baryons $\bar{q}\bar{q}\bar{q}$.

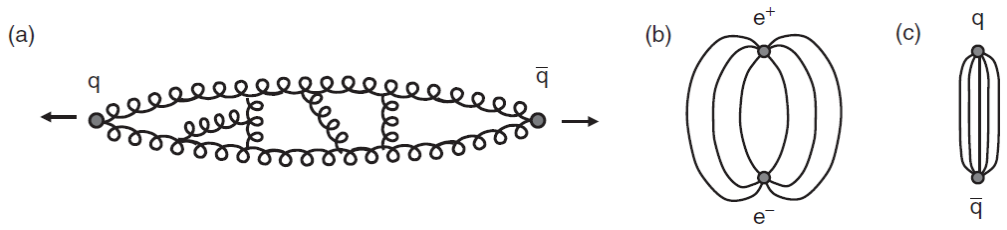


Figure 2.2: (a) shows the exchange of virtual gluons between a free quark (q) and an antiquark ($\bar{q}$), (b) shows the filed lines spreading out as in QED between an electron e^- and a positron e^+, but (c) shows how the field lines are confined in a tunnel between the quarks due to the attractive gluons. Taken from [30].

2.2 The Standard Model Lagrangian

The SM is a QFT comprising of different fields, where particles are excitations of these fields that satisfy the appropriate quantum mechanical field equations. To understand how the particles acquire their masses from the Brout-Englert-Higgs mechanism, a short discussion of Lagrangians and local gauge invariance is needed.

The (classical) Lagrangian formalism describes dynamical systems in terms of generalised coordinates and their time derivatives. For QFTs, the dynamics are described by the Lagrangian

[2] Virtual gluons are excitations of the QCD field and are not physical, detectable particles.

density, where the generalised coordinates and their time derivatives in the Lagrangian are replaced by the fields and their derivatives with respect to each of the four space-time coordinates. An important concept is that of gauge invariance, or gauge theories: the Lagrangian density (hereafter simply referred to as the Lagrangian) is required to be invariant under a set of local transformations which are a symmetry of the theory. These sets of transformations are represented by matrices that act as the generators of the associated symmetry groups.

QCD, QED and the weak interaction are represented by different symmetry groups. $SU(n)$ represents a special unitary group of degree n, which is a Lie group of $n \times n$ matrices with determinant 1. In the SM, QCD is represented by the $SU(3)$ group, while $SU(2)$ represents the electroweak interaction. QCD is an $SU(3)_C$ group, with 8 generators that represent the gluon octet (the eight independent types of gluons). QED and the weak nuclear force arise from the $SU(2)_L \times U(1)_Y$ groups, with 4 generators representing the $W^{\pm}$ and Z bosons, and the photon γ. The SM group can therefore be represented as $SU(3)_C \times SU(2)_L \times U(1)_Y$.

Spontaneous symmetry breaking (SSB) refers to the fact that in making a choice in a vacuum state in a model, the symmetry of the Lagrangian is broken. This is the underlying principle that the Brout-Englert-Higgs mechanism addresses, and subsequently the masses of the EW bosons and the fermions arise.

2.2.1 The Brout-Englert-Higgs Mechanism

The Brout-Englert-Higgs mechanism (hereafter referred to as the Higgs mechanism), is the way by which W and Z bosons acquire mass without breaking the local gauge symmetry of the SM, and it gives mass to the fundamental fermions.

The Higgs potential is given by:

$$V(\phi) = \mu^2 \phi^\dagger \phi + \lambda (\phi^\dagger \phi)^2 \tag{1}$$

and with the choices of $\mu^2 < 0$ and $\lambda > 0$, the potential has an infinite set of degenerate minima satisfying

$$\phi^\dagger \phi = \frac{v^2}{2} = -\frac{\mu^2}{2\lambda} \tag{2}$$

where v is the vacuum expectation value (VEV), and this VEV sets the scale for the masses of the Higgs boson and the gauge bosons. The shape of the potential is the so-called Mexican-hat potential, since there are an infinite number of degenerate minima rotated by the phase rotation, as illustrated in Figure 2.3.

The choice of $\mu^2 < 0$ leads to the non-zero VEV, which in turn leads to SSB. The λ term leads to quartic self-interactions for the scalar fields, and the choice of $\lambda > 0$ is required to have a finite minimum, or vacuum stability. The choice in vacuum state triggers SSB, and then through the Higgs mechanism, the W and Z bosons obtain their masses.

2.2.2 Components of the SM Lagrangian

The Lagrangian formalism allows separation of free (particle) terms or kinetic terms, and interaction terms. The SM Lagrangian can be split into four distinct groups, based on the particles and the interactions that they describe:

$$\mathcal{L}_{SM} = \mathcal{L}_{gauge} + \mathcal{L}_{fermion} + \mathcal{L}_{Yukawa} + \mathcal{L}_{Higgs} \tag{3}$$

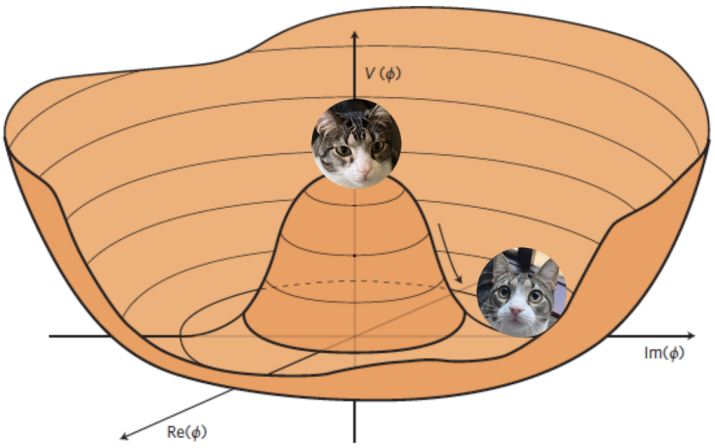


Figure 2.3: Illustration for the case of SSB in a $U(1)$ model. Choosing a point at the bottom of the potential spontaneously breaks the rotational $U(1)$ symmetry [31].

The first term, $\mathcal{L}_{gauge}$ describes the low energy gauge groups of the SM, and can be expanded to show the contributions of $SU(3)$ (colour), $SU(2)_L$ (weak isospin[3]) and $U(1)$ (hypercharge[4]):

$$\mathcal{L}_{gauge} = \mathcal{L}_{QCD} + \mathcal{L}_{I_W} + \mathcal{L}_Y \tag{4}$$

$$= -\frac{1}{4g_3^2}\sum_{A=1}^{8} G^A_{\mu\nu} G^{\mu\nu A} - \frac{1}{4g_2^2}\sum_{a=1}^{3} F^a_{\mu\nu} F^{\mu\nu a} - \frac{1}{4g_1^2} B_{\mu\nu} B^{\mu\nu} \tag{5}$$

$G^A_{\mu\nu}$ represents the color field strengths, and g_1, g_2, g_3 are the dimensionless colour, weak isospin and hypercharge coupling constants. $F^a_{\mu\nu}$ represents the weak isospin field strength, and the hypercharge field strength is represented by $B_{\mu\nu}$.

$\mathcal{L}_{fermion}$ describes the fermion fields and their gauge interactions:

$$\mathcal{L}_{fermion} = \sum_{i}^{3} \left(L_i^\dagger \sigma^\mu \mathcal{D}_\mu L^i + \bar{e}_i^\dagger \sigma^\mu \mathcal{D}_\mu \bar{e}^i + \mathbf{Q}_i^\dagger \sigma^\mu \mathcal{D}_\mu \mathbf{Q}^i + \bar{\mathbf{u}}_i^\dagger \sigma^\mu \mathcal{D}_\mu \bar{\mathbf{u}}^i + \bar{\mathbf{d}}_i^\dagger \sigma^\mu \mathcal{D}_\mu \bar{\mathbf{d}}^i \right) \tag{6}$$

In Equation 6, L_i represents the weak doublet of leptons, e_i the weak lepton singlet, $\mathbf{Q}_i$ the quark weak doublet and $\bar{\mathbf{u}}_i$ and $\bar{\mathbf{d}}_i$ the antiquark weak singlets. i ranges over the three families of chiral fermions, $\mathcal{D}$ are the covariant derivatives of the different fermion fields and σ^μ are the standard Pauli matrices [32].

The covariant derivative acting on left-handed fermion fields is given by:

$$D_\mu \equiv (\partial_\mu - igA^a_\mu t^a - ig' Y_{\psi_L} B_\mu) \tag{7}$$

[3]The weak isospin is the gauge symmetry attributed to the electrically charged part of the weak interaction, and connects quark and lepton doublets in all generations. If a particle has a weak isospin of a half-integer value, it can interact with the $W^\pm$ bosons. Isospin, or strong isospin, is the gauge symmetry attributed to the strong force in the group $SU(2)$, and relates the up- and down- content of hadrons.

[4]The hypercharge of a particle is the quantum number that is conserved under strong interactions. The operator accounts for three properties: isospin, electrical charge and flavour.

where $A^a_\mu(x)$ are the three $SU(2)_L$ gauge bosons, $B(x)$ is the $U(1)_Y$ hypercharge gauge boson and g and g' are the corresponding (dimensionless) gauge couplings.

The strong covariant derivatives are given by:

$$D_\mu \equiv \partial_\mu - ig_s G^a_\mu \tag{8}$$

with the eight new gluon field strength tensors $G^a_{\mu\nu}$, with $a = (1...8)$ and

$$G^a_{\mu\nu} \equiv \partial_\mu G_\nu - \partial_\nu G_\mu - ig_s[G_\mu, G_\nu] \tag{9}$$

where g_s is the coupling for the strong force.

The term responsible for describing the Yukawa coupling of the fermions to the Higgs field is given by:

$$\mathcal{L}_{Yukawa} = i\left(\hat{L}_i y^{[e]}_{ii} + \hat{\mathbf{Q}}_i y^{[d]}_{ii}\bar{\mathbf{d}}_i\right)H^* + i\hat{\mathbf{Q}}_i\mathcal{U}_{ji}y^{[u]}_{jj}\bar{\mathbf{u}}_j\tau_2 H + c.c. \tag{10}$$

H represents the Higgs field, and y_{ii} the hypercharge assignments, dependent on the Yukawa coupling constants. τ_2 are the weak isospin indices and $\mathcal{U}$ the Cabibbo-Kobayashi-Maskawa matrix. The notation follows $\hat{\eta} \equiv \eta^T\sigma_2$.

The final part of the Lagrangian is the $\mathcal{L}_{Higgs}$, describing the Higgs doublet, its interactions with itself and the gauge field. The Higgs Lagrangian is:

$$\mathcal{L}_{Higgs} = (\mathcal{D}_\mu H)^\dagger(\mathcal{D}^\mu H) - V(H) \tag{11}$$

The covariant derivative $\mathcal{D}$ is of the form:

$$\mathcal{D}_\mu = \partial_\mu + iW_\mu + \frac{i}{2}y_h B_\mu \tag{12}$$

where W_μ refer to the intermediate vector bosons in the weak isospin field, and $V(H)$ is the same form as equation 1, however the choice of $\mu^2 < 0$ has been written explicitly as $-\mu^2$:

$$V(H) = -\mu^2 H^\dagger H + \lambda(H^\dagger H)^2$$

2.3 Standard Model Interactions

The interactions between the SM fermions and the gauge bosons are described by interaction vertices. The properties of the interaction are determined by both the properties of the gauge bosons, and the nature of the interaction.

Figure 2.4 shows the different interaction vertices for the different forces in the SM. The strong interaction only involves quarks and gluons, and never changes flavour. The strong coupling constant α_s is approximated to 1 at low energies. The electromagnetic interaction is mediated by the photon and involves all electrically charged fermions, with a coupling constant $\alpha \simeq 1/137$. These interactions never change flavour. The weak interaction is split into the charged current interaction, and the neutral current interaction. Both of these interactions involve all fermions, and have a coupling strength of $\alpha_{W/Z} \simeq 1/40$. In the charged current interaction, which is mediated by the $W^\pm$ bosons, the fermions always change flavour, while in the neutral current interaction, which is mediated by the Z boson, the fermion flavour does not change.

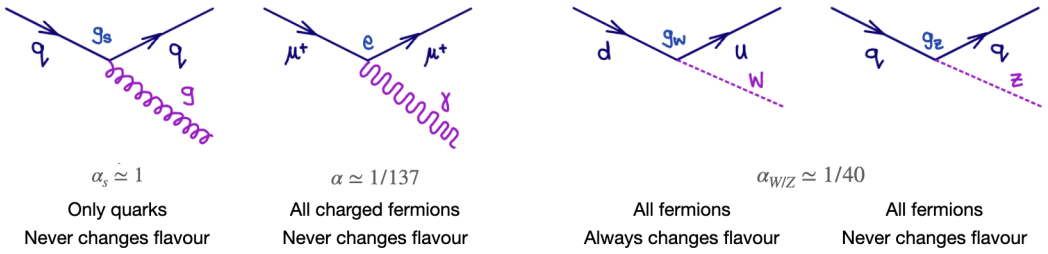


Figure 2.4: Diagrams showing the four different SM interaction processes. The first diagram shows the strong interaction vertex, and shows an example of the strong interactions between quarks and gluons. The second diagram shows the electromagnetic interaction, which takes place between all electrically charged fermions. The third and fourth diagrams show the weak current interaction which takes place between all fermions, first in the charged-current case (with W-bosons) and then in the neutral-current case (with Z-bosons).

2.3.1 Feynman Diagrams and Mandelstam Variables

Feynman diagrams are pictorial representations of interaction amplitudes, each part corresponding to a mathematical term [33]. They represent the term of the perturbation expansion of the scattering matrix and correspond to all possible transitions from two particles, a and b, to two particles, c and d, over all time-orderings and polarisations. The diagrams are constructs that correspond to the exchange of "virtual exchange particles", and the four-momentum is conserved at all interaction vertices.

The Mandelstam variables s, t and u are used to classify diagrams with a single force carrier, according to the four-momentum of the exchanged particle. The squared four-momentum is given by s, t or u, depending on the diagram. Each of these channels has a physical interpretation, and are shown in Figure 2.5. In the s-channel, particles 1 and 2 from an intermediate particle that splits up into particles 3 and 4. In the t-channel, particle 1 emits a virtual intermediate particle and becomes particle 3, while particle 2 absorbs the intermediate particle and becomes particle 4. The u-channel is analogous to the t-channel, and u-channel diagrams only exist for identical outgoing particles, since the same final state can occur with two different exchange momenta. s, t and u are kinematic variables and are defined in terms

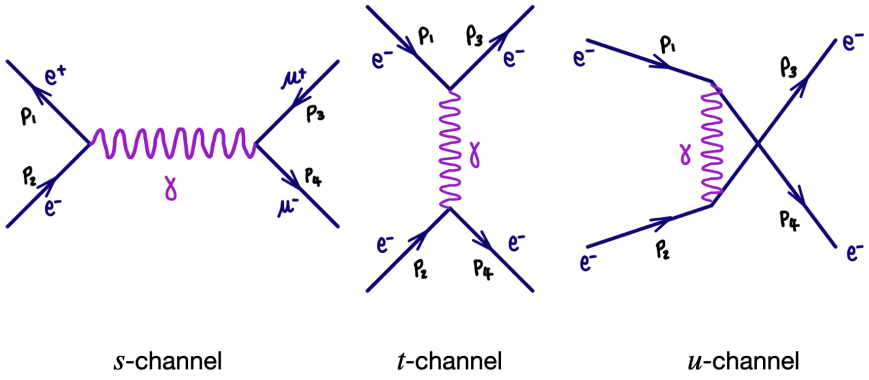


Figure 2.5: Feynman diagrams for the three different Mandelstam variables. The first diagram shows the s-channel, the second the t-channel and the third the u-channel.

of the momentum p of the particles in the interaction:

$$s = (p_1 + p_2)^2 = (p_3 + p_4)^2$$
$$t = (p_1 - p_3)^2 = (p_4 - p_2)^2$$
$$u = (p_1 - p_4)^2 = (p_3 - p_2)^2$$

2.3.2 Perturbation Theory and Cross Section Calculations

The coupling constant α_s of QCD is energy dependent: at low energies or long distances, α_s is approximately equal to 1. In this case, particles are confined and this is the non-perturbative regime of QCD. At higher energies or shorter distances, α_s is small and calculation are made in the perturbative regime of QCD.

If the strong coupling constant $\alpha_s \ll 1$, the interaction amplitude can be expanded in powers of α_s:

$$f = f_0 + \alpha_s f_1 + \alpha_s^2 f_2 + \alpha_s^3 f_3 + ... \tag{13}$$

The first term is called the leading order (LO) term, the second the next-to-leading order (NLO) term, the third next-to-next-to-leading order (NNLO) term and so on. Perturbative calculations are particularly useful when calculating the hard-scattering cross-sections of processes.

The differential cross-section of a process can be given as a perturbative expansion in the strong and electroweak couplings, at the electroweak scale (where $\alpha_s \sim 0.1$ and $\alpha \sim 0.01$):

$$\mathrm{d}\hat{\sigma} = \mathrm{d}\hat{\sigma}^{(0,0)} + \alpha_s \mathrm{d}\hat{\sigma}^{(1,0)} + \alpha_s^2 \mathrm{d}\hat{\sigma}^{(2,0)} + \alpha_s^3 \mathrm{d}\hat{\sigma}^{(3,0)} + \alpha \mathrm{d}\hat{\sigma}^{(0,1)} + \alpha\alpha_s \mathrm{d}\hat{\sigma}^{(1,1)} + ... \tag{14}$$

The first term in Equation 14 is the LO term, with no dependence on α or α_s. The next three terms, with indices $(i, 0)$, are the NLO, NNLO and N3LO terms for the QCD contribution to the cross-section. The fifth term is the NLO electroweak contribution, and the last term shown is the mixed QCD-electroweak contribution, and is dependent on both α and α_s. Including higher-order terms improve the precision of the cross-section calculation, but is mathematically complicated.

Visualisations of the higher order processes are shown in Figure 2.6. The first diagram depicts the LO process. In this case, there are no real or virtual gluons emitted after the initial interaction. There is no α_s dependence in the cross-section of this calculation, and the calculation is relatively easy. The next two diagrams depict NLO processes. The first, on the left, shows the emission of a real gluon, while the other diagram shows the exchange of a virtual gluon. The dependence on α_s is quadratic, and these calculations are computationally more expensive. They require the consideration of all diagrams that have this extra factor of α_s, the real radiation (the first figure) and the virtual emission (second figure). For the virtual diagrams, integration over the loop momentum is required. Virtual corrections in NLO cross-section calculations ($\mathcal{O}(\alpha_s)$) arise from the interference between the tree-level and one-loop virtual amplitudes. Event generators like MadGraph [34] (further discussed in section 2.4.1) are capable of calculating these cross-sections.

The second and third rows of Figure 2.6 show the NNLO processes and emissions of gluons. The first two show the double-virtual emission, the third the real-virtual emission of two gluons, and the fourth and fifth the double-real emission. Multi-leg diagrams represent real emission, while multi-loop diagrams show the inclusion of additional loops that are not real.

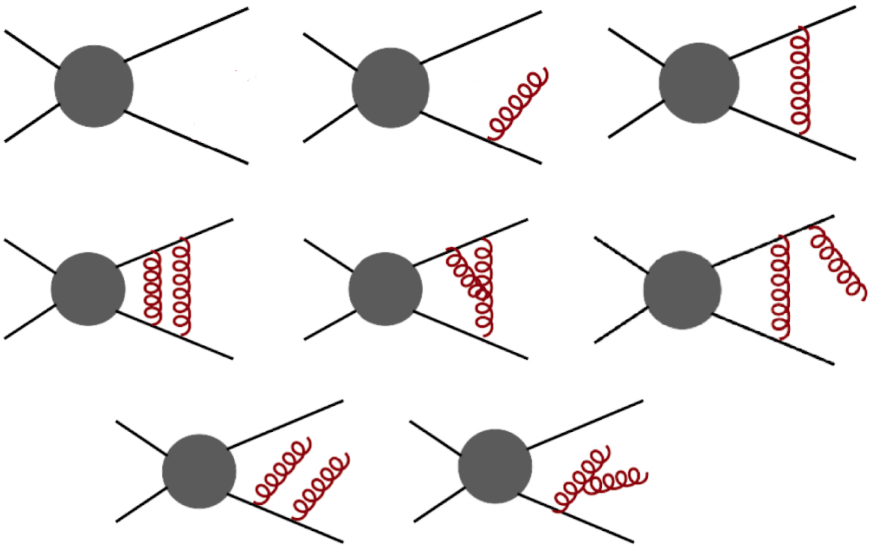


Figure 2.6: Representations of the higher-order correction terms that are added in a process. The first diagram represents LO, the next two NLO. The bottom five diagrams represent NNLO corrections that need to be considered.

LO, NLO and NNLO QCD calculations are essential for precision calculations and measurements. NLO QCD calculations add a factor of $\sim$ 10% to the accuracy of a cross-section measurement, and NNLO QCD calculations add a factor of $\sim$ 1%, as do NLO electroweak calculations.

2.4 Generating and Analysing Standard Model Processes

Being able to simulate high-energy physics processes is a necessity to extract the desired information from data taken at collider experiments. Monte Carlo (MC) event generators [35] are part of a large ecosystem of computational tools developed that can model SM processes, and are build on the foundation of the Monte Carlo technique for integral evaluation. Using the MC technique for integral evaluation in necessary due to the many degrees of freedom that are introduced with each particle and interaction. MC event generators simulate signal and background processes, and are an integral part of analyses carried out by experiments at the LHC. This section serves as a walk-through of the process, highlighting some of the event generators commonly used in the field, and the blocks they are built on. The components of a particle collision are shown in Figure 2.7, and the components and specific generators are discussed in the context of a specific software programme in following paragraphs.

2.4.1 Matrix-element Generator: MadGraph5

MadGraph5 [34, 37] is one of the standard matrix-element generators in the field. MadGraph5_aMC@NLO, the programme developed to include NLO calculations, automatically generates matrix elements at tree-level and at NLO, and from this it automatically computes cross-sections and generates events, simulating the physical processes. These generated events are then used to predict physical observables with different perturbative accuracies and final

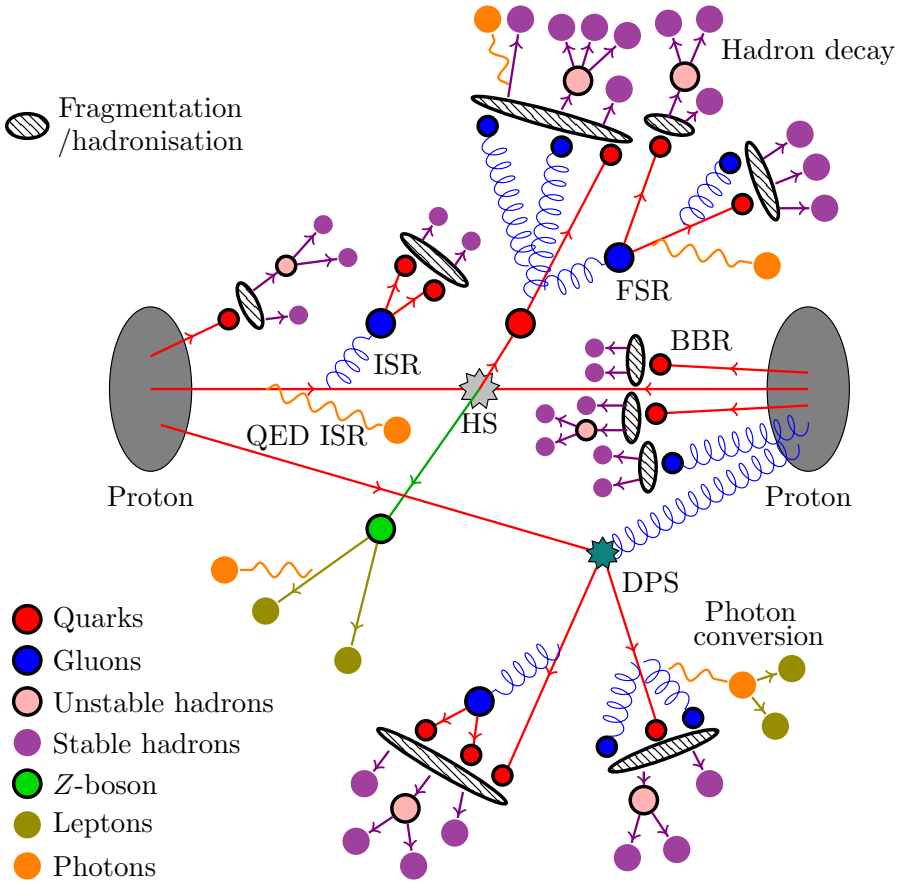


Figure 2.7: Diagram representing the different parts in a particle physics collision [36]. The hard collision is represented by HS label in the centre, and shows the production of a Z-boson and a quark. The Z-boson decays into two leptons, with a photon being radiated by one of the leptons. The quark produced in the hard scattering emits gluons (final state radiation of FSR), and the emitted gluons and quark undergo fragmentation and hadronisation. Hadron decay from unstable hadrons is also shown after the hadronisation step. The diagram also shows initial state radiation (ISR), QED ISR where a photon is emitted, douple parton scattering (DPS), photon conversion to two leptons, and beam beam remnants (BBR). Monte Carlo generators are able to simulate all components of these hadron collisions.

state descriptions for the model.

The cross-section calculation for the production of two particles XY in a proton-proton collision is of the form:

$$\sigma(pp \to XY) = \sum_{a,b} \int \mathrm{d}x_1 \mathrm{d}x_2 f_a(x_1, \mu_F) f_b(x_2, \mu_F) \times \hat{\sigma}(ab \to XY) \tag{15}$$

$f_a(x)$ is the probability to find parton a inside the proton with momentum fraction x, and μ_F is a scale which separates low energy from high energy dynamics. The functions f_a and f_b are parton distribution functions (PDFs) [38] and are fed into MadGraph via the LHAPDF [39] interface. The cross section $\hat{\sigma}(ab \to XY)$ is the theoretical cross-section of the production of XY, as calculated in Equation 14, and had LO and higher-order contributions from QCD and the EW interactions.

MadGraph outputs event information in the form of Les Houches Event (LHE) files [40],

which is a standardised output file format that matrix-element generators use. LHE files contain parton-level information about the hard process (the red circles and lines in Figure 2.7) generated.

2.4.2 Parton Showering and Hadronisation: Pythia8

Another important process called hadronisation [41] takes place in particle collisions. When an initial $q\bar{q}$ pair is produced in a particle collision, and the two quarks separate at high velocities, the field between the quarks increases to a point that the energy stored in the field is sufficient to provide the energy necessary to form a new $q\bar{q}$ pair. The colour field is broken into smaller "strings" that are energetically more favourable, and the process continues and forms more $q\bar{q}$ pairs until the colourless hadrons can be formed at lower energies. Experimentally, quarks and gluons are therefore seen as a spray of particles called jets. The process of jet formation from an experimental point of view is further discussed in Section 4.4.1.

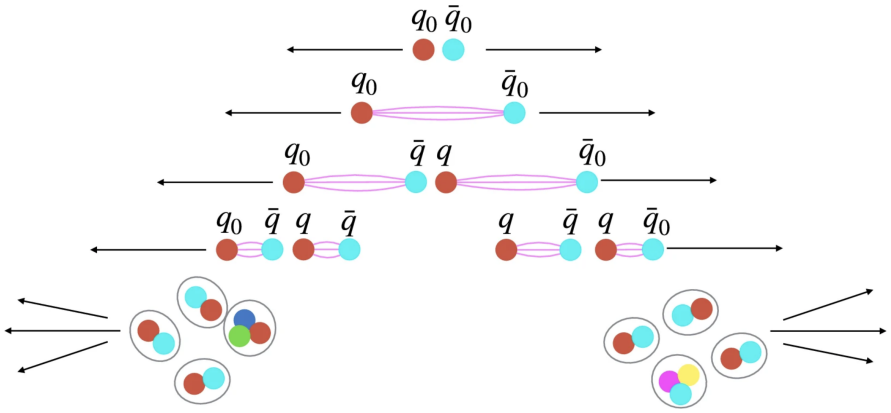


Figure 2.8: The hadronisation process, taken from [42].

The next step in the event-generation process is parton showering [43] and hadronisation. Pythia8 [44] is one of the event generators that takes parton-level information and showers them using a parton-showering algorithm[5]. Pythia8 performs the parton showering and hadronisation, and can also add underlying events to information obtained from LHE files. Following the hard process, there are two levels to event generation in Pythia8: the parton level and the hadron level.

Initial and final state radiation, and multi-parton[6] interactions [45], are included in the parton level. This level also treats possible beam remnants and colour-recombination. At the end of the parton-level evolution, the event represents a realistic partonic structure that includes jets and a description of underlying events. The parton level has different algorithms used to determine the parton evolution of SM processes.

QCD confinement is taken care of in the hadron level, and in Pythia8 this is done by describing hadronisation as the fragmentation of QCD strings into colourless hadrons. Hadronisation models are non-perturbative and require modelling and parameter-tuning, and in Pythia8 it is based on the Lund String Model [46, 47]. After the hadronisation process is complete, the

[5]Pythia8 can also produce matrix elements for a select number of simple processes, but the development of their parton-showering algorithm is what the programme is known for.

[6]Hadrons are composite in nature and in a single hadron-hadron collision, it is possible to have multiple parton hard-scatterings.

output is a event that would be possible to observe in a detector. The hadron-level event file contains richer information than the parton-level event file, due to the inclusion of the large collection of hadrons given together with their four-momentum.

The output format of data after running Pythia8 is a HepMC3 file [48]. The HepMC3 event record library holds information from simulated events on per-event and simulation-run bases, and eases the manipulation and analysis of the events.

2.4.3 Analysis Frameworks: RIVET, MadAnalysis5 and ROOT

RIVET, or the Robust Independent Validation of Experiment and Theory, is a toolkit designed to validate Monte Carlo (MC) event generators [49–51] and is widely used in analysis preservation at particle colliders. The toolkit facilitates comparisons between theoretical calculations of the final states in particle collisions, and measurements of those final states. RIVET has an extensive set of analyses, mostly measurements of particle properties made by the ATLAS and CMS collaborations, that enable comparison between MC generated events and data, through a connection to HepData [52]. HepData is an open-access online database that contains the data points from plots and tables stemming from thousands of publications, including those from the experiments at the LHC.

RIVET takes a HepMC data file as input and analyses each event. The programme reconstructs quantities that are present in a given experimental analysis for event selection and data processing. The datasets are output in a format that is comparable to public data from particle collider experiments.

MadAnalysis5 is a framework for phenomenological studies at particle colliders [53]. Taking a HepMC file containing hadron-level information, or a LHE file with parton-level information, the framework allows for sophisticated analyses to be carried out on the generated MC samples. MadAnalysis5 uses a fast detector-simulation tool called Delphes [54], which reconstructs detector level objects like photons, jets, leptons and missing energy[7] with their properties.

Both RIVET and MadAnalysis5 allow the creation of histograms of observables that illustrate the different properties of the generated physics processes, and only work with MC-level events.

ROOT [55] is an analysis framework that is used to analyse and visualise scientific data, and has its own specific data format. The framework has an advanced graphical user interface for visualisation of data, and a large library of mathematical functions that can be applied to fit various functions and perform statistical analyses. ROOT is the standard analysis framework used when working with experimental data.

[7] Event reconstruction in detectors is fully discussed in Section 4.4.1.

3 Extending the Standard Model

As well-formulated as it may be, the SM does not answer all the open questions in particle physics. It was put together from different theoretical ideas: QFTs, the Dirac Equation of relativistic quantum mechanics, the gauge principle and the Higgs mechanism, and tested extensively using particle colliders and experiments. Some of the missing pieces are highlighted below. This section also introduces an overview of Beyond the Standard Model (BSM) models. The discussion is non-exhaustive - the models are an extension of the SM and do not discuss all possible New Physics phenomena. The focus is on the Dark Sector (DS): a collection of new hypothetical particles and quantum fields, that broadly covers the vast variety of particles that can be considered as Dark Matter candidates.

3.1 Missing Pieces in the Standard Model

The existence of dark matter [56] and dark energy [57] are arguably the biggest open questions in all of physics. The hierarchy problem [58] is one concerned with naturalness and the energy scales seen in nature. Many other problems like neutrino masses and baryon asymmetry are all questions that are yet to be addressed as well, but are not discussed here.

3.1.1 The Hierarchy Problem

The hierarchy problem is a problem of naturalness. Two of the fundamental scales in nature are the Planck scale ($M_{Pl} = G_N^{-1/2} \sim 10^{18}$ GeV) and the electroweak scale ($m_{EW} \sim 10^3$ GeV), with the ratio of the gravitational (Newtonian) and weak (Fermi) interaction constants around 10^{-34}. The fundamental nature of the weak scale can be stated with experimental certainty [59], but the big question is: why there is such a large difference in these scales? There is a large discrepancy between aspects of the weak force and of gravity, most notably that the weak force is 10^{24} times stronger than gravity. The Hierarchy Problem also asks why the Higgs boson mass is so much lighter than the Planck mass, through the renormalisation of the Higgs mass and the cancellation of terms to achieve the Higgs mass at the electroweak scale. Electroweak symmetry breaking (EWSB) is triggered by the Higgs VEV, and the difference in mass scales is evident in the following:

$$\mu^2 = \lambda v^2 \sim 10^4 \ \mathrm{GeV}^2 \ll M_P^2 \sim 10^{38} \ \mathrm{GeV}^2 \tag{1}$$

The naive expectation would have been to have $\mu^2 \sim$(heavier scale)$^2 \sim M_P^2$, but this is not the case. The hierarchy seems to exist because of some fine-tuning, which goes against the desire for naturalness in the models created. However, the hierarchy problem directly motivates new physics searches in collider experiments. Many models that extend on the SM

(some of which are discussed in Chapter 3) aim to explain this smallness of the hierarchy, and many Dark Matter searches are put in the context of solutions to the hierarchy problem. This also leaves space for Effective Field Theories (EFTs), a local QFT at low energies with the degrees that survive at this scale, and other new models to explain symmetry breaking and the patterns of fermion masses and their mixing. Composite Higgs models, where the Higgs boson is not a fundamental particle but rather a bound state of some strong interaction, have been extensively formulated to try and resolve the hierarchy problem [60, 61].

3.1.2 Dark Energy and Dark Matter

The existence of Dark Energy and Dark Matter are driven by observational evidence in astronomy. These two constituents are called dark because they do not interact via the three forces described in the SM, and are only detectable via their interaction with gravity. The Universe consists of three constituents: baryonic matter, Dark Matter and Dark Energy [62]. Baryonic matter makes up around 5% of the Universe and is the only constituent we can actually see. Dark Matter is inferred from its gravitational effects on baryonic matter and makes up 26% of the Universe. Dark Energy, the driving force of the acceleration of the expansion of the Universe, makes up the remaining 69%.

The observational evidence for the existence of Dark Energy first came from observing supernovae in the late 1990s [63, 64]. The distant Type 1a supernovae observed have a constant luminosity, and so they can be used as standard candles to make accurate distance measurements. The cosmic acceleration, or the accelerating expansion of the Universe, is inferred to be driven by the existence of this hypothetical form of energy that exerts a negative pressure and causes the universe to expand at an ever-increasing rate. Other evidence for Dark Energy comes from the cosmic microwave background radiation [65], X-ray observations of the gas content and growth of clusters of galaxies [66] and gravitational lensing, the distortion and bending of light due to massive celestial bodies [67] as seen in Figure 3.1. Dark Energy and its role in the evolution of the Universe is still not entirely understood. Recently, the Dark Energy Spectroscopic Instrument (DESI) found that the current rate of expansion of the Universe is not constant as it was previously thought to be, but rather changing in unexpected ways [68–70].



Figure 3.1: The James Webb Space Telescope's First Deep Field (NIRCam Image) [71] shown on the left, and the Bullet Cluster shown on the right [72]. The matter distribution in the Bullet Cluster is calculated by gravitational lensing (shown in blue), and this is superimposed on the X-ray image (shown in pink) and the visible light image.

Observational evidence for the existence of Dark Matter has some overlap with evidence for

Dark Energy, but gravitational lensing (Figure 3.1), galactic rotation curves and the image of the Bullet Cluster (Figure 3.1) act as evidence on sub-galactic scales, and show the gravitational effect of Dark Matter on baryonic matter. The Bullet Cluster shows the collision between two galaxies clusters. The Chandra X-ray telescope detected hot gas (pink clumps) in the area that contains the most baryonic matter. This distribution is superimposed on the optical image from the Magellan and Hubble Space Telescope picture taken, with the blue areas in the picture indicating the areas that contain the most mass. The matter distribution is calculated using gravitational lensing, and superimposing the X-ray image over the galaxy mass distribution shows that most of the matter in the image is separate from the baryonic matter. This directly shows that nearly all of the matter in the cluster is dark or undetectable in nature [73].

3.2 The Dark Sector

Dark Matter (DM) is gravitationally interacting matter that does not interact via the forces described in the SM. Models, particles and interactions that try to explain and explore the existence of DM in the context of particle-level interactions are put under the umbrella-term "Dark Sector". The Dark Sector (DS) [74] provides theoretical frameworks in which searches for DM candidates can be performed. DS searches are often signature based, with direct signatures, indirect signatures and Long-Lived Particles (LLPs) being the three classes that the detection signatures can be split into.

- Signatures for DM candidates in colliders include processes in which a new mediator particle (or boson) decays into final states containing DM. These DM final states are invisible to the detector, since they interact weakly with the detector components and pass through the detector unobserved. These DM candidates are traditionally called Weakly Interacting Massive Particles (WIMPs), and the detector final state includes missing transverse energy or momentum, the magnitude of which is referred to as MET[1]. The new DM mediator needs to be produced with a visible (SM) particle, resulting in the term "mono-X searches" being applied to these final states, where X represents any SM particle (or decay product) visible in the detector.
- For indirect DM signatures in colliders, it is important to note that any mediator produced by the collision and the interaction of SM particles, can decay back to SM particles. Indirect signatures are the resonances that are found when a new mediator is produced, when the mediator decays back into fully visible SM states. These signatures are therefore sensitive to the SM interactions of the mediator.
- LLPs are a hypothetical class of particles that decay outside the range of the detector, and are therefore invisible to the detector, but could appear from interesting DS dynamics: these models could describe the elementary nature of DM by introducing additional unstable particles, more mediators and new interactions.

The theoretical frameworks on which DS models are built rely heavily on the observation of DM signatures in experiments. These DS models have DM particle candidates in the final states, or they propose BSM scenarios that could produces these DM particle candidates. DS

[1]A discussion of event and object reconstruction follows in Section 4.4, and specifically Section 4.4.4 for missing energy, but for the purpose of this discussion it is enough to know that invisible particles are observed as missing energy in detectors.

models require some DM particle, and a portal or additional sector through which SM particles can couple to DM particles. In the majority of DS models, this portal corresponds to a new mediator particle, however some models have modified couplings of the Z and Higgs bosons that allow the decay to DM states. The $W^{\pm}$ bosons are not included, since DM is neutral under the SM (electric) charge.

Figure 3.2 shows the broad classes of Dark Sector models that are being studied by the field [75]. DS models are split into two categories: simplified and extended sectors. Models in the simplified DS consist of DM and a single mediator particle, where DM normally takes the form of WIMPs. These models are incomplete, and act as proxies for more complete models but can nevertheless be used in searches at colliders. Models in the extended DS have more complex DS dynamics and the type of the DM particles under consideration may vary. The relevant branches to the work in this thesis are the spin-1 and fermion portals in the simplified DS, and the Hidden Valleys in the extended DS, although other branches will be briefly explained.

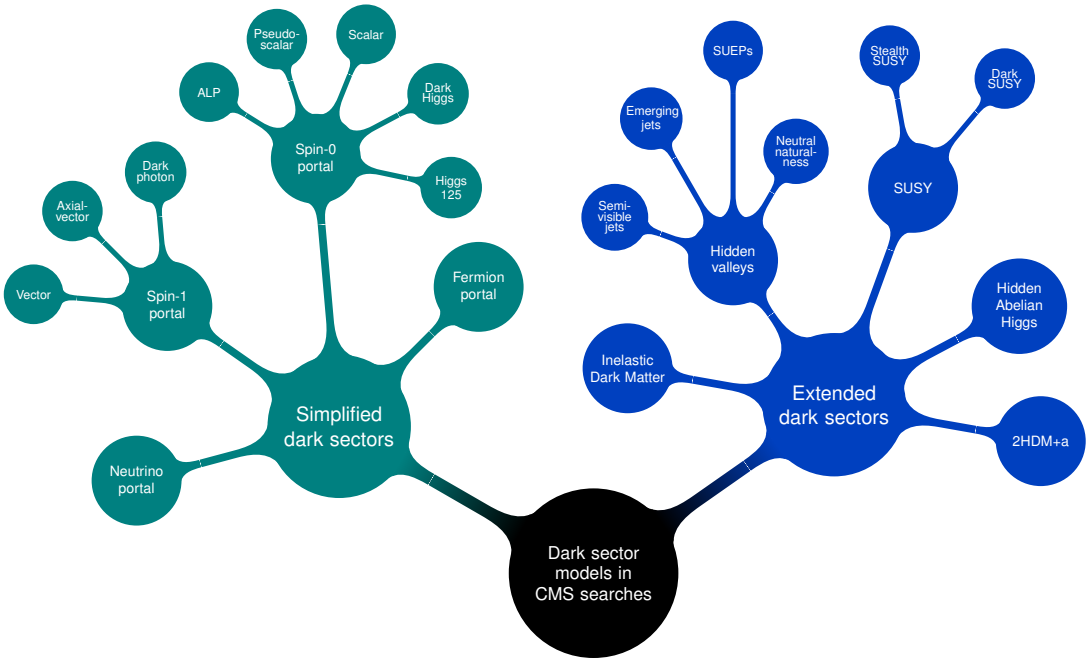


Figure 3.2: Representation of the different models in the DS, taken from [75].

3.2.1 Simplified Dark Sector

In the simplified DS [76], the visible sector is connected to the DS through a new mediator. This mediator enables the resonant and non-resonant production and physical production mechanisms for processes, and introduces other parameters in models that are relevant for collider searches.

The spin-1 portal class of models includes a mediator that couples to the SM, but the coupling is uniform across flavours and differs according to particle type [77]. As a baseline, models only have quark couplings but other couplings are possible. In more elaborate models, mixing between the new spin-1 mediator and SM Z-boson and photon is proposed to take place, giving rise to the Dark Photon models [77]. The Dark Photon (DP) is discussed further in Section 5.2, and a Feynman diagram representing the production of DM candidates via the DP is shown in Figure 3.3.

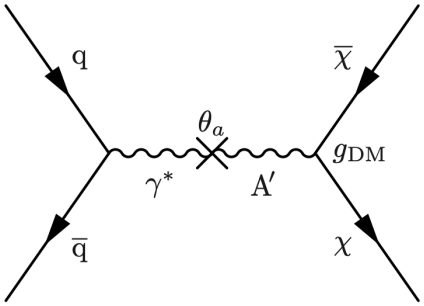


Figure 3.3: Feynman diagram showing the production of DM candidates via the DP mediator A', via mixing with the SM photon. θ_a is the mixing angle between the SM photon and the DP, χ represents the DM particle and g_{DM} is the coupling of the DP to DM. Taken from [75].

The fermion portal introduces Φ, an alternative scalar mediator, that couples the DM particles to the SM fermions, and introduces the non-resonant (t-channel) processes [78]. Lagrangians for the fermion portal are of the form:

$$\mathcal{L}_{\Phi} = \sum_{i,j} \lambda_{ij} \bar{\chi}_i \Phi_{ij} f_j \tag{2}$$

where i is the DM flavour index, j is the SM flavour index and λ_{ij} are the associated Yukawa couplings. Φ is a complex scalar particle and bifundamental, meaning that it is part of the fundamental representation for all gauge groups under which it is charged, one for each type of particle but also its own non-Abelian gauge charges. This is to ensure the conservation of the quantum numbers of the interacting SM and DM particles. The mediator Φ can be strongly charged, meaning that it can have quark couplings that are non-zero, and it can be produced in pairs via quark-antiquark annihilation or gluon-gluon fusion. It can also be produced via quark-gluon scattering, resulting in the production of Φ with a DM particle via, or through the virtual mediation of non-resonant DM production. Two of the four production modes are shown in Figure 3.4.

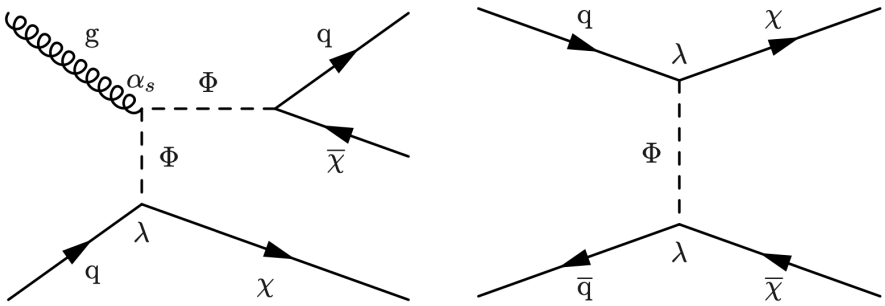


Figure 3.4: The Feynman diagram showing the single production of the mediator Φ with a DM particle χ is on the left, while the Feynman diagram on the right shows the non-resonant t-channel DM production. Taken from [75].

In the case of the spin-0 portal, the mediator is a pseudoscalar or scalar particle. In the most simplified models, the scalar mediator and the Higgs boson do not mix, but models can include a scalar portal that mixes with the Higgs boson, giving rise to a Higgs portal mediator H_D, or a "dark Higgs". The neutrino portal mainly discusses Heavy Neutral Leptons [79], massive leptons that are not charged under the SM gauge interactions and often take the form of right-handed neutrinos.

3.2.2 Extended Dark Sector

The Extended Dark Sector is characterised as having more complex DS dynamics. The possibility of communication with the SM through portals in the simplified sector is not excluded, although generally more than one DM particle species is included in these models. Including these additional DM states means that there are additional dynamics and kinematics, which could lead to interesting and novel experimental signatures. Four of the branches shown in the extended DS tree in Figure 3.2 warrant a short explanation, but the emphasis is placed on the Hidden Valley models.

Strongly Interacting Massive Particles

Strongly Interacting Massive Particles (SIMP) models [80] form part of the DS that include multiple new particles and new interactions, but can experience a dark force akin to the SM strong force. These interactions are assumed to be completely decoupled from the SM, and are at low energy scales, roughly around the energy scale of the lightest SM particles. This means that it is possible to access these interactions at particle colliders, specifically the LHC [81]. These models introduce rich dynamics and phenomenology, with DM candidates that are novel, stable and invisible to particle detectors.

SIMP models are characterised by the addition of a non-Abelian confining $SU(N_C^{dark})$ gauge interaction to the SM gauge interactions. N_C^{dark} refers to the number of dark colours in the gauge group, and this interaction introduces a gauge coupling α_{dark}. The force carriers in this new theory are massless dark gluons, akin to SM gluons but just in the DS. All SM particles are neutral under the new gauge group $SU(N_C^{dark})$, and the new light particles introduced are charged under it, and neutral under the SM gauge groups. The new light particles are dark quarks, denoted q_{dark} with mass $m_{q_{dark}}$, and there are N_F^{dark} flavours. Interactions between the SM fields and these dark quarks happen via higher-dimensional operators that carry both hidden-sector and SM charges.

An example of a simple SIMP scenario is given to illustrate how these interactions take place. If a broken $U'(1)$ gauge group is introduced, mediation between the DS and the SM can take place through a heavy vector portal. This leads to kinetic mixing between the $U(1)_Y$SM group and the $U'(1)$ DS group, and results in a DP that communicates with the SM via this kinetic mixing. Some models in this category are commonly called Dark-QCD models, due to its similarities with the SM QCD interactions. Dark-QCD is further discussed in Section 7.1, particularly focusing on semi-visible jets.

Soft Unclustered Energy Patterns (SUEPs) [82] are a class of SIMP model in which the jets formed are dissimilar to SM QCD jets[2]: instead of collimated jets, there is a large number of low-momentum charged particles that are spherically distributed. A schematic Feynman diagram showing the signal model can be seen in Figure 3.6. Neutral naturalness introduces new symmetries as a way to potentially fix the Hierarchy Problem. The new particles are not charged under the SM and arise in these models naturally, which typically set $N_C^{dark} = 3$. A dark Higgs boson and a uncoloured top quark partner are often introduced. The uncoloured top partner is referred to as a dark top quark.

[2]Further discussed in 4.4.1.

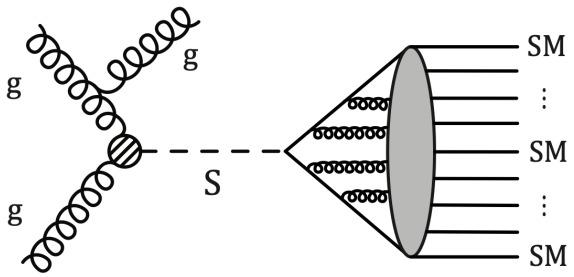


Figure 3.5: A Feynman diagram showing the signal model that results in a SUEP final state, taken from [82].

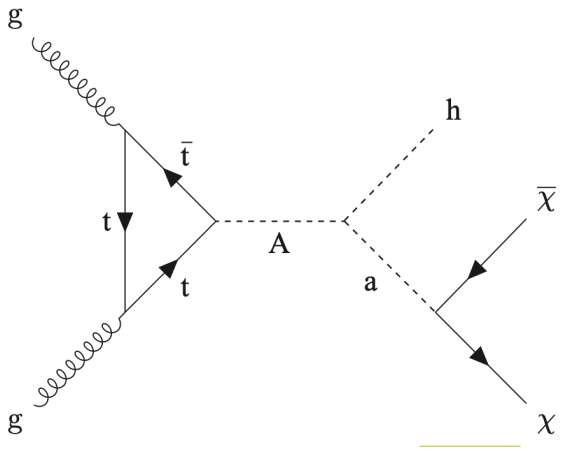


Figure 3.6: A Feynman diagram for a 2HDM+a model, taken from [85].

Other Extended Dark Sector Models

The 2HDM+a models [83] are an extension of the two-Higgs-Doublet Models (2HDM) [84], where an additional DM particle candidate and a spin-0 pseudoscalar mediator is added to the model. The Hidden Abelian Higgs Model (HAHM) adds an extra gauge group $U(1)_\chi$ to the SM, resulting in the gauge group $G = SU(3)_C \times SU(2)_L \times U(1)_Y \times U(1)_\chi$. This results in a new dark Higgs boson H_D and a neutral gauge boson, that are able to mix with SM fields. In many cases, this neutral gauge boson is chosen to be the Dark Photon.

Supersymmetry (SUSY) models can introduce light supersymmetric particles that are possible candidates for DM [86]. Dark SUSY models evolve from the extension of the SM through low-energy SUSY, in which DM is naturally embedded. Stealth SUSY models are more complex, and allow the introduction of a "stealth sector" in addition to the usual SUSY candidates. The stealth sector contains a scalar singlet S and the singlino $\tilde{S}$, its fermionic superpartner [87]. These models were developed after the LHC placed stringent limits on SUSY searches, and investigate ways that the SUSY partners have managed to go undetected. Inelastic DM models predict two DS states, scalars or fermions, with near mass degeneracy. Suppression of the elastic couplings between states with the same flavour takes place if the mass splitting is small relative to the average mass, in comparison to the inelastic couplings. As a result, in proton-proton collisions at the LHC there is simultaneous production of both states, mediated by a portal interaction that is most commonly taken to be the DP portal [88].

3.3 Generating BSM events and Exploring New Models

To perfrom any study on a BSM theory, simulated events of the theory need to be produced and in many cases, a comparison of signal and background (SM) processes needs to take place. The event generation is similar to that described in Section 2.4, but has a few additional tools and packages that facilitate the event generation and are used in specific BSM scenarios. An important part of BSM studies is comparison to existing results, which introduces the concept of reinterpretation and recasting, and tools that are used to perform these studies.

3.3.1 FeynRules

Starting with the Lagrangian of the BSM theory, the first step of the event generation process is to feed the Lagrangian into FeynRules [89], a Mathematica-based package that takes as input the Lagrangian, parameters and a list of fields in the theory and outputs the Feynman rules in a form that is usable by event generators. The output is given in a Universal FeynRules Output (UFO) format, a Python module that can be linked to Feynman diagram calculators. A full discussion of the UFO contents and its interface is in Reference [90], although it is useful to highlight the fact that the UFO output format is modular and flexible, and contains information of the model in an easily-accessible format for matrix-element generators.

The UFO file is then included when running the matrix-element generator, which is outputs an LHE file with the simulated events.

3.3.2 Pythia8 Hidden Valley

As introduced in Section 3.2.2, a specific DS class of particles include multiple new interactions and particles, leading to the development of a specific branch called Hidden Valley models, and specifically Dark-QCD. Pythia8 includes the Hidden Valley (HV) module, described in References [91, 92] that can be used to simulate these Dark-QCD processes.

The HV module was developed to allow the study of hidden sector hadronisation through the decay back to visible SM particles, and is specifically geared towards studying Dark-QCD like signatures. The implementation of the module in Pythia8 allows for flexibility in the model parameters: flavour contents, particle masses, gauge groups and gauge couplings can be set according to the model requirements, without losing the ability to produce hadron-level event files for analysis.

Figure 3.7 shows the production and decay of a dark sector particle D_v that forms part of a Dark-QCD model and is used to illustrate the possible processes that the HV module can work with. The dark quarks D_vs are pair produced via $q\bar{q}$ fusion, and emit massless dark gluons g_v as well as SM gluons g during the shower evolution. The D_v finally decays into a SM d-quark and a quark-like particle q_v that is part of the hidden sector. The decays in the model are flavour diagonal, with $D_v \to d + q_v$. The SM quark d can only emit SM gluons, while the hidden sector quark q_v can only emit hidden sector gluons g_v. The free parameters that need to be set are the masses of the communicator particle m_{D_v}, the mass of the dark quark m_{q_v}, and the coupling constant between the hidden sector and the SM, α_v.

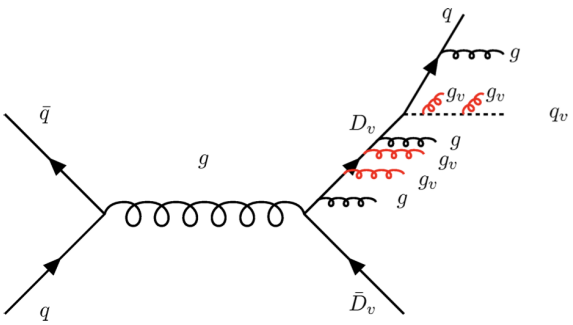


Figure 3.7: Example of a Dark-QCD process that is capable of being showered using the Pythia8 HV module, taken from [91].

3.3.3 Reinterpretation Using CONTUR and MadAnalysis5

Various analysis frameworks exist to analyse and interpret simulated events, from both SM and BSM processes. MadAnalysis5 was introduced in Section 2.4.3 in the context of performing analyses on SM processes, but it can also be used as a tool to search for new physics signatures, along with CONTUR (Constraints on New Theories Using RIVET) [93, 94].

CONTUR and MadAnalysis5 are used in reinterpretation studies, where data from particle colliders (particularly, but not limited to the LHC) is used to determine the validity of a BSM theory. Using analyses that have been carried out by experiments and preserved,[3] and subsequently validated by developers of the frameworks, regions of a parameter space can be excluded for a given model based on the data from the analyses.

An overview of the entire event generation process to setting limits for points in a parameter space for a BSM model is shown in Figure 3.8, followed by a short description of the CONTUR and MadAnalysis5 methodologies.

CONTUR

The CONTUR framework and approach to reinterpretation is built on measurements made at the LHC. Used as a layer on top of RIVET, CONTUR does a statistical interpretation of the injected BSM signal to SM phase spaces. This is possible because measurements of particle properties are not dependent on the SM, but match predictions from the SM well, and so data can be assumed to be an accurate representation of the SM. These measurements can be used to rule out different models, and influence the parameter space that searches for new physics are carried out in. RIVET has a large database of measurements carried out by the experiments at the LHC, and using this CONTUR can derive sensitivity from a broad range of SM measurements, with many different final states and variables.

CONTUR aims for speed and coverage of new models, at the cost of sensitivity and some precision. The toolkit focuses on fiducial, particle-level[4] measurements, to find the balance between the model dependence (so minimal theory extrapolation in the measurement) and

[3] Analysis preservation saves the methodology of the analysis, so that the same analysis can be carried out on MC samples or different datasets. The analyses are preserved either in RIVET for CONTUR, or the Physics Analysis Database (PAD) for MadAnalysis5.

[4] Particle-level data means data that has been unfolded, or corrected for detector effects, but not extrapolated beyond detector acceptance. To compare predictions to particle-level data, MC generated samples are needed for fiducial phase space selections to be applied to final-state particles.

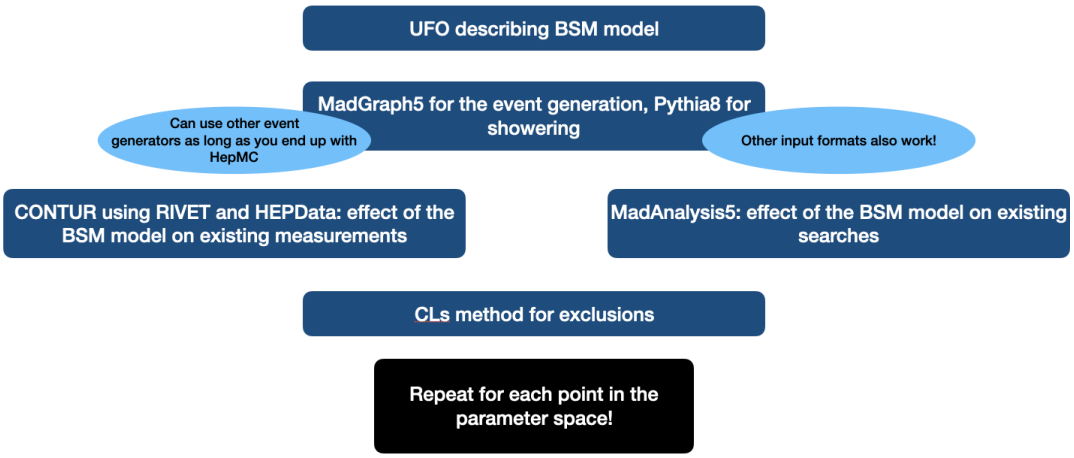


Figure 3.8: The CONTUR and MadAnalysis5 workflow. Starting with a UFO file that describes the BSM model, parton-level events are generated using MadGraph5, followed by the showering and hadronisation using Pythia8. The flexibility of the event generators and analysis frameworks means that other generators can be used, as long as they are in a recognised and compatible format. The standard is the HepMC file-format after the showering and hadronisation has been performed. Both frameworks use the CLs method for exclusions, and the process needs to be repeated for each point in the parameter space.

detector independence (minimal detector dependence in the BSM predictions). The toolkit divides analyses into orthogonal regions as to not create correlations between measurements, which would overestimate the sensitivity of the model probed. The histograms produced by RIVET are divided into orthogonal pools, according to the centre-of-mass energy of the LHC beam, the experiment performing the measurement and the final state of the analysis.

CONTUR calculates the CLs method [95, 96] to set exclusions (or upper limits) on the BSM model parameters, using a likelihood function for a certain parameter point. A full discussion of the statistical method can be found in Reference [94], although it is worthwhile to point out that through the definition of the CLs in CONTUR, a score close to one implies exclusion. The CLs calculation is carried out for each parameter point, and produces a heatmap showing exclusion of each parameter point, and the 95%, 68% and expected exclusion lines for the phase space.

MadAnalysis5

MadAnalysis5, as introduced in Section 2.4.3 is a useful toolkit to perform analyses on generated events, but can also be used in the context of reinterpretation. Testing new models relies on detector simulations and MadAnalysis5 uses Delphes or a simplified fast detector simulation package called SFS [97] for these detector simulations. While CONTUR mainly uses measurements made at the LHC, MadAnalysis5 uses data from searches performed at the LHC to determine the limits placed on a new model. A discussion of the methodology and implementation of exclusion calculations in MadAnalysis5 can be found in Reference [98].

4 The LHC and ATLAS

4.1 The Large Hadron Collider

The European Council for Nuclear Research (CERN) houses the most intricate accelerator complex in the world (Figure 4.1). A feat of engineering and innovation, the complex uses different systems and accelerators to accelerate particles to a final energy of 6.8 TeV. The proton beam is injected into Linear Accelerator 4, where negative Hydrogen atoms are accelerated to 160 MeV. The ions are then injected into the Proton Synchrotron Booster (PSB), and during the injection the ions are stripped of their two electrons. The remaining protons are accelerated to 2 GeV in the PSB and subsequently injected into the Proton Synchrotron, where they are accelerated to 26 GeV. The protons are then injected into the Super Proton Synchrotron, reaching energies of 450 GeV, before being injected to the Large Hadron Collider (LHC).

The LHC accelerates particles to 99.9999991% the speed of light, corresponding to a beam energy of 6.8 TeV. During previous runs, which are predetermined time periods in which data-taking takes place, the centre-of-mass energy progressively increased from 900 GeV, to 7 TeV, 8 TeV (Run 1) and 13 TeV (Run 2). This 27 km long synchrotron collider has two beams: one running clockwise, the other anti-clockwise, and the beams are brought together at four collision points, inside particle detectors with a centre-of-mass energy of 13.6 TeV. ATLAS, CMS, LHCb and ALICE are the particle detectors that probe these particle collisions, and are designed for observing different physics in the detectors.

4.1.1 Coordinates at the LHC

The coordinate system used by the ATLAS detector comprises of the variables x, y, z, θ, ϕ and η, with the interaction point taken as the origin. The x-coordinate points to the centre of the circular accelerator, the y-coordinate represents the vertical distance from the beamline, and the z coordinate goes along the beamline. The polar angle θ is defined as the angle from the z-axis, the pseudorapidity η measures the angle from the beamline in the y–z plane, and the azimuthal angle ϕ measures the angle around the beamline, in the x–y plane. The polar angle θ is commonly represented in terms of the pseudorapidity, with $\eta = -\ln\tan(\theta/2)$. The x-y plane is perpendicular to the beamline and is referred to as the transverse plane, and is commonly described in r-ϕ coordinates, where r (the radial dimension) is the distance from the beamline. The distance ΔR is defined as the following, and is shown in Figure 4.2:

$$\Delta R = \sqrt{\Delta\eta^2 + \Delta\phi^2} \tag{1}$$

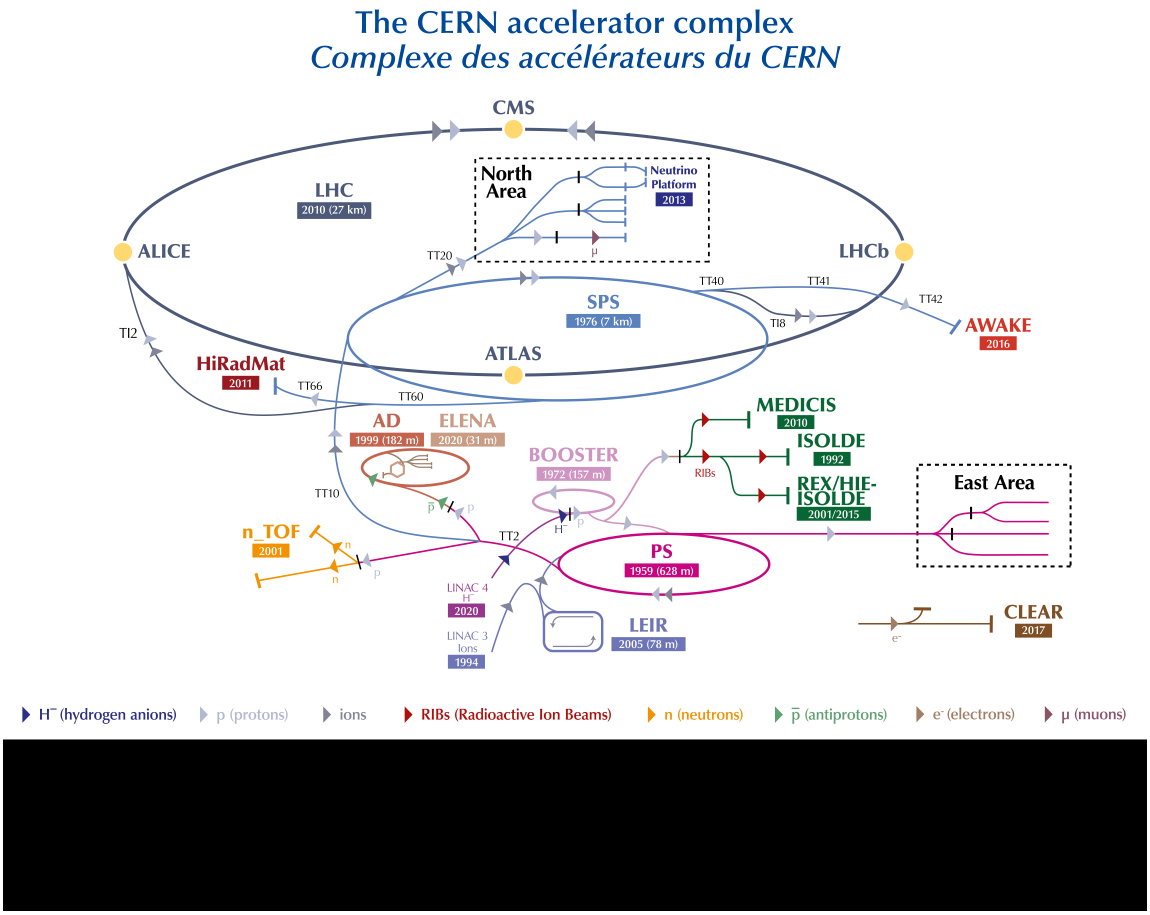


Figure 4.1: The CERN Collider Complex [99].

4.2 The ATLAS Detector

One of the four detectors at the LHC, the ATLAS detector [101] is the largest volume detector ever built at a particle collider and was initially designed for proton-proton collisions at centre-of-mass energy $s = \sqrt{14}$ TeV. The cylindrical detector weighs 7000 tonnes, is 44 meters in length, and has a diameter of 25 meters. It is located in a cavern 100 meters below ground.

This general purpose detector was designed and built to cover and measure the widest range of possible signals instead of focusing on a specific physical process. It consists of different detector subsystems that are layered concentrically around the beamline. These subsystems can be understood by placing them in four categories: the Inner Detector (ID), the calorimeter system, the muon spectrometer and the magnet system, as seen in Figure 4.3.

4.2.1 Inner Detector

The ID is the detector subsystem that is closest to the beamline, and consists of the Pixel Detector, Semiconductor Tracker, and Transition Radiation Tracker. The ID measures the direction, momentum, and charge of electrically-charged particles and relays this information to the Trigger and Data Acquisition (TDAQ) system.

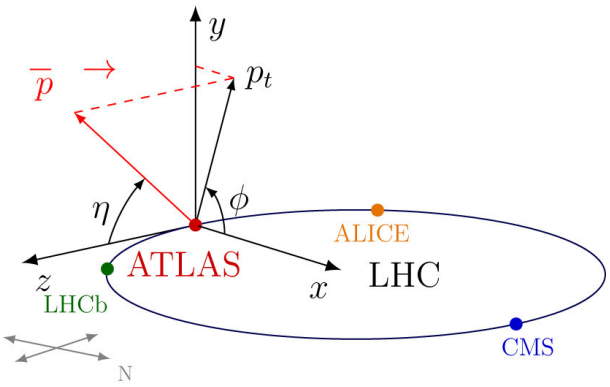


Figure 4.2: Coordinate system used at the LHC, with the detectors indicated along the beamline [100].

4.2.2 Calorimeter System

The calorimeters measure the energy of the particles passing through the detector, and are broadly split up into two classes: the electromagnetic calorimeter (which measures the energy of photons and electrons as they interact with matter and produce electromatic showers) and the hadronic calorimeter (which measures the energy of hadrons as they interact with atomic nuclei and produce hadronic showers). The Liquid Argon (LAr) Calorimeter is placed directly around the ID, and as end-cap calorimeters, and measures the energy of electrons, photons and hadrons. The Tile Calorimeter is placed concentrically around the LAr Calorimeter, and measures the energy of hadrons that were not stopped by the LAr Calorimeter.

4.2.3 Muon Spectrometer

The muon spectrometers (or muon chambers) are the final detector subsystem. Muons are registered in the inner detector and leave a small amount of energy in the calorimeter, but they do not produce showers in the calorimeters as opposed to electrons, photons or hadrons. They pass through several meters of material with minimal energy deposits, and so a dedicated spectrometer is required to measure the momenta of muons. The system uses 5 different detector technologies: Thin Gap Chambers (TGCs), Resistive Plate Chambers (RPCs), Monitored Drift Tubes (MDTs), Small-Strip Thin-Gap Chambers (sTGCs) and Micromegas. The MDTs are responsible for the precision of measuring the muon tracks through the spectrometer, and the TGCs and RPCs are used for the fast detection required by the experiment through the ionisation of gas in the chambers. The Micromegas and the sTGCs are specially designed to use in high-intensity collisions, and are used to detect muons close to the beamline with high precision and in a short timeframe.

The detector technologies used for fast-response detection pass on coarse information about the muon momenta that is then used by the trigger system in event selection.

4.2.4 Magnet Systems

ATLAS uses magnets to bend the trajectories of charged particles to measure their momentum and charge. The superconducting magnets are cooled to around 4.5 K and are split up into solenoidal and toroidal systems.

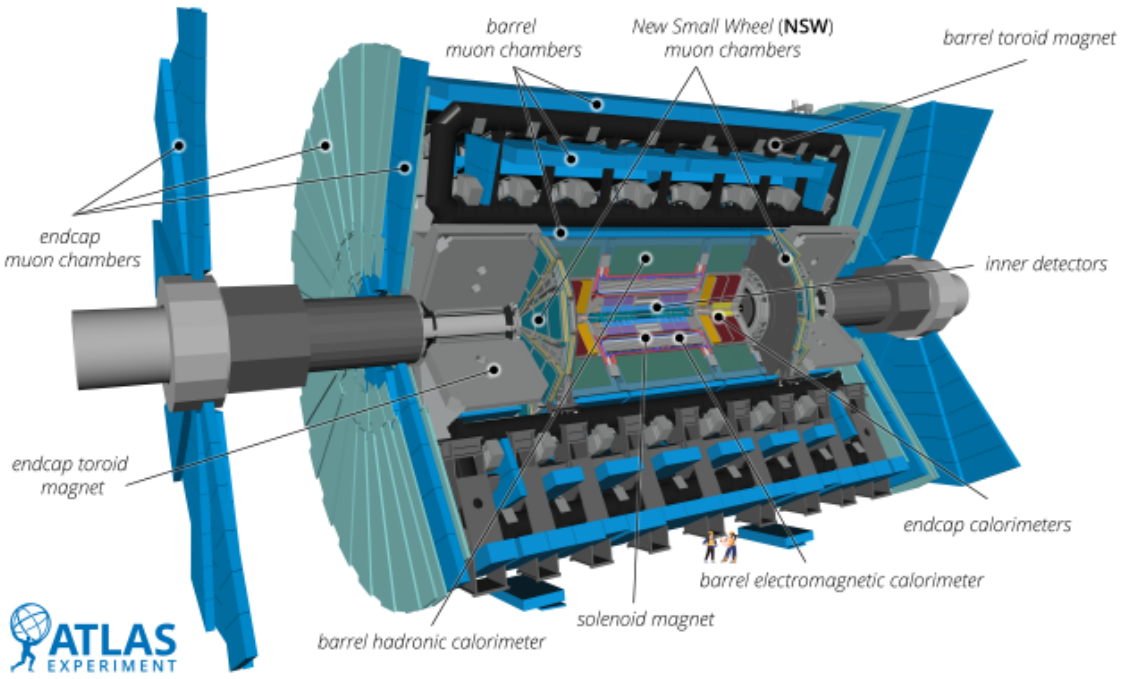


Figure 4.3: Schematic diagram of the ATLAS detector [102].

The central solenoid magnet surrounds the ID and provides a 2 T magnetic field that bends charged particles to measure their momentum. The ATLAS toroidal system consists of the barrel toroid and the end-cap toroids, and is used to measure the momentum of muons. The barrel toroid consists of 8 separate coils that are each 25.3 m in length and provide a 4 T magnetic field. The end-cap toroids each have 8 coils in a common cryostat, and extend the magnetic field to particles that leave the detector close to the beam pipe.

4.3 The ATLAS Trigger System

Data-taking at any of the detectors at CERN is an enormous undertaking, and relies on complex and state-of-the-art (TDAQ) systems to select, save and process data. This is no different at the ATLAS experiment, where the data from the 40 MHz collision rate of the Large Hadron Collider (LHC) needs to be decreased to the manageable data output rate of 3 kHz (or 8 GB/s). A diagram of the ATLAS trigger system is shown in Figure 4.4. This relies on innovative engineering, computing and physics to ensure that data is selected and saved for analyses to be carried out on.

The trigger system is a critical component of the ATLAS experiment and the data-taking process [103]. There are two levels to the system: Level-1 (L1) and the High-Level-Trigger (HLT), which work together to select which events are saved to be processed.

4.3.1 Level-1 Trigger

Data from the detector needs to go through two important components in the L1 trigger system as a first step in data acquisition: the Level-1 Calo (L1Calo) and the Level-1 Muon (L1Muon). L1Calo receives inputs from the calorimeter detectors: the Liquid Argon Calorime-

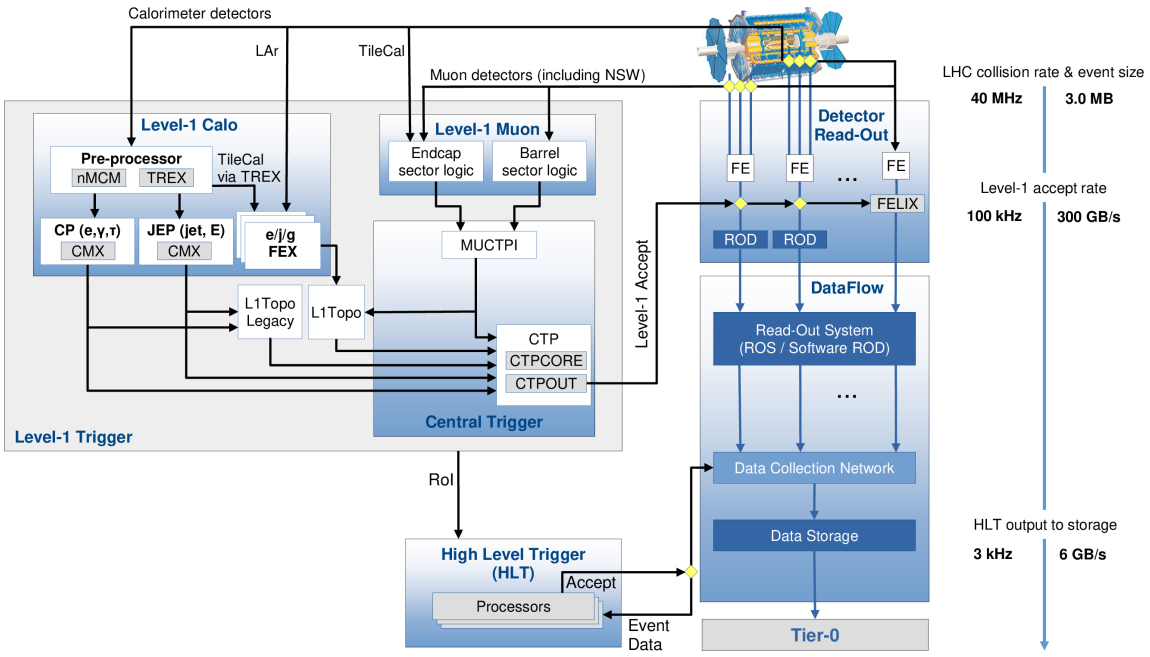


Figure 4.4: Overview of the ATLAS trigger system [104].

ter and the Tile Calorimeter. L1Muon receives inputs from the muon spectrometer. L1Topo is the next step in the L1 system and allows for more complex algorithms at L1 based on topological selections. It applies real-time kinematic and angular selections to trigger objects. Information from L1Topo is sent to the Central Trigger Processor (CTP). The CTP receives inputs from all of the L1 trigger systems, and produces 512 L1 trigger items based on logical combinations of these inputs. The CTP produces L1-accepts, which trigger the precision readout of a given event. The system combines this information in a format that is readable to the HLT, by identifying *Regions of Interest (RoIs)* with coarse information on the geometrical region in the muon spectrometer and the calorimeters, the type of object (corresponding to EM, τ, jet or muon) and the momentum or energy threshold passed.

4.3.2 High-Level-Trigger

The HLT reconstruction typically uses dedicated fast trigger algorithms to provide early background rejection, which is then followed by more precise and resource (CPU) intensive algorithms to make the final selection. The algorithms reconstruct objects, after which physics selections are applied. Athena, the ATLAS software framework [105], is used in the HLT reconstruction process.

HLT Chains

The HLT chain name contains all of the information of the chain configuration, in the format of `HLT_<HLT configuration>_L1<L1 seed threshold>`, and are categorised by their use cases. The primary chains are used for physics signals and in general all events passing these chains are recorded. The back-up chains are used in case of an unexpected luminosity increase and have higher thresholds compared to the primary chains. Supporting chains are chains that are used to support a physics analysis, (using data-driven background methods, efficiency measurements, etc.). Finally, monitoring chains are used to monitor the detector and to ensure good data quality, usually in the form of detector monitoring and calibration.

HLT Streams

The HLT chains are grouped together into streams, more formally defined as a collection of events or event fragments in the same dataset depending on the HLT decision. The design of the streaming model is inclusive (barring the debug streams), which means that an event can be written to multiple streams, although streams are designed to have minimal overlap. Physics streams include full event building with information from all sub-detectors, with an event size of $\sim$2 MB and an output rate of $\sim$3 kHz. The Main stream is used for most physics analyses. Delayed streams contain events that are not automatically reconstructed at Tier-0[1] to rather use the resources during downtime. The Enhanced Bias stream is used to record events for trigger rate predictions and is biased towards high-p_T events likely to be selected by the trigger.

4.3.3 The ATLAS Trigger Menu

The ATLAS collaboration has a dedicated physics programme which dictates what physics is being searched for, and the trigger system is responsible for selecting events aligned with the programme. This is all put together in the trigger menu, a collection of trigger chains and the corresponding set of rules that defines the rate that each chain can write out. Events are only selected to be recorded if they satisfy the conditions of one or more chains on the menu. The rules that define the output rate of each chain come in the form of a prescale value (or simply a prescale) that controls the rate of accepted events to stay within rate, bandwidth and CPU constraints. These prescales are computed using the trigger Rulebook.

The menu is constantly being updated and fine-tuned according to the running conditions and new developments. There are physics priorities aimed at taking a balanced dataset for analyses. Supporting triggers for calibration and efficiency measurements also need to be included. Online and offline resources available also contribute to the design of the menu and it varies with luminosity and time. Additionally, there are different menus defined for specific purposes and conditions: the proton-proton and heavy-ion physics menus differ considerably, and there are Cosmic and Standby menus for technical stops and machine development.

4.4 Event and Object Reconstruction in ATLAS

For any physics analysis to be carried out, physics objects need to be reconstructed. Events passing the L1 and HLT chains enabled during a run are sent to processing, where different objects are reconstructed and prepared for analysis.

4.4.1 Jets

The jet clustering algorithms that are used in modern collider experiments are called *sequential recombination algorithms* that combine the inputs in momentum-space to form the jets [36], in a bottom-up approach. There are two important values, d_{ij} and d_{iB} used in the reconstruction

[1] Tier-0 is the first part of the multi-tier processing centre based at CERN, and is responsible for the prompt processing of raw data from the detector, before distribution to other processing centres [106].

algorithm. The distance measure d_{ij} used to form the jets is calculated by:

$$d_{ij} = Min\left(p_{T_i}^{2\rho}, p_{T_j}^{2\rho}\right)\frac{\Delta R_{ij}^2}{R_0^2} \tag{2}$$

with $R_{ij} = (y_i - y_j)^2 + (\phi_i - \phi_j)^2$ equal to the distance between the two input objects. R_0 is a dimensionless angular radius parameter that can be varied, depending on the size of the jet that needs to be reconstructed.

The distance measure d_{iB} is the momentum-space distance between the detected particle and the beam axis, and is given by:

$$d_{iB} = p_{T_i}^{2\rho} \tag{3}$$

The sequential recombination algorithms look at the entire set $\{d_{ij}, d_{iB}\}$ and finds the minimum of the set. In the case that d_{ij} is the minimum, i and j are taken out of the list of particles and they are used to form a new particle, $\{ij\}$. If d_{iB} is the minimum in the set, i is taken out of the list of particles and labelled a final jet [36].

The variable ρ in Equations [2] and [3] is used to control the ordering or merging, depending on the value used. There are three cases: the k_T algorithm, where $\rho = 1$ [107], the anti-k_T algorithm with $\rho = -1$ [108] and the Cambridge-Aachen algorithm with $\rho = 0$ [109], the behaviour of which is shown in Figure 4.5.

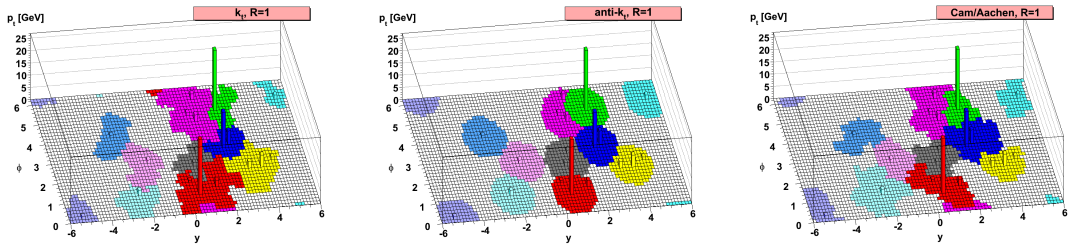


Figure 4.5: Depiction of the three jet clustering algorithms mentioned, using the same input data and the same jet radius. The k_T algorithm has irregular jet shapes, and the use of the anti-k_T algorithm results in conical jets, showing its preference for hard radiation [108].

For small-radius jets ($R = 0.4$), which is the default reconstruction radius used in ATLAS, Particle Flow Objects (PFOs) are created from combined track and calorimeter information. Large-radius jets ($R = 1.0$) are clustered from Unified Flow Objects (UFOs), which are improved PFOs where track information is used to split up large clusters based on jet-substructure (energy flow and their direction), which improves jet mass resolution at high p_T [110].

Hadronic jets are clustered according to the anti-k_T clustering algorithm [108], and are dependent on the jet-radius for the flow objects used in the reconstruction. Charged-particle hits in the ID are used to reconstruct particle tracks with quality criteria applied to ensure the use of well-reconstructed tracks [111]. Information from the (hadronic) calorimeters are built on 'topoclusters': three-dimensional groupings of topologically connected calorimeter cells [112].

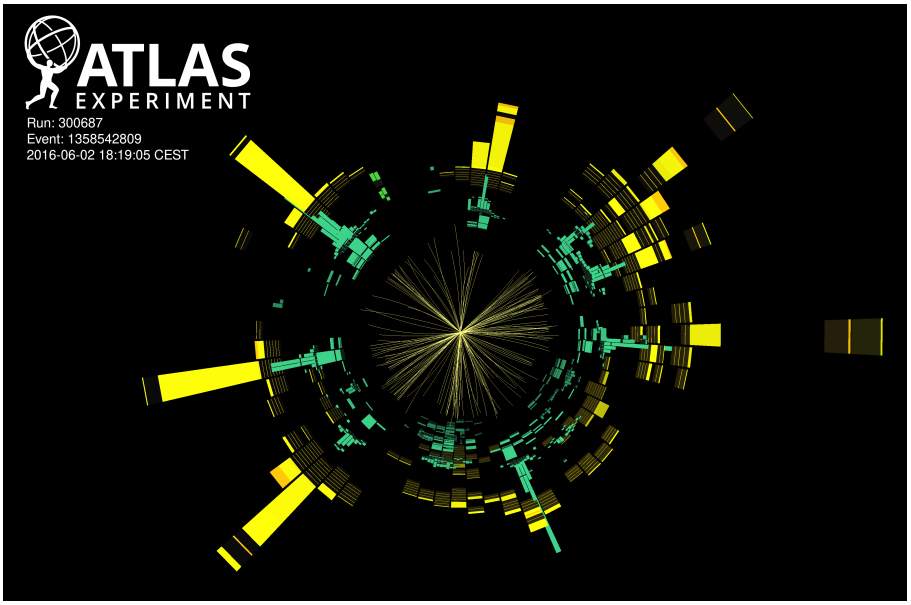


Figure 4.6: ATLAS event display for a multi-jet event [113].

4.4.2 Electrons and Photons

Initial electron candidates are reconstructed by matching tracks made in the ID (with energy loss due to Bremsstrahlung taken into account) to topological clusters from the EM and hadronic calorimeters. Initial photon candidates are more complicated, are are split up into converted or unconverted objects. Converted photon objects are photons that have pair produced before the ECAL and unconverted photons only pair produce in the ECAL, since approximately 30% of photons convert in the detector material before reaching the LAr calorimeter. A converted photon object is based on an EM topo-cluster that was matched to a conversion vertex, while an unconverted photon is reconstructed from a cluster than is not matched to a conversion vertex or an electron track.

Initial clusters and their (matched) candidates are then used to build the final EM clusters. For all photon and electron candidates, EM clusters that are close together are merged to form the final cluster, since energy losses due to Bremsstrahlung mostly happen in the bending (transverse) plane. Prompt electrons and photons are defined to stem from the hard-scattering vertex, or from decays of heavy-resonant Higgs, W and Z bosons, where prompt is used in the sense that these particles are created immediately after the collision, before quarks and gluons have had time to form hadrons.

Electron and photon identification is split up into Loose, Medium and Tight selections, with Loose having the most signal acceptance but the most background, and Tight losing signal acceptance but with increased suppressed background. Electrons identification is made in a likelihood classifier, while the first two photon identifications are applied in the trigger [114].

Isolation requirements are also applied to electrons and photons, where variables measuring the activity in the surrounding area of the electron or photon candidate are constructed. This is usually done by summing the transverse energies of clusters in the calorimeter or the transverse momenta of tracks in a cone of radius $\Delta R = \sqrt{\Delta(\eta)^2 + (\Delta\phi)^2}$ around the direction of the electron and photon candidate, excluding the candidate itself [115].

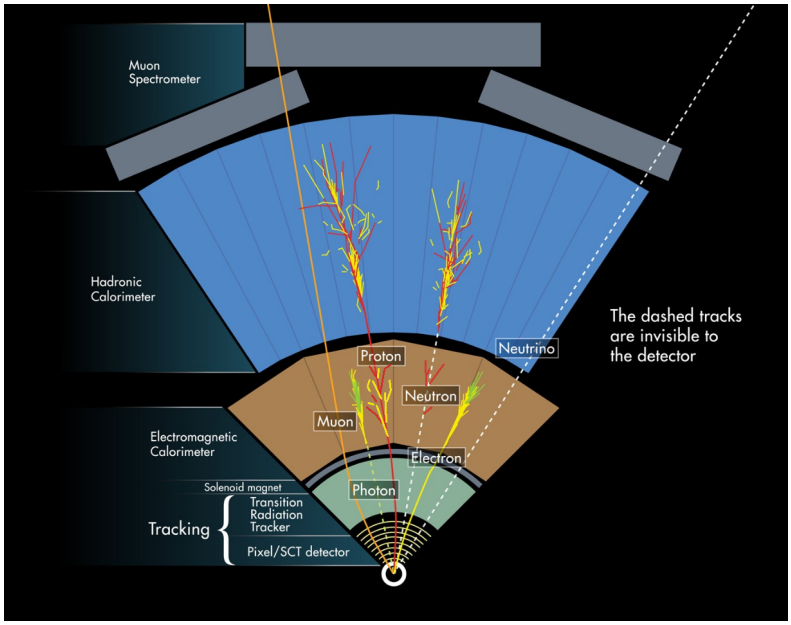


Figure 4.7: Schematic diagram of the different layers of the ATLAS detector, showing the sub-detectors and the particles that interact with them [117].

4.4.3 Muons

Muon reconstruction algorithms use information from the MS and/or the ID. Three broad reconstruction algorithms are used, based on the information from the ID and MS. ID tracks are tracks reconstructed using ID hits only, while Stand-alone tracks (SA) are muon candidates with tracks that are only made using MS hits. These tracks are extrapolated to the beam spot, taking into account the energy loss and multiple scattering in the material before the MS, to define the kinematic quantities at the interaction point. Combined tracks (CB) are tracks from muon candidates where the MS track is matched to an ID track. Muon reconstruction has different working points, the most common being the Medium WP that only selects CB muons in a certain part of the detector range and rejects poorly reconstructed tracks. Isolation criteria are also applied to muons, and can be measured using the ID (through ID tracks), the calorimeters (with topological cell clusters), or a combination of both [116].

4.4.4 Missing Transverse Momentum

Reconstructed missing transverse momentum p^T_{miss}, acts as the "detector signature" for invisible particles and is calculated as the negative vector sum of the p_T of objects in the event. The magnitude of this vector is known as the missing transverse energy. SM neutrinos pass through the detector without interacting with any of the sub-detectors, and are therefore invisible to the detector. Similarly, stable dark matter candidates that do not interact with the detector also contribute to the MET measurement. A distinction is made between "real" MET, from neutrinos and stable DM candidates, and "fake" MET that come from pileup, detector resolution and acceptance.

4.5 It's All About the Rates or A Summer Working on the Trigger Menu

The rates of chains and streams in the trigger Menu can be analysed to ensure that the rate limitations of the HLT are not exceeded and that the Menu is operating optimally. This is done using the Rates Analysis package, a suite of tools for trigger rates calculations, which is found in Athena. Rate predictions are run on an Enhanced Bias[2] dataset [118], the results of which are used by the Rulebook to calculate the prescales that are applied in data-taking. The actual rate output of different chains and streams can then be analysed to control or improve the resource allocation to each chain. The trigger Menu is periodically being updated to include new triggers and optimise streaming. Each time this is done, the rates analysis should be performed to check the output rates of updated streams and chains.

The streaming model is inclusive and so chains can be written to multiple streams, and the same events can be recorded in different streams. The *overlap* between two streams is a measure of how many events are written into the streams before being processed, and the overlap should be minimised as to not waste resources. The contribution of a chain to a stream can also be determined, as well as the overlap between two chains. It is also possible to create a set of chains and find the unique rate of the set with respect to the entire Menu.

The work presented here is the result of the development of a script that automatically calculates different contributions of chains to streams, and was completed during the course of the Summer Student Programme at CERN.

4.5.1 Developing an analysis of rate usage

The process of performing the rates analysis on chains and streams is repeated on a regular basis, and a script that can perform an analysis of the rate usage is a useful tool to facilitate these analyses. This section details the development of a script that adds four functionalities to be used on top of the Rates Analysis package. The four functionalities are calculating the:

1. overlap between two streams
2. unique contribution of a chain to a stream
3. overlap between two chains
4. unique rate of a set of chains

4.5.2 Overlap between Two Streams

By performing the analysis on the chosen streams, trigger Menu experts can decide whether or not chains from a chosen stream should be moved into a different stream to avoid wasting resources due to duplication. This is done by finding the *unique stream rate and overlap between streams* of the selected stream. To do this, the script enables all chains in Stream A

[2]An enhanced bias dataset is overweighted in high-p_T events which are likely to be selected by the trigger system. The data is taken with an invertible trigger menu such that a single weight is calculable per event which corrects for the prescales applied during the enhanced bias data taking and restores an effective zero bias spectrum. This dataset is useful when performing rate estimations on the data of the type typically selected by the HLT.

(which as a default is set to Main[3], but can be changed to any other stream) and Stream B (which can be any other stream), determines the Global HLT Rate for the combination, and then subtracts the rate when only chains in Stream A are enabled.

The script takes two flags `--stream0` and `--stream` as arguments and creates two prescale files: one where only Stream A is enabled, and one where Stream A and Stream B are enabled. Stream A is the reference stream (passed by `--stream0`), and as a default is set to Main. A different reference chain can be chosen by passing it as an argument after this flag. A list of streams can be passed as an argument to `--stream`, and the script iterates over the list. It then calls the `run_RatesAnalysis.py` script (already included in the Rulebook and which calculates the rates of all the chains in the Menu, based on a specific prescale set) and runs the script for each combination of Stream A and Stream B, and writes a text file with the Global HLT Rate for Stream A only, the Global HLT Rate for Stream A and B, and calculates the difference between the rates to get the unique rate of Stream B. For bookkeeping and keeping track of which streams were compared, the script creates a directory for each pair that is compared, and inside that has two directories for the `stream0` and `stream` RatesAnalysis outputs. The information for the unique rate and the overlap is stored in a text file in the directory for each iteration.

The `run_RatesAnalysis.py` script also has the option of giving the rate error of a stream or individual chains, up to four decimal places. The errors presented in the examples below are Poisson in nature. A detailed discussion of the error analysis performed in the script is beyond the scope of this project.

Example: Overlap between the stream0 and three other streams

The example illustrates the use of the script by analysing the stream overlap between the Main stream and three other streams, running over 100 000 events from data processed with a specific Athena release. The Main stream needs to be processed immediately during data-taking, and if the overlap between the streams are high, it can be considered to move chains to one of the other streams.

The results are shown in Table 4.1:

Stream	Rate (Hz)	Error (Hz)	Unique Rate w.r.t. Main (Hz)
Main	2160.1456	53.1707	
Stream 1	347.3337	22.6622	240.7915
Stream 2	475.1429	96.4235	449.3020
Stream 3	6858.5519	202.172	5907.5888

Table 4.1: Table showing the overlap between stream0 and three other streams.

We see that the overlap between Main and Stream 1 is 30.67%, while Stream 2 has an overlap of 5.43% and Stream 3 has an overlap of 13.87%.

[3]The Main stream is a collection of events or event fragments that is typically used in data analysis and Data Quality assessment.

4.5.3 Unique Contribution of a Chain to a Stream

The unique contribution of a chain to a stream can be used as a survey to see if any chains should be moved to a different stream. If a primary chain in the Main stream has an unusually high rate, the chain could be moved to a delayed stream to optimise resource usage. The events would then be processed at a later time when resources are available. This is done as to not slow down the processing of the Main stream data. The setup for this analysis was similar to that of the stream overlap, but the script enables chains in the given stream (with the chain selected enabled), gets the prescales for the chains and then determines the Global HLT Rate of the stream. The script then gets another prescale file in which the given stream is enabled but the chain is *disabled* and subtracts this rate from the Global HLT Rate. The result is then the unique rate contribution of the chain.

An extra functionality of the script is that chains can be added using RegEx[4] by passing the argument `regex` to the flags `--chain`, `--chain_comp` and `--chain_set`.

Example: Jet Chain

In this example, we found the overlap between a jet chain and the given stream. The analysis ran over 500k events in the processed dataset for Athena release 24.0.52. The chain requires a single jet ($p_T > 100$ GeV), with a central eta tag (eta value between 0 and 240, meaning that the jet is in the central part of the detector) and requires that the chain reconstructs particle flow jets which needs full scan fast track finding [119]. The chain is only fed to the Main stream, and the results are shown in Table 4.2.

	Rate (Hz)	**Rate Error (Hz)**
Chain	38.4361	0.9789
Stream and Chain	2518.1376	38.8825
Stream w/o Chain	2479.7015	38.811
Unique Contribution	38.4361	—

Table 4.2: Table showing the unique contribution of a jet chain to the Main stream.

The unique rate of the chain is taken from the menu with the chain enabled, and is given as 38.4361 Hz. This is the same value as the chain rate, since the chain under consideration was only fed to the Main stream.

Example: DarkJet Chain

Considering a chain that is similar to the one outlined in the previous example, except that it has a Dark Jet requirement, the unique contribution of the Dark Jet chain to the Main stream was analysed. Note that the chain is not fed into the Main stream, but rather the DarkJetPEBTLA stream. The results are shown in Table 4.3.

Example: Muon Chain

In this example, we consider a muon chain that is fed into the BPhysDelayed stream and the Main stream. The results are shown in Table 4.4.

[4]A Regular Expression (shortened to RegEx) is a sequence of characters that specifies a match pattern in text.

	Rate (Hz)	Rate Error (Hz)
Chain	2.3314	0.052
Stream and Chain	2494.3401	44.9878
Stream w/o Chain	2494.3401	44.9878
Unique Contribution	0.0000	—

Table 4.3: Table showing the unique contribution of a Dark Jet chain to the DarkJetPEBTLA stream.

	Rate (Hz)	Rate Error (Hz)
Chain	22.4568	5.7983
Stream and Chain	2348.8865	54.587
Stream w/o Chain	2344.4024	54.5254
Unique Contribution	4.4841	—

Table 4.4: Table showing the unique contribution of a muon chain that is fed into the BPhysDelayed and Main streams.

The muon chain selected has a unique contribution of 0.19% to the Main stream.

4.5.4 Overlap between Two Chains

Calculating the overlap between two chains is a useful tool for trigger experts and developers of new triggers to see if events pass multiple chains and if the overlap between the chains is too large. There is one prescale file where only one chain is enabled and everything else in the menu is disabled, and another prescale file where both chains are enabled. The script has the option of comparing multiple chains to a single reference chain. The chains are entered as a list and the user does not need to run the script for each comparison chain.

Example: Jet Chains

In this case, the prescales are set to 1, however the user could change the values in the input prescale file. The example considers jet chains with the same L1 seed that requires a minimum p_T of 160 GeV, with the reference chain having a p_T cut of 360 GeV at the HLT level, and the three comparison chains having increasing p_T cuts. The results are shown in Table 4.5. We

	Weighted PS Rate (Hz)	Unique Rate (Hz)
Reference Chain	90.0203	45.8392
Comparison Chain 1	44.1811	0.0000
Reference Chain	90.0203	54.7757
Comparison Chain 2	35.2447	0.0000
Reference Chain	90.0203	62.7814
Comparison Chain 3	27.2390	0.0000

Table 4.5: Table showing the overlap between two jet chains.

see that the weighted PS rate (the rate of the chain after the prescales have been applied) for the reference chain is the same in each comparison. The weighted PS rate of the comparison chain, plus the unique rate of the reference chain, adds up to the weighted PS rate of the

reference chain. The comparison chains have no unique rate, because if an event passes their selection criteria, it also passes the selection criteria of the reference chain.

It follows that the weighted PS rate of the comparison chains decrease as the selection criteria of the chains become stronger, and subsequently we see that the unique rate of the reference chain increases as the jet p_T cut increases. The percentage overlap of the reference chain with the three comparison chains is 49.07%, 39.15% and 30.25%.

Example: Similar Electron Chains with Different Selection Criteria

In this example, the reference electron chain has a higher L1 selection criteria (a p_T greater than 28 GeV) than the comparison chain (a p_T greater than 26 GeV), and a higher HLT p_T threshold (30 GeV as opposed to 28 GeV). The results are shown in Table 4.6.

	Weighted PS Rate (Hz)	Unique Rate (Hz)
Reference Chain	864.4192	678.3463
Comparison Chain	227.7408	41.6680

Table 4.6: Table showing the overlap of two similar electron chains with different selection criteria.

The rates show that there is indeed an overlap of 26% between the two chains.

4.5.5 Unique Rate of a Set of Chains

The unique rate of chains is displayed in the standard Rates Analysis results, but the way that it is determined means that if an event triggers multiple chains, it does not contribute to the unique rate of the chain. It then appears that a set of chains has no unique rate although this set of chains selects events which are not selected by any other chain in the menu. In analogy to the streams analysis, we define our set of chains as a "stream" and perform the rates analysis on the full menu, and then the rates analysis when all of the chains in the set are disabled. The difference in the Global HLT Rate is then the unique rate of the set. This is in particular useful for developers planning to add multiple chains to the menu, e.g. a mix of primary and support chains targeting a specific analysis signature.

Example: Displaced Vertices

The set of chains contains the tag `"hitdv"`, meaning we look for hits with displaced vertices. For this set of 20 chains, the script was on 500k events from processed output data files. The results are shown in Table 4.7.

The unique rate of the hitdv set is 0.1330 Hz for the changed and unchanged prescale files.

	Global HLT Rate [Hz]	Global HLT Rate Error [Hz]
Full Menu Enabled	9762.7216	116.9259
Chains Disabled	9762.5886	116.9224
Unique Set Rate	0.1330	

Table 4.7: Table showing unique rate of a set of chains with a displaced vertex selection criteria.

4.5.6 Conclusion

The studies performed in Section 4.5 were completed over the course of the Summer Student Programme at CERN, along with the development of a script that automatically analyses the rate usage of the ATLAS Trigger Menu. This required a good understanding of the ATLAS Trigger System, as well as internal tools used in the development and operation of the Trigger Menu and System as a whole. The script has been implemented into the Athena Software releases and can be used by Menu developers to perform their own analyses on rate usage.

5 ATLAS Search for a Maverick Top Partner Decaying to a Dark Photon

This chapter focuses on an ATLAS search for a top-partner vector-like quark, called the Maverick top partner, that decays into a Dark Photon, which in turn decays into a highly-collimated pair of leptons. The model was first proposed in Reference [120] and further explored in Reference [121],

5.1 Vector-like Quarks

Vector-like Quarks (VLQs) are introduced as a new hypothetical quark isosinglet, or spin-1/2 fermions. They are singlets of $SU(2)$ with charge -1/3 and/or +2/3, and both left- and right-handed components transform in the same way under the gauge group [122]. Mass terms of the form $M_U \bar{U}_L U_R$ and $M_D \bar{D}_L D_R$ arise[1], and are included in the gauge-invariant Lagrangian. These mass terms introduce a new scale V, which can be significantly higher than the Higgs VEV v, and above the EWSB scale, thereby populating the expansive desert between the v and some higher energy scale [123] and addressing parts of the hierarchy problem. VLQs mix with the SM quarks to regulate the Higgs mass, and are naturally suppressed by the ratio of $\frac{v}{V}$. VLQs are expected to be around the TeV scale, and to mix primarily with the t and b quarks. Due to the large Yukawa coupling of the top quark, it is expected that the lightest new VLQ states are partners of the top itself [124] and connects the top quark to most New Physics models involved in EWSB and the fermion mass hierarchy. These VLQs are then further specified to be top partner VLQs, or simply top partners.

Production modes of VLQs are split up into three groups: pair production, single production in association with other particles and mono production, as shown in Figure 5.1. Pair production mostly takes place in QCD interactions and is only dependent on the mass of the new fermion, while single VLQs can be produced in association with top quarks, jets (until a further discussion is section 4.4.1, a jet simply refers to the other five (light) quarks), or a boson, specifically $W^{\pm}, Z, H$. The single production is model dependent. The mono production through gluon chromomagnetic coupling happens via a loop-induced operator, and this operator also contributes to the single production with tops and jets. For VLQ masses larger than 1 TeV, single production is favoured, particularly because the cross-section is higher than that for pair production, and the coupling to SM particles are free parameters, albeit constrained [125].

[1] U represents up-type VLQs and D represents down-type VLQs.

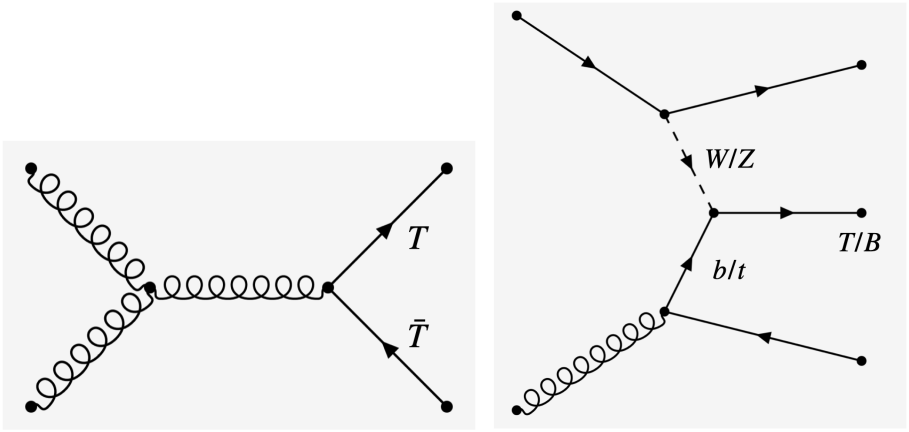


Figure 5.1: Representation of two of the VLQ production modes. The diagram on the left shows the QCD pair production ($gg \rightarrow TT$), and the diagram on the right shows the production of a single VLQ with an associated particle, in this case quarks.

VLQ decay modes were traditionally theorised to be to SM electroweak bosons ($W^{\pm}, Z$) and the Higgs boson, and have many complex final states to drive searches. Extensive searches by two of the collaborations at the Large Hadron Collider (LHC), ATLAS and CMS, have not found evidence for VLQs using these traditional decay modes [125, 126].

5.2 Dark Photons

Dark Photons (DP) are hidden-sector gauge bosons, akin to the photon, that kinetically mix with the SM photon through a vector portal [77]. They are charged under a new $U(1)_d$ gauge group that acts as an extension to the SM. The type and dimension of the operators classify the vector portal, which highlights the significance on the spin of the mediator. DPs are accordingly classified as spin-1 vector bosons, and it is via this vector portal that we can detect them. The portal acts as a link between normal matter and dark matter by the kinetic mixing of the visible and dark gauge bosons. The kinetic mixing therefore links the visible and dark sectors, and so we can access the dark sector in particle colliders [77].

The general (kinetic) Lagrangian of two Abelian gauge bosons, charged under the symmetry groups $U(1)_a$ and $U(1)_b$ is:

$$\mathcal{L} = -\frac{1}{4}F_{a\mu\nu}F_a^{\mu\nu} - \frac{1}{4}F_{b\mu\nu}F_b^{\mu\nu} \tag{1}$$

Assuming that the gauge boson that couples to the current J_μ of the SM is A_b^μ, and the gauge boson coupling to the current J'_μ of the dark sector is A_a^μ, the Lagrangian takes the form:

$$\mathcal{L} = eJ_\mu A_b^\mu + e'J'_\mu A_a^\mu \tag{2}$$

where e and e' are the respective coupling constants. DPs can be massive or massless, the latter of which is mostly discussed in the literature. The focus on massive DPs is motivated by its direct coupling to the SM electromagnetic current, while also coupled to the dark sector. The Lagrangian of the interaction between the massive DP and the SM is subsequently given by:

$$\mathcal{L} = -\epsilon eJ^\mu A'_\mu$$

where the electromagnetic current is represented by J^{μ} and ϵ modulates the strength of the interaction. The kinetic mixing between the DP and the photon in the SM is possible because the electromagnetic current for the DP is the same as the electromagnetic current in the SM [77].

The massive DP can be produced in the same way as SM photons, through Bremsstrahlung, annihilation of electron-positron pairs, meson decays and via the Drell-Yan process. In the Drell-Yan process, the DP decays leptonically to a lepton-antilepton pair, or hadronically to a hadron-antihadron pair. The different production modes are shown in Figure 5.2

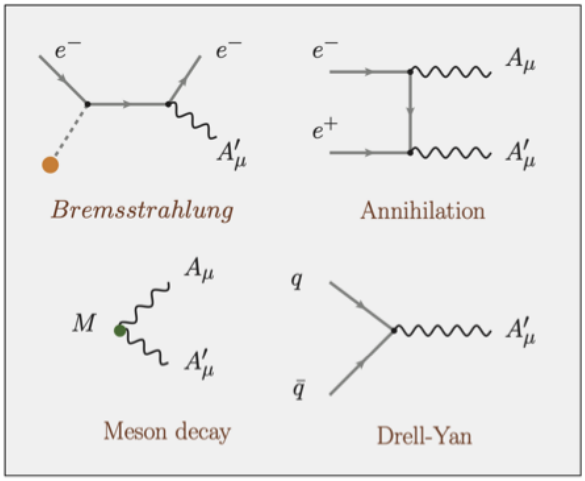


Figure 5.2: Production mechanisms of massive dark photons (A'_μ), taken from [77].

Massive DPs can further be classified as visible or invisible. Visible DPs are required to have a mass $m_{A'} > 2m_e \simeq 1$ MeV, so that their decay products are visible in particle detectors, the lightest of which is an electron-positron pair. Invisible DPs decay into other DM states, and are under the mass threshold of 1 MeV.

For experimental searches, the parameter space depends on two parameters: the DP mass, $m_{A'}$, and the mixing parameter ϵ, which describes the mixing between the DP and the SM photon. Searches for DPs in accelerators and colliders broadly fall into one of three categories - visible final state detection, missing energy/momentum techniques or missing mass techniques. In the case of the latter two, the missing momentum and energy or missing mass that are due to the presence of invisible particle(s) are measured. This requires precise knowledge of the initial and final states, and these search strategies are better performed at fixed-target experiments and electron-positron colliders, and not at circular hadron colliders like the LHC.

Visible final state detection is therefore more interesting for the experiments based at the LHC. The signature for a DP produced would be a narrow resonance (bump) over an irreducible background, but their detection is heavily reliant on the different decay modes, as proposed by different models. Collider experiments are sensitive to larger couplings of ϵ, and the detectable rate of DPs is proportional to ϵ^4. High-luminosity colliders like the LHC are needed to overcome this suppression of small couplings.

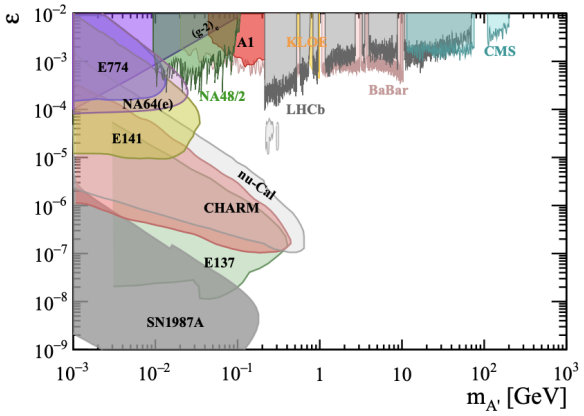


Figure 5.3: Current limits on the massive DP for masses above 1 MeV from di-lepton searches. The searches were performed at collider experiments, beam dumps and fixed-target experiments. Limits from $(g-2)_e$ and supernovae are also included [77].

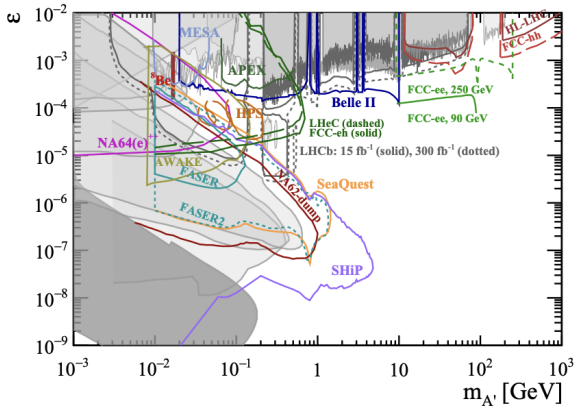


Figure 5.4: Considering massive DPs with $m_{A'} > 1$ MeV. Colored lines represent projected limits for existing and proposed experiments. The gray shaded areas are existing limits [77].

The decay width for leptonically decaying DPs is calculated by:

$$\Gamma(A' \to l^+ l^-) = \frac{1}{3}\alpha\epsilon_c^2 m_{A'}\sqrt{1-\frac{4m_l^2}{m_{A'}^2}}\left(1+\frac{2m_l^2}{m_{A'}^2}\right)$$

This decay channel is only accessible to DPs with $m_{A'} > 2m_e \simeq 1$ MeV.

Experiments based at the LHC have been searching for Dark Photons that decay into a lepton pair. ATLAS has searched for DPs that decay into pairs of electrons or muons using 139 fb^{-1} of data [127, 128], while LHCb has searched for DPs that decay into two muons [129, 130] using 1.6 fb^{-1} of data at a centre-of-mass energy $\sqrt{s} = 13$ TeV, and CMS performed the same search with fully reconstructed data, as well as data collected with a reduced trigger information [131]. These searches are the most recent constraints that we have for DPs that decay into two muons, and place limits on the parameters $m_{A'}$ and ϵ. These current and expected limits are shown in Figures 5.3 and 5.4.

5.3 Theoretical Framework

The model explores a up-type (top partner) VLQ, T, charged under a new Abelian $U(1)_d$ gauge force which kinetically mixes with the SM hypercharge. The gauge boson of the $U(1)_d$ force is the dark photon, γ_d and the VLQ undergoes a non-traditional decay to a DP or a dark Higgs, assuming a Higgs mechanism in the dark sector exists. The SM is therefore extended, and the group representation becomes $SU(3) \times SU(2)_L \times U(1)_Y \times U(1)_d$. T has charge $+1$ under this symmetry, and SM particles are singlets. T is a singlet under $SU(2)_L$ with hypercharge $Y = \frac{2}{3}$. The field content under this extension is given in Table 5.1.

	$SU(3)$	$SU(2)_L$	Y	Y_d
t_{1R}	3	1	2/3	0
b_R	3	1	-1/3	0
$Q_L = \begin{pmatrix} t_{1L} \\ b_L \end{pmatrix}$	3	2	1/6	0
Φ	1	2	1/2	0
T_L	3	1	2/3	1
T_R	3	1	2/3	1
H_d	1	1	0	1

Table 5.1: Field content and the charges they posses. The third generation quarks are t_{1R}, b_R and Q_L, T is the $SU(2)_L$ singlet, Φ is the SM Higgs doublet and H_d is the $U(1)_d$ Higgs field. The SM hypercharge is denoted by Y, and Y_d is the $U(1)_d$ charge.

Reference [120] has a full discussion of the Lagrangians and the interactions, but a simple discussion follows here. The inclusion of the additional gauge field means that the following parameters are added to the usual SM parameters: the VLQ mass m_{VLQ}, the mass of the dark photon m_{γ_d}, the dark Higgs mass m_{H_d}, the VEV of the dark Higgs v_d, the mixing parameter ϵ, the mixing angle between the VLQ and the SM top quark $\sin\theta_l^t$ and the scalar mixing between the dark and SM Higgs $\sin\theta_s$.

Motivation for the new $U(1)_d$ force comes from the fact that DM may have interact with itself through this new force, and the kinetic mixing with the SM hypercharge that allows decays to SM fermions. The kinetic mixing is generated via fermions that are vector-like and are charged under $U(1)_d$ and the SM hypercharge. The kinetic mixing is small if the mass of the DP is much less than the electroweak scale, and the DP has a coupling to SM fermions of the form ϵJ^μ_{EM}, where ϵ is the kinetic mixing parameter ad J^μ_{EM} is the SM electromagnetic current. The kinetic mixing only occurs between the third generation SM quarks and T to avoid flavour constraints.

The gap between the mass of the SM top quark t and the top partner T can be small for the branching ratios of VLQs into the dark sector and SM quarks to be enhanced, as opposed to the case where down-type or bottom partners are considered, as in Ref [132]. The partial width of T decaying into a final state composed of only SM particles, or a traditional decay, is given as:

$$\Gamma(T \to b/t + W/Z/H) \sim \sin^2\theta \frac{M^3_{VLQ}}{v^2_{EW}} \tag{3}$$

M_{VLQ} is the mass of the top-partner, θ is the mixing angle between t and T, and v_{EW} is the Higgs VEV (246 GeV). Assuming that a dark sector Higgs mechanism exists, and that the

top-partner is charged under the dark force, the partial width of T into a DP or a dark Higgs h_d is given by:

$$\Gamma(T \to t + \gamma_d/h_d) \sim \sin^2\theta \frac{M_{VLQ}^3}{v_d^2} \tag{4}$$

with v_d the VEV of the dark Higgs boson. Taking the ratio of these two rates:

$$\frac{\Gamma(T \to t + \gamma_d/h_d)}{\Gamma(T \to b/t + W/Z/H)} \sim \left(\frac{v_{EW}}{v_d}\right)^2 \tag{5}$$

If considering light DPs, or DPs with $m_{\gamma_d} < 10$ GeV, the value of the dark VEV v_d is also less than 10 GeV. The ratio of decays into DPs to decays into purely SM final states is then greater than $\mathcal{O}(100)$. The mass gap between the SM electroweak bosons and the dark sector bosons means that the VLQs preferentially decay into light dark sector bosons (γ_d or h_d). The quadratic dependence of the ratio means that the mass gap does can be small for the decay to the dark sector to be favoured.

The different production modes for the VLQ in the model are shown in Figure 5.5. The VLQs can be produced in pairs, which is dominated by QCD and is determined by the $SU(3)$ gauge interactions. The production of a single VLQ particle (with a quark) relies on the mixing angle $\sin\theta_L^t$ between the VLQ and the SM quarks, more specifically the production cross-section is proportional to $(\sin\theta_L^t)^2$. This is suppressed for small $\sin\theta_L^t$. For $\sin\theta_L^t \sim 0.1$ the single production of the VLQ is favoured over the pair production. T is charged under the new $U(1)_d$ gauge group and the SM, and this allows the decay of T to a top quark and a DP or a dark Higgs boson, shown in Figure 5.6. If the mixing parameter ϵ is small, the mass of the DP is significantly lower than the EW scale and the VLQ has a high mass, decay to a DP is preferred over the decay to a dark Higgs boson. The model results in a interesting experimental situation: searches for light dark sectors (the DPs) can be connected to searches for new heavy particles (the VLQs).

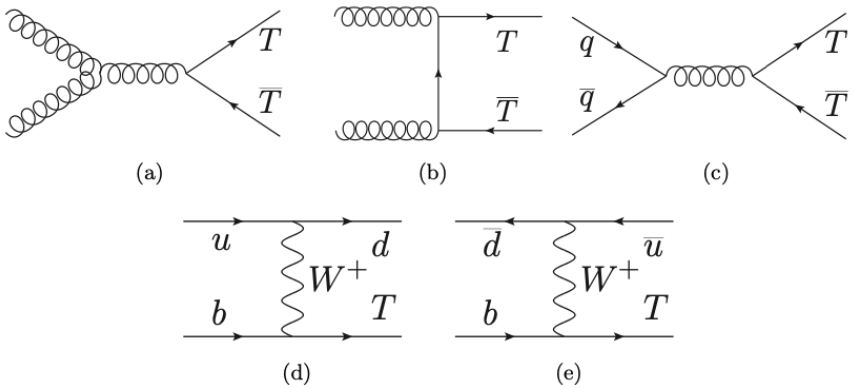


Figure 5.5: VLQ production modes in the model. a) through c) show the pair production modes, while d) and e) show the single production that is studied in the analysis. Taken from [120].

The most encouraging signature for $T \to t\gamma_D$ is in the leptonic decay of the DP. This has the added benefit of avoiding the large multi-jet backgrounds. If the mass of the DP is assumed to be a lot less than the mass of T, or $m_{\gamma_d} \ll m_T$, the DP is highly boosted and this

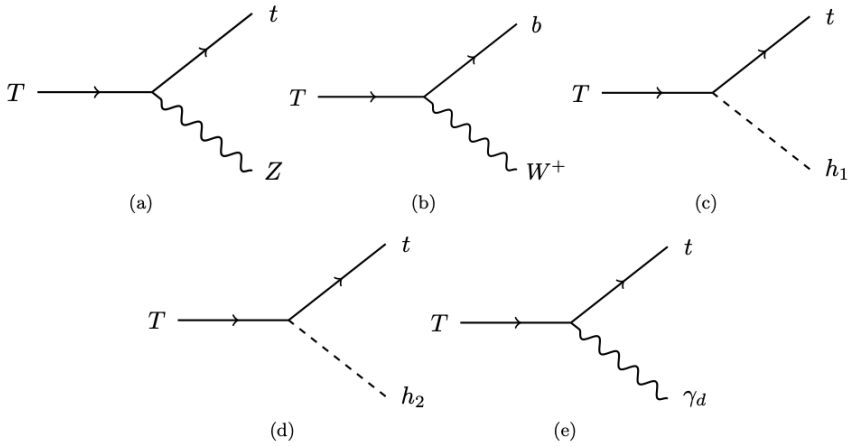


Figure 5.6: Possible VLQ decay modes. (a) through (c) show the traditional decays to EW bosons and the Higgs boson, while (d) and (e) show the decay of the VLQ to a dark Higgs boson and a DP. The analysis focuses on the decay of the VLQ to the DP. Taken from [120].

leads to highly collimated decay products. The angular separation of the leptons can then be calculated by:

$$\Delta R_{ll} \sim \frac{2M_{\gamma_d}}{E_{\gamma_d}} = \frac{4M_{\gamma_d}}{M_{VLQ}} = 4 \times 10^{-3} \left(\frac{M_{\gamma_d}}{1\text{ GeV}}\right) \left(\frac{1\text{ TeV}}{M_{VLQ}}\right) \quad (6)$$

where ΔR_{ll} is defined as in Equation 1. The two leptons are difficult to isolate at such small angular separations, and give rise to a collider signature called a lepton jet.

5.4 Lepton Jets in ATLAS

Lepton jets are non-standard detector objects used to reconstruct highly-collimated leptons, or leptons with very small angular separation. Lepton jets are defined as originally having at least two leptons, with small angular separations and GeV-scale invariant masses [133]. The leptons are the decay products of the highly-boosted (high-p_T) DP, causing this small angular separation. Reconstructing these lepton jets poses challenges in the ATLAS detector. The detector lacks the angular resolution to separate the nearly-overlapping leptons, even after combining the track information from the ID and the calorimeter inputs for electrons, and the muon spectrometer inputs for muons.

In the case of electrons, lepton jets are reconstructed from clusters of deposited energy in the EM calorimeter. The cluster must be associated to at least one ID track, and the (reconstructed) electron is required to be within a ΔR of 0.2 of a electron trigger object that passes a certain energy threshold. The transverse shower profile of these lepton jet electrons are different to the profiles of isolated electrons produced in W or Z boson decays, due to the overlap (low angular separation) of the electrons [128, 134].

Muon candidates for lepton jets should have tracks in the ID, and have measured momenta in the muon spectrometer. As with electrons, the reconstructed muons are required to be within a ΔR of 0.2 of muon trigger objects.

Lepton jets are not reconstructed using the anti-k_T algorithm [108], but rather the Cambridge-Aachen (CA) algorithm [109]. Lepton jets typically have less constituents than hadronic jets,

and the clustering algorithm starts from the highest p_T lepton. The CA algorithm is therefore better to resolve soft, collimated objects, as is the case for lepton jets. The difference in reconstruction efficiency between the two algorithms is negligible, so the CA algorithm is chosen. The distance measure used to reconstruct the jets, d_{ij}, has no p_T dependence and is solely based on the distance between constituent particles:

$$d_{ij} = \frac{\Delta R_{ij}^2}{R_0^2} = \frac{(y_i - y_j)^2 + (\phi_i - \phi_j)^2}{R_0^2} \tag{7}$$

5.5 Analysis Strategy

5.5.1 Final State Topology and Signal Characteristics

The resulting final state topology of the search is shown in Figure 5.7, and the VLQ is named the Maverick top-partner. The single production of the VLQ requires the associated production of a jet, labelled by q in the diagram. The lepton-jet is labelled by e^+e^-. The analysis focuses on the hadronic decay of the top quark, and so the top jet is shown by encompassing the broad jet with the b-jet and the W boson decay to two quarks.

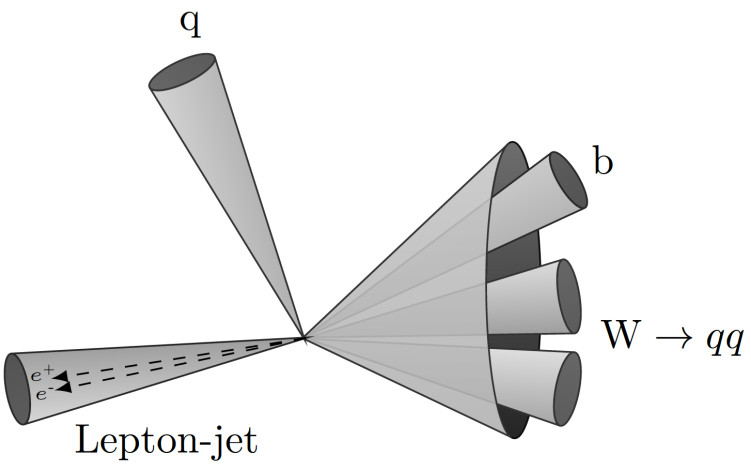


Figure 5.7: Final state topology of the Maverick top-partner search [121].

Different variables can be used to distinguish signal from background. The first class of variables are the angular variables. ΔR, as defined in Equation 1, between the two leading muons[2] is found to be less than 0.1, as illustrated in Figure 5.8. The top jet and the lepton jet are produced back-to-back, and both are boosted. Figure 5.9 shows the angular separation between the two jets, and Figure 5.10 shows the high-p_T behaviour of the lepton jet.

The Maverick top-partner is reconstructed by adding the four-vectors of the top jet and the lepton jet, and the invariant mass plot should peak at the different generated masses, shown in Figure 5.11. The samples were simulated for 1 TeV and 3 TeV masses.

[2]The two leading muons are the two muons with the highest p_T, and are assumed to be the muons in the lepton jet since the lepton jet is boosted.

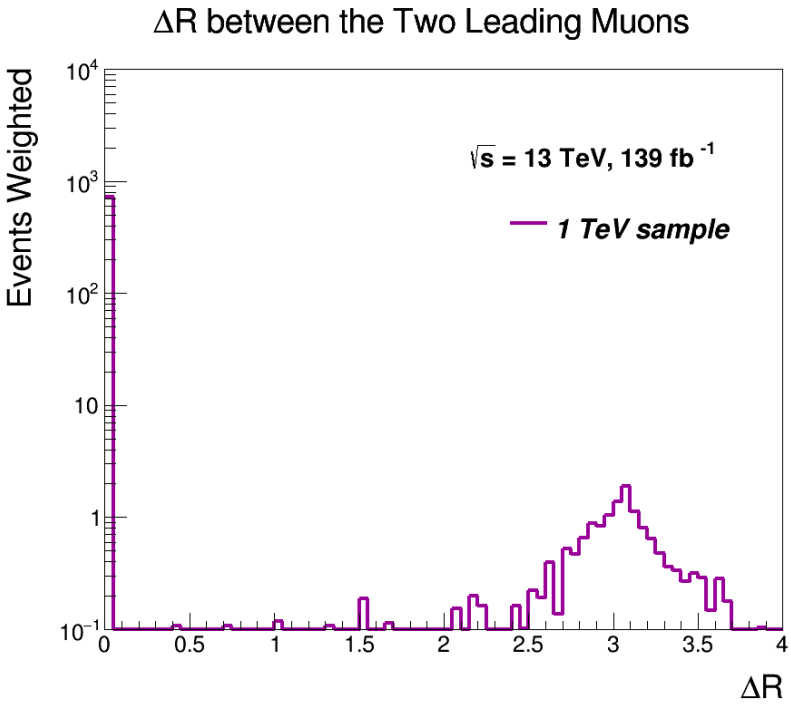


Figure 5.8: The angular separation ΔR between the two leading muons in the simulated sample where the Maverick top mass is 1 TeV. The distribution peaks in the first bin, where $\Delta R < 0.1$, and shows the small angular separation of the muons in the lepton jet. The peak around $\Delta R = \pi$ is due to cases where the sub-leading muon is not in the lepton jet and there are more than two muons in the event.

5.5.2 Event Generation

The simulated samples correspond to the full Run 2 (2015-2018) dataset, with a centre-of-mass energy of $\sqrt{s} = 13$ TeV and an integrated luminosity of 140 fb^{-1}. The samples were required to pass a either large-jet or muon triggers [135], with transverse energy and momentum thresholds.

Simulated MC signal samples are used to prepare the analysis strategy, the background estimation and the signal optimisation. The samples are generated using MadGraph5, interfaced with Pythia8 for the showering, and using the default NN23LO1 PDF set [136], on the UFO file outlined in [120] to produce a Maverick top partner that decays into a DP, which promptly decays to a muon pair. Two samples are generated, with the Maverick top mass set to 1 TeV and 3 TeV, with the VEV of the dark sector Higgs, v_d, set to 10 GeV, and the dark kinetic mixing parameter set to 0.001. Both the mixing angle between the VLQ and the SM top quark $\sin\theta_l^t$, and the scalar mixing angle between the dark Higgs and the SM Higgs $\sin\theta_s$ is set to 0.1. The dark Higgs boson mass m_{H_d} is set to 10 GeV. The DP mass is set to 500 MeV.

Simulated sampled of the SM background processes are used to optimise the event selection before looking at data. The multi-jet background samples are split up into 12 slices, each corresponding to a particular p_T range, and are produced using Pythia 8306, using the same PDF set as the signal samples (NNPDF23LO), with the A14 tuned parameter set [137]. The $t\bar{t}$ samples are produced using the Powheg Box v2 [138–141] generator at NLO, with the h_{damp} parameter set to 1.5 times the mass of the top quark [142] and the NNPDF3.0NLO

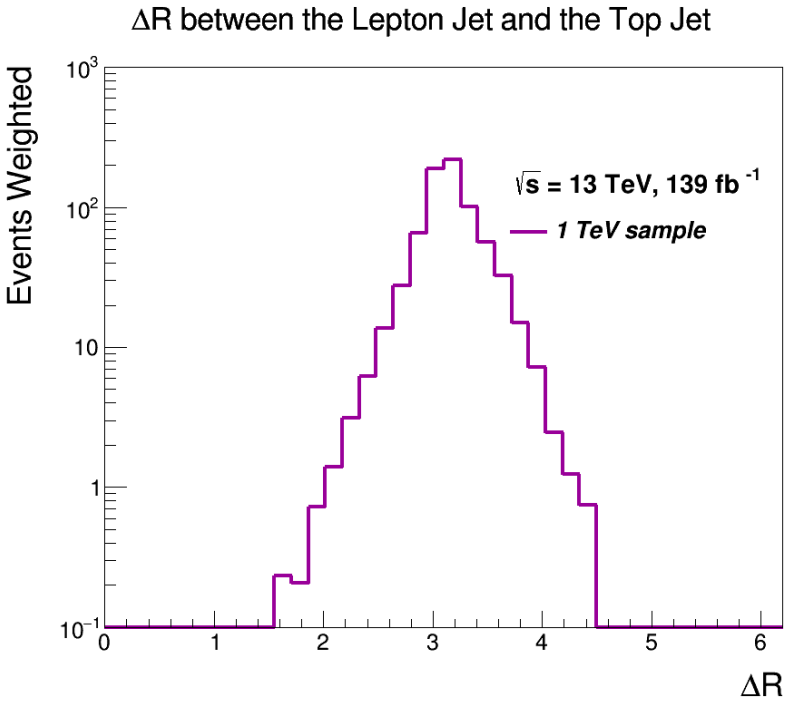


Figure 5.9: The angular separation ΔR between the lepton jet and the top jet in the simulated sample where the Maverick top mass is 1 TeV.

PDF set [143]. Pythia 8.230 [144] was used to model the parton shower, hadronisation and underlying event, using the PDF set NNPDF23LO. The $t\bar{t}$ samples include the all-hadronic and partial hadronic decay of the top quarks. The vector boson production along with jets samples are divided into the production of the Z-boson and the W-boson. The Z+jets samples are generated using Sherpa 2.2.11 [145] generator, with NLO matrix elements for up to two partons, and leading-order (LO) matrix elements for up to four partons. These samples were matched with the Sherpa parton shower [146], using the NNPDF3.0NNLO PDF sets [143] that are normalised to a NNLO prediction [147]. The same generator and setup was used for the W+jets production.

Simulated signal and background samples were passed through the Geant4 [148] toolkit, used to produced a full simulation of the ATLAS detector geometry and detector response [149]. The simulation accounts for pile-up (multiple proton-proton collisions per bunch crossing), and interactions that happen prior to and after the hard-process interaction. The reproduction of the distribution of the average number of interactions per bunch crossing observed in data is achieved by weighting the simulated events.

5.5.3 Object Selection and Event Reconstruction

Events are selected if at least one collision vertex can be reconstructed, using two tracks in the ID with a p_T greater than 500 MeV. The primary vertex is further defined as the vertex with the largest $\sum p_T^2$, if there are multiple vertices with a p_T greater than 500 MeV.

The objects in the final state topology are reconstructed as follows.

Electrons are identified by the association of energy clusters in the electromagnetic calorimeter to tracks in the ID. The electrons are required to have a p_T greater than 4.5 GeV and be

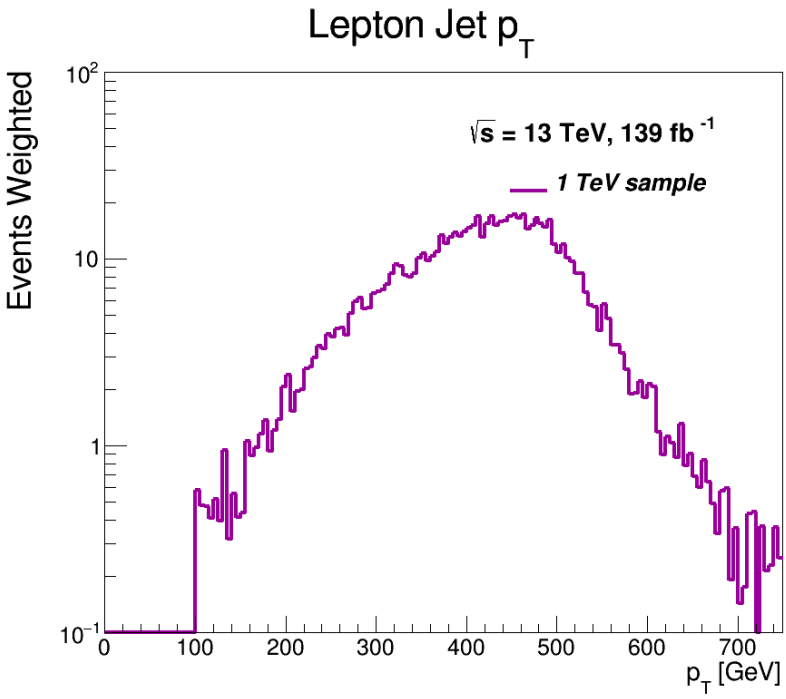


Figure 5.10: The transverse momentum (p_T) of the lepton jet in the simulated sample where the Maverick top mass is 1 TeV, showing its boosted nature.

in the pseudorapidity range of $|\eta| < 2.47$, excluding the range $1.37 < |\eta| < 1.52$ as this is the transition region between the barrel and endcap electromagnetic calorimeters. Muons are reconstructed by combining tracks in the ID and the MS, and have a minimum p_T requirement of 3 GeV. Muons are required to be in the pseudorapidity range $|\eta| < 2.5$. The isolation requirements for muons depend on the track-based or calorimeter-based energy contributions surrounding the muons. An isolation requirement [150] is used in regions where background modelling is performed, and is the standard isolation requirement used in the analysis. The minimum track p_T of this working point is 500 MeV, and requires the following:

$$p_T^{\text{varcone30}} + 0.4E_T^{\text{netflow20}} < 0.16p_T^{\mu} \tag{8}$$

where p_T^{μ} is the p_T of the muon and $p_T^{\text{varcone30}}$ is min(10 GeV/p_T^{μ}, 0.3). E_T^{neflow20} the transverse energy of neutral particle flow objects in a cone of radius ΔR of 0.2 around the muon. This results in the ΔR of the isolation of the muon, and is optimised for topologies where muons are expected to be in close proximity to other energetic leptons and jets. Electrons and muons are at risk of being double-counted, and as prevention electrons that have the same ID-track as a muon are removed.

Hadronic jets are reconstructed using the anti-k_T algorithm [108], with a radius $R = 0.4$. The jets have a minimum p_T requirement of 20 GeV, and are in the pseudorapidity range $|\eta| < 2.5$. Hadronic large-radius jets are reconstructed with the same requirements as the 0.4-radius jets, but are set to have radius $R = 1.0$. Reconstructed jets can be mistaken for electrons, and so jets within an angular distance of $\Delta R = 0.2$ of electrons are removed, and this process is called overlap removal.

Lepton jets can consist of either muons or electrons. Both types are reconstructed using the Cambridge-Aachen algorithm [109]. If a differently-flavoured lepton is found within a cone-radius (ΔR) of 0.4 of the lepton jet, the lepton jet is discarded. This ensures orthogonality

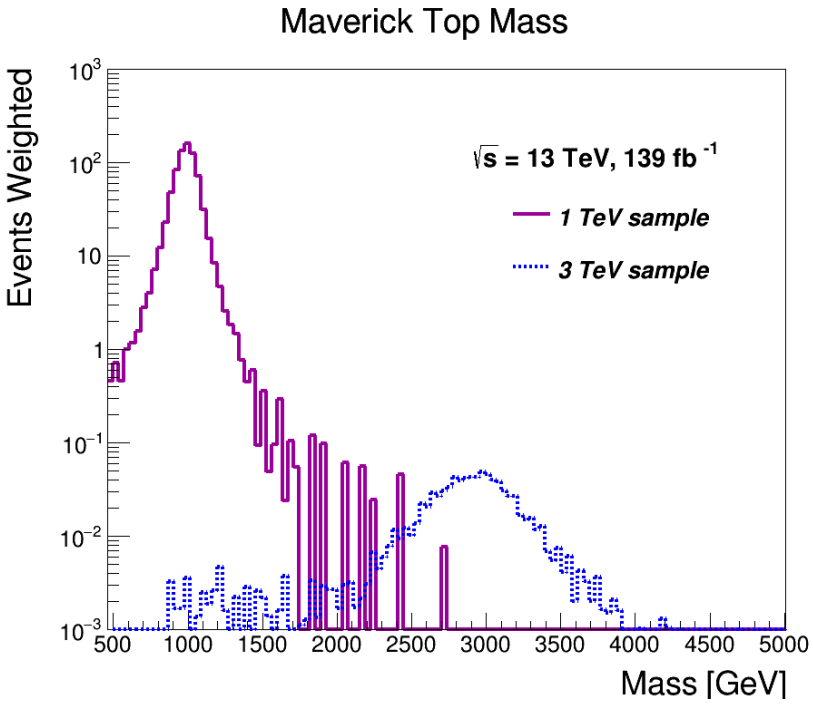


Figure 5.11: Plot of the reconstructed Maverick top mass for the 1 TeV and 3 TeV simulated samples.

between the lepton jet types. The DP is neutral, and so the two leptons originating from its decay should be of opposite charge, however this requirement is not imposed in the analysis. Muon lepton jets are required to have two muons inside the lepton jet[3], while electron lepton jets are required to have at least one electron with two associated ID tracks to the electron(s). Electron lepton jets are further required to be in the pseudorapidity range of $|\eta| < 1.37$, with a leading track p_T greater than 5 GeV. The mass of a lepton jet is defined differently for each type of lepton jet. For muon lepton jets, the invariant mass is the sum of the constituent muon masses, and for electron jets the definition of the mass depends on number of electron objects that are clustered. For two electrons in the lepton jet, the invariant mass is the invariant mass of the system of electrons. For the case of two associated tracks and a single electron, the mass is computed from the ID tracks. Events containing muon lepton jets are in the *muon channel*, and events containing electron lepton jets are in the *electron channel*.

The analysis is for both the muon decay channel and the electron decay channel of the DP, however the focus of this work is placed on the muon channel.

5.5.4 Event Selection

Events are required to have at least one jet with $R = 0.4$, one b-tagged jet, one large-radius jet with $R = 1.0$, one muon and one muon lepton jet. The leading large-radius jet is taken to be the jet representing the top jet, with the added requirement of having a b-tagged jet within a angular distance $\Delta R = 1.0$ of the top-jet axis. The top jet is required to be within the top-mass window, broadly set to between 100 GeV and 250 GeV to account for possible misreconstruction in the detector and to be as inclusive as possible. Due to the boosted nature of the lepton jet, a p_T requirement of 100 GeV is applied, and the lepton jet is required to be

[3]More information can be found in the Muon Studies section (5.6.1).

in the range of $1.5 \leq \Delta R \leq 4.5$ of the top jet.

5.5.5 Contributing Background Processes

The most significant background processes for the analysis are processes with multi-jet final states, $t\bar{t}$ production and processes with vector (W and Z) bosons produced with jets.

The final state for the signal topology has multiple jets, as shown in Figure 5.13a along with the number of jets in each of the background samples, and so the multi-jet final state is the leading background to the signal.

Top quarks are most commonly produced in pairs at the LHC, and the $t\bar{t}$ process is the sub-leading background process. Figure 5.12 shows the possible decay products in the $t\bar{t}$ process. In addition to the multiple jets (shown in Figure 5.13a), the lepton from a leptonically-decaying W-boson could be mistaken for a muon originating from a DP. The branching ratio (BR) of the all-hadronic decay of the $t\bar{t}$ pair is roughly 45%. The lepton plus jet BR (where one W boson decays hadronically, and the other leptonically) is roughly 30%, while the di-lepton (both W-bosons decaying leptonically) BR is roughly 5%. The last 20% of the BR belongs to the hadronically-decaying $\tau + X$ decay process. The number of b-jets in the event, shown in Figure 5.13b, can be a discriminating variable, since the number of b-jets in the signal samples peak at 2, and the $t\bar{t}$ process produces 3 or 4 b-jets in most events[4].

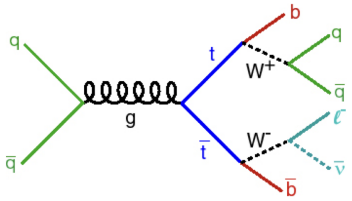


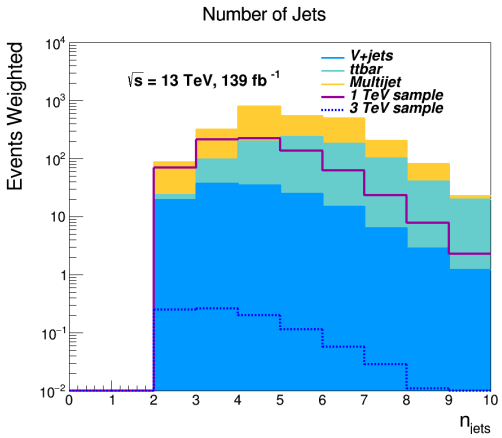
Figure 5.12: Feynman diagram showing the $t\bar{t}$ production and decay channels. The top quark can decay to a W boson that decays either hadronically (top branch) or leptonically (bottom branch).

The vector boson (V) and jets process is the third background to the signal model. Z bosons have a BR of roughly 70% to a quark-antiquark pair and roughly 10% to a lepton-antilepton pair (3% for each lepton type) [32]. The W bosons have a BR of 68% to a quark-antiquark pair, and roughly 11% to each lepton-neutrino combination. This results in possible final state topologies that are similar to the signal model.

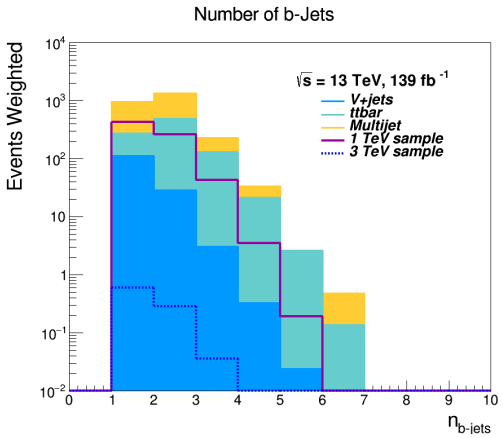
5.6 Preliminary Results

The reconstruction of the lepton jet is essential in reconstructing the Maverick top partner, and plays a key role in the analysis. A study was carried out that reconstructed the lepton jets based on different selection criteria. The optimal selection criteria was then applied, the choice of which was based on the reconstruction of the Maverick top partner, while reducing the number of events in the background processes.

[4]The cuts applied are discussed in the next section.



(a) Number of jets in the signal model and the three different backgrounds considered. The multi-jet final state is the leading background of the signal model, followed by $t\bar{t}$ production and V+jets.



(b) Number of b-tagged jets in the signal model and the three different backgrounds considered. In both the 1 TeV and 3 TeV Maverick top signal samples, the number of b-jets peaks at 2. In the multi-jet and $t\bar{t}$ samples, the number of b-jets peak at 3.

Figure 5.13: Distributions showing the number of jets and the number of b-jets for the signal and background samples.

5.6.1 Muon Studies

The selection criteria of the formation of the lepton jets plays a crucial role in the reconstruction of the lepton jet and subsequently the Maverick top partner. The studies involved varying the minimum number of muons in the lepton-jet, the isolation criteria of the selected muons, and the inclusion of the track information of the muon(s). The choice for the reconstruction of the lepton jet was ultimately made to optimise the reconstruction of the Maverick top partner, while also decreasing the yield of the background processes.

The kinematic distributions used to choose the selection of the lepton jet criteria are the lepton jet mass and p_T, and the Maverick top mass distributions. The yields of the signal samples and the background samples are given in Table 5.2. The first step in creating the lepton jets is reconstructing the muons. The muons can be reconstructed with either no isolation requirement, or with the standard isolation requirement. The lepton jets are subsequently created, requiring either at least one or at least two muons in a radius ΔR of 0.4 from each other. Lastly, the lepton jet can be created using information from the ID and the reconstructed muons: lepton jets with either one muon with two associated tracks, or two muons with two associated tracks are reconstructed.

Reconstruction criteria	1 TeV signal yield	3 TeV signal yield	Multi-jet yield	$t\bar{t}$ yield	V + jets yield
One Muon					
non-Isolated	1630.96	6.7416	115616	159108	23709.5
Isolated	1133.84	4.09895	13504	148314	23535.8
Two Tracks	973.126	1.96019	4704.76	33087.5	2732.22
Two Muons					
non-Isolated	755.177	0.941042	12443.3	3971.37	162.394
Isolated	743.699	0.922994	1655.12	767.227	142.481
Two Tracks	635.493	0.824893	859.509	471.638	158.764

Table 5.2: Table showing the yields of the signal and background processes.

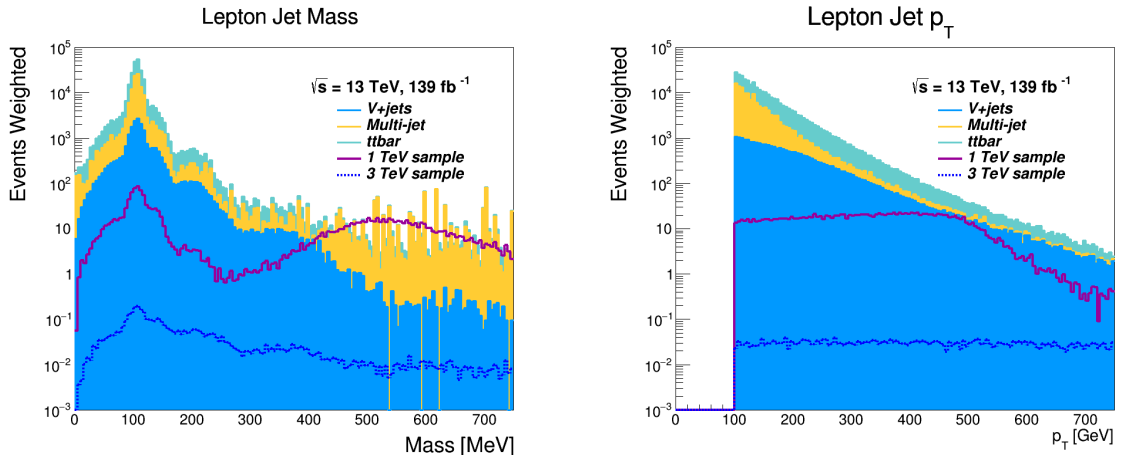
Results Requiring One Muon

The first set of distributions, shown in Figure 5.14, show the reconstruction of the lepton jet requiring at least one non-isolated muon. The next set of distributions (Figure 5.15) show the reconstruction of the lepton jet again with at least one muon, but this time with the isolation requirement. The third set of distributions (Figure 5.16) the formation of a lepton jet with at least one muon, but requiring two tracks associated to the muon. In the case of the lepton jet with two tracks but only one muon, the muon has been reconstructed with the isolation criteria applied. As the restrictions placed on the lepton jet formation are increased (from non-isolation to isolation, and then to two tracks with an isolated muon), the yields of all samples decrease. This is expected, since the muons reconstructed with the isolation criteria applied are a subset of all the muons with no isolation criteria applied. The biggest decrease in the yields for the background samples, are the multi-jet yields.

In the three distributions showing the lepton jet mass (Figures 5.14a, 5.15a, 5.16a) for a lepton jet requiring at least one muon, two peaks are observed. The first peak is around 105 MeV, the mass of a muon, and is present in the background samples as well as the signal samples. In this case, the reconstruction of the lepton jet does not include the second muon, and this is used as a metric to show the misreconstruction of the lepton jet. The second peak is around 500 MeV, the mass of the DP in the model and is only present in the 1 TeV signal sample. The 3 TeV signal sample does not have a large enough yield to see this second peak. Both peaks are present in the 1 TeV sample, since the lepton jet is constructed in the case of one muon and two muons, since the requirement is at least one muon.

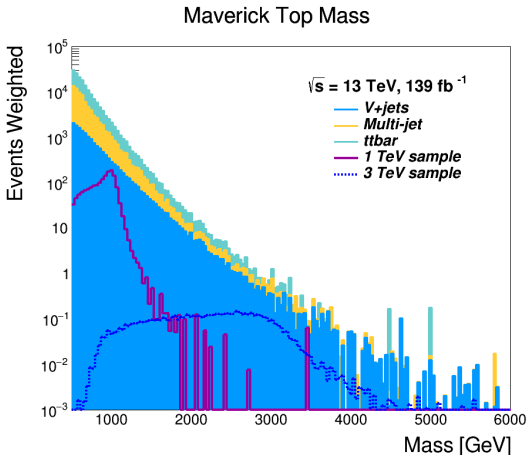
The second distributions for comparison are the lepton jet p_T distributions, shown in Figures 5.14b, 5.15b and 5.16b. While the background processes decrease exponentially for higher p_T, the signal samples roughly increase to 500 GeV before dropping off. This highlights the boosted nature of the DP in the signal samples.

The third set of distributions to compare is the Maverick top mass (Figures 5.14c, 5.15c, 5.16c), where the Maverick top partner is reconstructed by adding the four-vectors of the DP candidate and the top jet. In the background samples, there is no observed peak and the distribution is steeply falling. The 1 TeV Maverick top is well-reconstructed, with a clear peak around 1 TeV in all three distributions. In Figure 5.14c, the 1 TeV bump is not as symmetrical as in the other two figures, showing that removing the isolation criteria of the muon affects the reconstruction of the Maverick top partner. In the case of the 3 TeV signal samples, the



(a) Lepton jet mass

(b) Lepton jet p_T

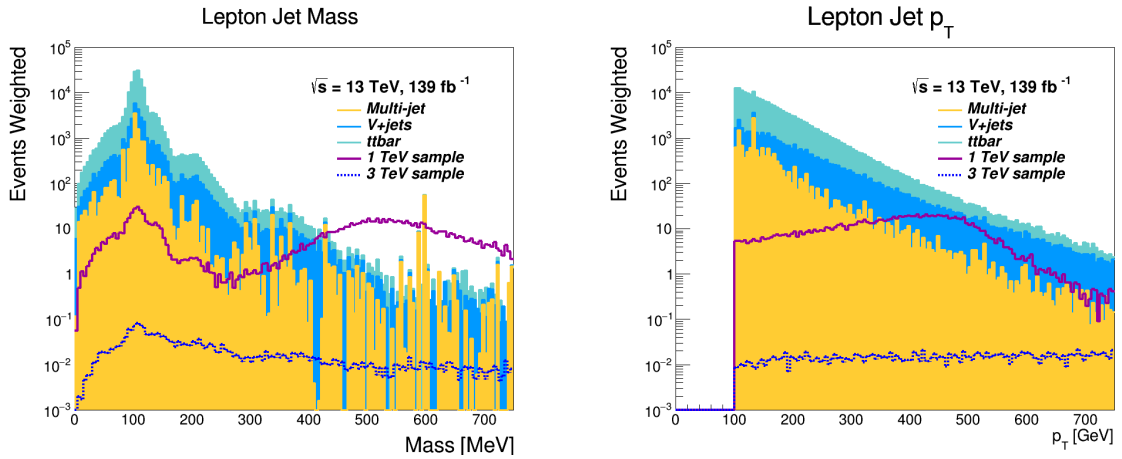


(c) Maverick top mass

Figure 5.14: Kinematic distributions showing the reconstruction of the lepton jet and the Maverick top partner when there is one non-isolated muon in the lepton jet. The background processes are the shaded areas, while the 1 TeV signal sample is shown by the purple solid line, and the 3 TeV signal sample is shown by the dashed blue line.

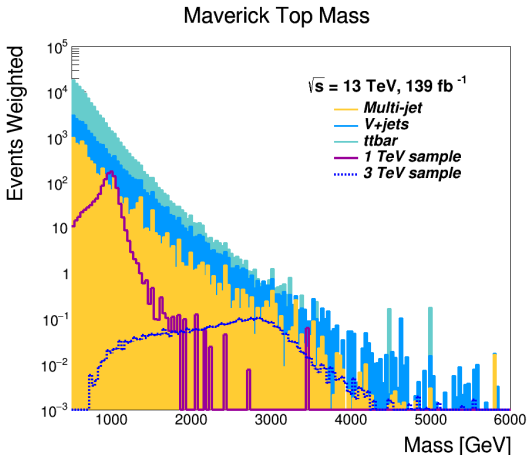
peak around 3 TeV is not as pronounced as in the 1 TeV case, and there is a significant tail to the left of the peak in all three cases.

When comparing the kinematic distributions shown in Figures 5.14, 5.15 and 5.16, with only one muon in the lepton jet, it is clear that the additional isolation requirement of the muon and the requirement of two tracks associated to the muon improves the kinematic distributions and the ultimate reconstruction of the Maverick top partner.



(a) Lepton jet mass

(b) Lepton jet p_T



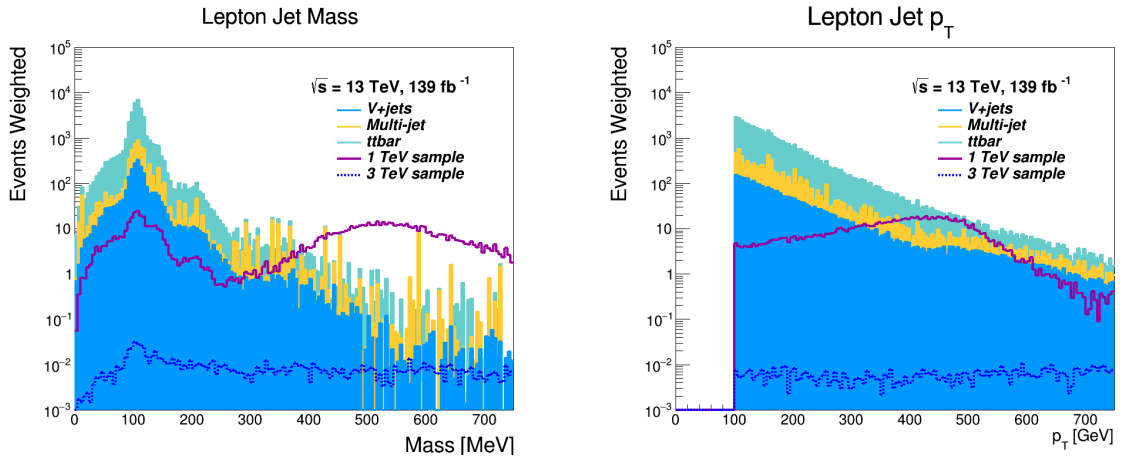
(c) Maverick top mass

Figure 5.15: Kinematic distributions showing the reconstruction of the lepton jet and the Maverick top partner when there is one isolated muon in the lepton jet. The background processes are the shaded areas, while the 1 TeV signal sample is shown by the purple solid line, and the 3 TeV signal sample is shown by the dashed blue line.

Results Requiring Two Muons

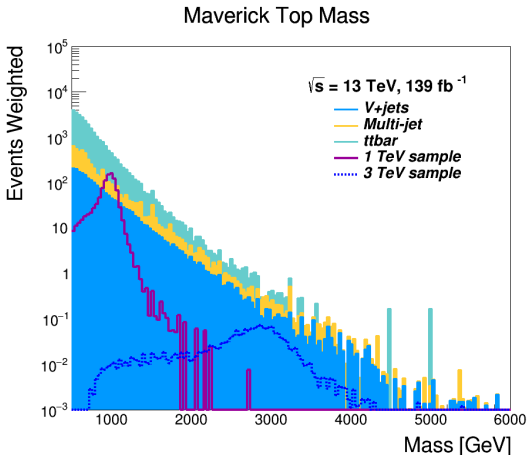
The next sets of distributions are reconstructed with at least two muons in the lepton jet. Figure 5.17 shows the lepton jet mass and p_T, and the Maverick top mass when no isolation requirements are applied to the muons. Figure 5.18 shows the same distributions, except the muons are reconstructed with the *PFlowLoose* requirement. Figure 5.19 again shows the same three kinematic distributions, however the two isolated muons in the lepton jet are required to have two tracks associated to them as well.

Comparing Figures 5.17a, 5.18a and 5.19a, the peaks of the three 1 TeV samples are all at 500 MeV, the mass of the DP. The shape of the distribution around this peak is almost identical to the shape of the peak in Figures 5.14a, 5.15a and 5.16a, showing that indeed the lepton jets requiring at least two muons are a subset of the lepton jets requiring at least one muon. The 3 TeV peak is not sufficiently clear enough due to low statistics, and there is an over-all reduction in background events as the reconstruction criteria of the muons and the lepton jets become more stringent.



(a) Lepton jet mass

(b) Lepton jet p_T

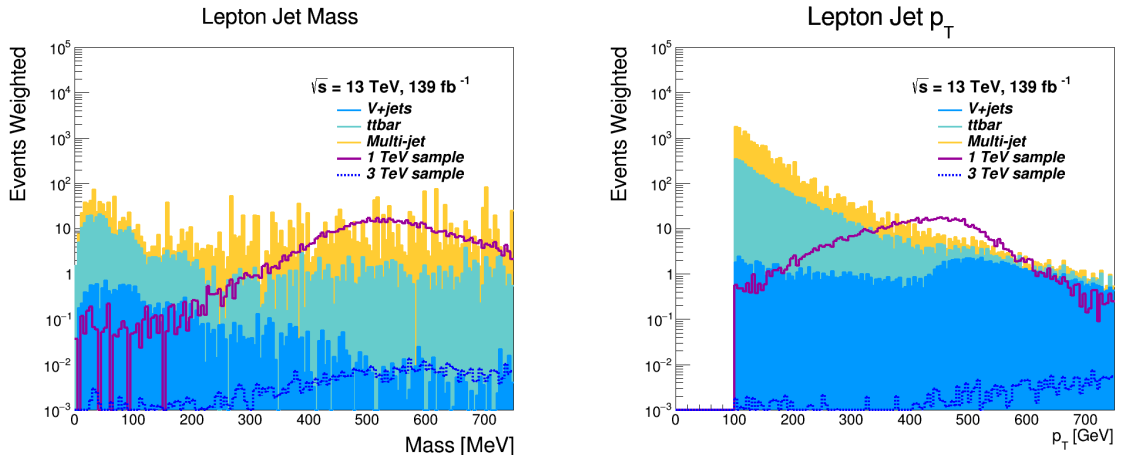


(c) Maverick top mass

Figure 5.16: Kinematic distributions showing the reconstruction of the lepton jet and the Maverick top partner when there is one isolated muon in the lepton jet that has two associated tracks. The background processes are the shaded areas, while the 1 TeV signal sample is shown by the purple solid line, and the 3 TeV signal sample is shown by the dashed blue line.

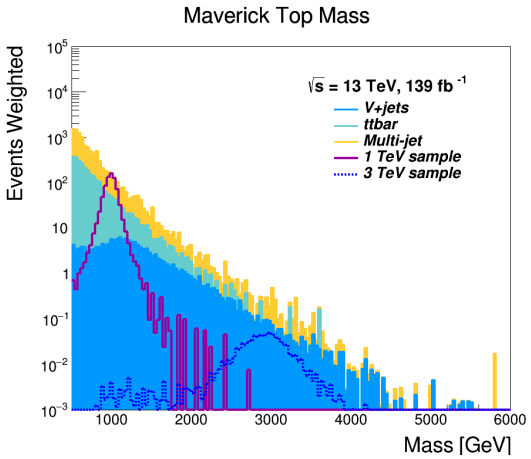
The second distributions for comparison are the lepton jet p_T distributions, shown in Figures 5.17b, 5.18b and 5.19b. The background distributions have a different shape compared to the reconstruction with one muon. The multi-jet background is still decreasing exponentially in Figure 5.17b, but it flattens out more once the isolation requirement is added in Figure 5.18b and the track requirement is added in Figure 5.19b. There is a significant decrease in the number of multi-jet events after adding the isolation requirement. The V+jets sample has a peak around 500 GeV, close to the p_T of the 1 TeV dark photon in all three distributions.

The Maverick top mass distributions (Figures 5.17c, 5.18c, 5.19c) show the improvement in Maverick top reconstruction if two muons are required in the lepton jet. The peaks in all three distributions are more pronounced in the 1 TeV case, and are more symmetrical as compared to the one-muon case, and it is possible to see a peak around 3 TeV for the 3 TeV signal sample. Adding the isolation criteria (Figure 5.18c) does not improve the reconstruction by much, but it does decrease the background significantly. Adding the track requirement in Figure 5.19c has the same effect.



(a) Lepton jet mass

(b) Lepton jet p_T

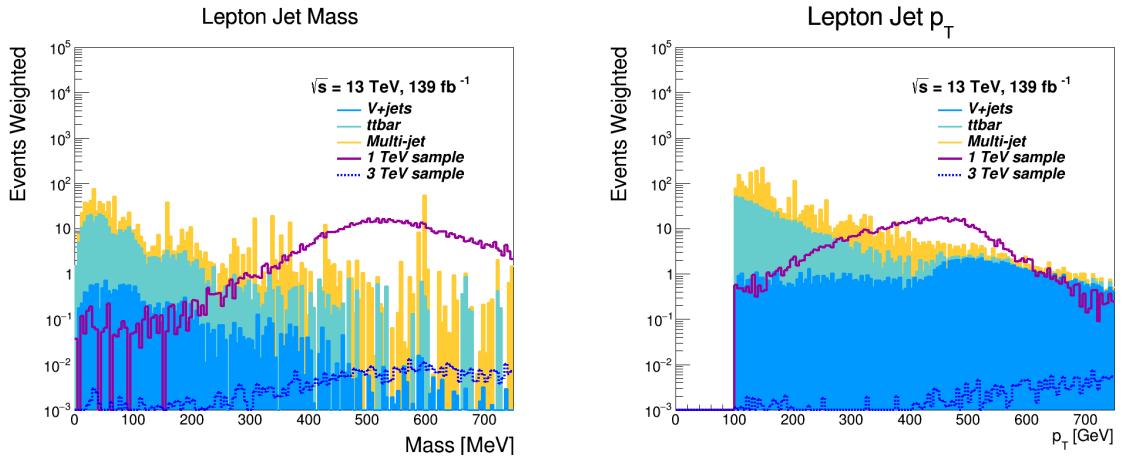


(c) Maverick top mass

Figure 5.17: Kinematic distributions showing the reconstruction of the lepton jet and the Maverick top partner when there are two non-isolated muons in the lepton jet. The background processes are the shaded areas, while the 1 TeV signal sample is shown by the purple solid line, and the 3 TeV signal sample is shown by the dashed blue line.

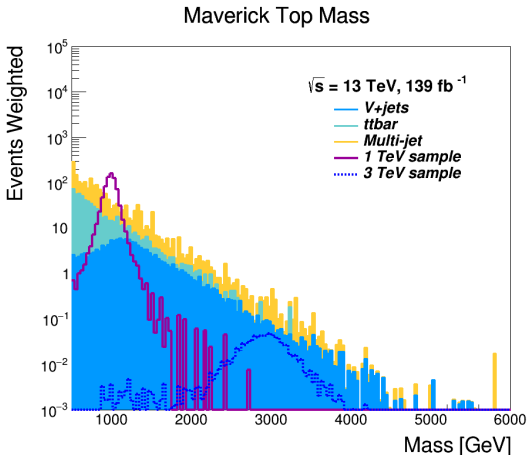
Conclusions of the Muon Studies

The comparison of the yields of each sample and the reconstruction of the kinematic distributions of the lepton jets and the Maverick top partners, led to the decision to reconstruct the lepton jet with at least two muons, with the *PFlowLoose* isolation criteria, but without requiring two associated tracks. The reconstruction of the lepton jet is notably better with the two-muon requirement, and the background reduction is sufficient without having to include the tracks.



(a) Lepton jet mass

(b) Lepton jet p_T



(c) Maverick top mass

Figure 5.18: Kinematic distributions showing the reconstruction of the lepton jet and the Maverick top partner when there are two isolated muons in the lepton jet. The background processes are the shaded areas, while the 1 TeV signal sample is shown by the purple solid line, and the 3 TeV signal sample is shown by the dashed blue line.

5.6.2 Kinematic Distributions

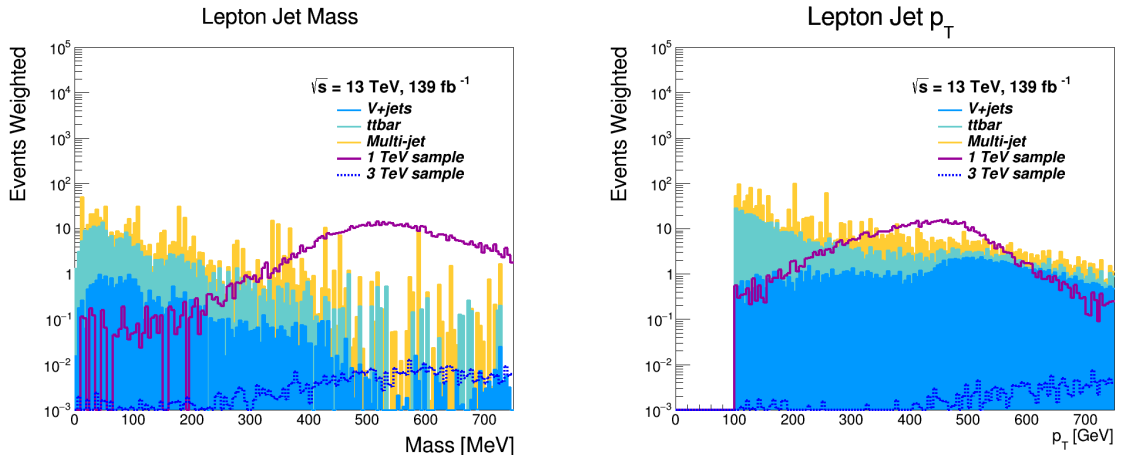
Before background estimation and signal optimisation can take place, important kinematic variables of the signal and background samples need to be studied.

The first distinguishing variable is the number of muons in each event, shown in Figure 5.20. In both the 1 TeV and 3 TeV signal samples, the number of muons in each event peaks at 2. The vector boson production along with jets background sample also has a significant peak at 2, while the $t\bar{t}$ sample peaks at 1 and the multi-jet sample has a small difference between 1 and 2 muons.

The second variable considered is the p_T-balance between the lepton jet and the top jet, defined by:

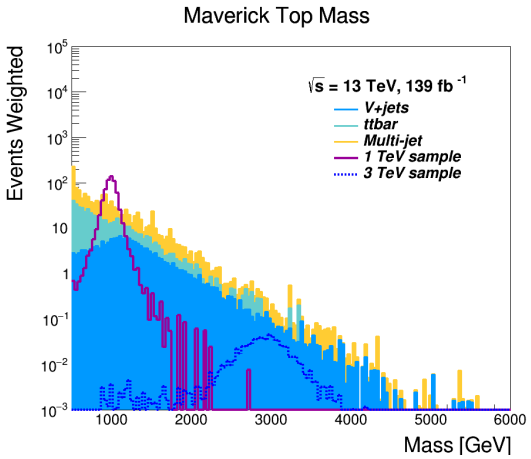
$$p_T\text{-balance} = \frac{p_T(\text{top jet})}{p_T(\text{top jet}) + p_T(\text{lepton jet})} \tag{9}$$

The signal samples, shown in Figure 5.21 are well-balanced, with a wide peak around 0.5, showing the back-to-back and boosted nature of the signal topology. The vector boson pro-



(a) Lepton jet mass

(b) Lepton jet p_T



(c) Maverick top mass

Figure 5.19: Kinematic distributions showing the reconstruction of the lepton jet and the Maverick top partner when there are two non-isolated muons in the lepton jet, with the additional requirement of two tracks associated to the muons. The background processes are the shaded areas, while the 1 TeV signal sample is shown by the purple solid line, and the 3 TeV signal sample is shown by the dashed blue line.

duction along with jets background has a similar signature, while the multi-jet and $t\bar{t}$ samples are unbalanced, with a peak shifted to the right. The p_T-balance is a useful discriminating variable in the analysis.

The third kinematic plot considered before starting with the background estimation and signal optimisation is the p_T sum of the lepton jet and the top jet, shown in Figure 5.22. The 1 TeV sample has a significant peak in comparison to the background distributions, two of which (multijet and $t\bar{t}$) are steeply falling. The vector boson production along with jets background has a peak in a similar place to the 1 TeV signal sample, and the 3 TeV sample has a broad, flat distribution with no clear peak.

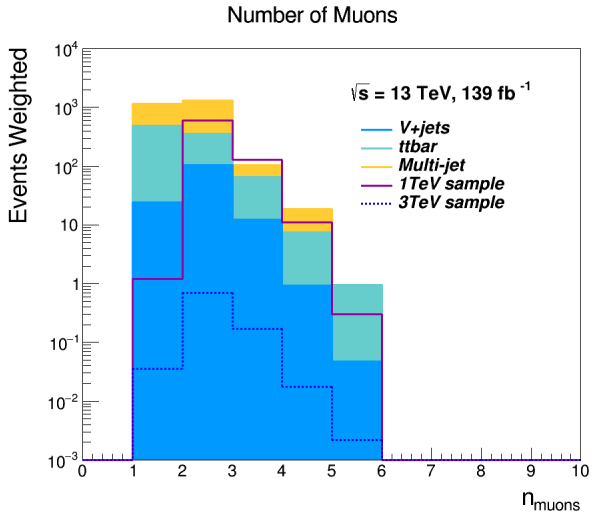


Figure 5.20: The number of muons in the signal and background samples.

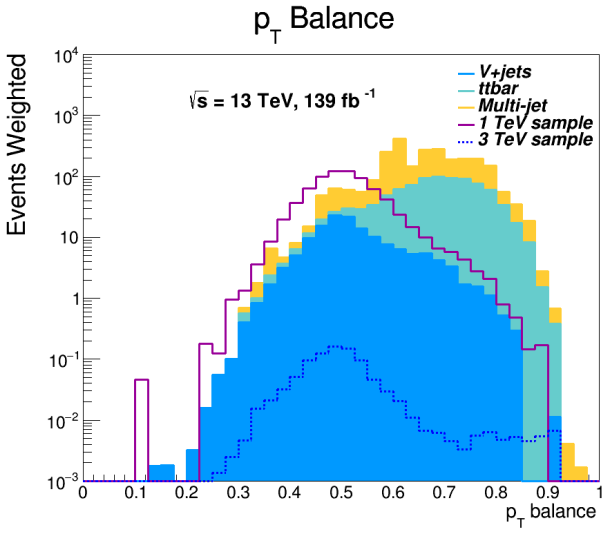


Figure 5.21: The p_T-balance of the lepton jet and the top jet, shown for the signal and background samples, as defined in Equation 9.

5.7 Conclusions

This chapter explores a model in which a top-like VLQ decays to a DP, which in turn decays into a collimated lepton pair. The search is carried out using ATLAS simulated events, and is part of an ongoing ATLAS analysis. The final-state topology includes a collider object, the lepton jet, that is not often used in analyses. Validating the tools used to reconstruct the lepton jet, and optimising the reconstruction of the lepton jet was a focus in Section 5.6.1. Using the optimal reconstruction of the lepton jet is critical in reconstructing the Maverick top partner, and also plays an important role in reducing the relevant backgrounds. Kinematic distributions that are relevant to the selection of the signal and control regions were discussed in Section 5.6.2, and will be used in the selection of these regions in the analysis, which is ongoing.

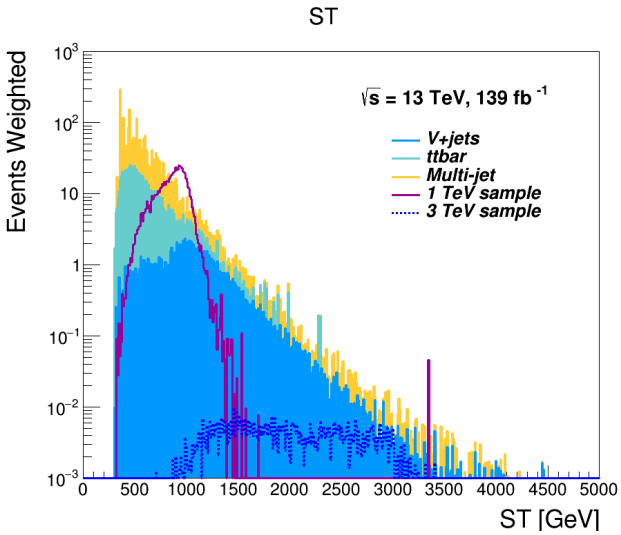


Figure 5.22: p_T sum of the top lepton jets, shown for the signal and background samples.

6 Placing Constraints on a t-Channel Dark Matter Model

The search for Dark Matter (DM) in colliders involving traditional missing energy signatures has come up empty-handed. No particle candidate for DM has been found, but limits and constraints have been placed on parameter spaces through the searches that have been performed.

There are two broad approaches in the search for DM candidates, aside from dedicated searches at particle colliders. The first is theory-driven: a model-specific approach is undertaken where DM is embedded in a framework that has been built up from first principles. The second approach is phenomenological: simplified models are used to interpret experimental results, and important features of a diverse range of extensions to the SM can be studied. The models in the phenomenolgy approach are less dependent on the underlying high-energy theory of the model, and can be used to explore viable DM scenarios without having the rigour of purely theoretical approaches. In these simplified approaches, a DM particle is generally assumed to interact minimally with the SM, through a limited number of couplings and additional new physics states [151, 152].

In the most simplified DM models, a single massive DM particle interacts with the SM through a single new mediator particle. In this case, the dark sector is composed solely of the massive DM particle and the mediator. The DM particle is required to be stable, and this is enforced by applying some discrete or continuous symmetry that acts differently on the DM state and the SM states. The interactions between the mediator and the DM and SM states are determined by the mediator's quantum numbers, and its representation under the new symmetry and the SM gauge group. In the case of t-channel models, the mediator and the DM state's properties are similar relative to the new symmetry. If under a discrete Z_2 symmetry the mediator is Z_2-odd, it can couple to one DM and one SM particle and in the simplest case, the t-channel mediators should decay into DM and SM states on timescales shorter than cosmological ones. If the mediators decay on longer timescales, they would be stable and carry colour or electric charge, which would violate observational constraints.

This section explores a t-channel DM model, as explored by the LHC Dark Matter Working Group in Reference [153], in a simplified paradigm, first by explaining the theoretical framework of the model, and then using MadAnalysis5 and CONTUR introduced in Section 3.3.3 to place limits on certain parameters and exclude regions of the parameter space. The process is run using events generated at leading-order (LO) and at next-to-leading order (NLO). The LO calculations and event generation is less computationally expensive, but the NLO calculations

have a higher accuracy. A comparison between the exclusions[1] at LO and at NLO is made, as well as a comparison between the exclusions from the different frameworks.

6.1 Theoretical Framework

This section explains the theory model used in the determining the constraints, starting from the most minimal form of the theory and building on it using additional assumptions and restrictions. The model starts with extending the SM with one DM particle that is Z_2-odd, and one mediator that is also Z_2-odd. Various spin configurations and interactions with the SM are possible, and are discussed in Reference [153], but the focus in this chapter will be on the setup that was used here. The model is then extended to include multiple mediators, but still a single DM particle, and still relies on t-channel exchanges for DM annihilation. The extension is built on ideas of compositeness, described in References [154–156].

6.1.1 Minimal Setup

In the most minimal setup of the model, the SM is extended to include one DM candidate X and one mediator state Y. The DM candidate is proposed to be a stable colourless electroweak singlet, and the stability is enforced by imposing a Z_2 symmetry under which all SM fields are even, and the mediator and DM particles are odd. The DMSimpt[2] framework used was introduced in Reference [157], contains multiple classes of spin configurations for the DM particle, and the mediator can be either fermionic or a scalar field. This allows the exploration of different spins of the DM particle and the mediator, the flavour structure of interactions and the quantum numbers of the mediator particle that depend on the coupling between the SM sector and the DM particle. The framework can be used to make collider simulations that include NLO QCD corrections to new physics processes that involve the DM particle and the mediator.

The full Lagrangian for the models considered can be split up into three components:

$$\mathcal{L} = \mathcal{L}_{SM} + \mathcal{L}_{kin} + \mathcal{L}_{XY} \tag{1}$$

$\mathcal{L}_{SM}$ is the SM Lagrangian, as introduced in Section 2.2.2, while $\mathcal{L}_{kin}$ represents the gauge-invariant kinetic and mass terms for all new fields, and $\mathcal{L}_{XY}$ introduces the interactions between the DM particle and the mediator with the SM. $\mathcal{L}_{XY}$ introduces a number of free coupling parameters, and can be extended according to the spin configurations of the DM particle. This work explores a real scalar DM particle, with colour-triplet fermionic mediators, and is tagged as the F3S configuration.[3] The Lagrangian for this configuration can be written as:

$$\mathcal{L}_{XY} = \sum_{f=u,d} \lambda_f \bar{\Psi}_f f_R \tilde{S} + \lambda_Q \bar{\Psi}_Q Q_L \tilde{S} + \text{H.c.} \tag{2}$$

Q_L represents the weak doublet of left-handed SM quarks, while u_R and d_R represent the corresponding singlets. Ψ_Q, Ψ_u and Ψ_d represent the fermionic mediators and interact with the Q_L, u_R and d_R fields respectively. $\tilde{S}$ represents the real scalar DM state, and one fermionic

[1] The term "exclusion" refers to the XX% CL limit, with XX either being 95 or 68.

[2] The DMSimpt name comes from the fact that the model is a simplified t-channel DM model.

[3] A description of the other possible states can be found in Reference [153].

mediator is introduced for each generation of SM fermions. The mediators lie in the same representation as their SM fermionic partners, and they are vector-like. The mediators also possess a flavour index, and while they have been left out of Equation 2 for clarity, the coupling constants λ_u, λ_d and λ_Q are 3×3 matrices in the flavour space. The matrices are real and flavour-diagonal to prevent loop-induced mixing between the SM fermions. Each mediator is hence associated with a given generation of SM partners.

6.1.2 Extending using Ideas of Compositeness

Composite scenarios of new physics can be used to influence the development of t-channel models. Additional coloured and non-coloured resonances are postulated in many of these models, and arise as bound states due to an underlying fermionic construction that features new strong dynamics. Many of the resonances can be tied to the top quark and partial compositeness [158], trying to explain the large mass of the top quark in relation to the other SM quarks, but the resonances can also be electrically neutral, colourless and stable and therefore be candidates for DM particles [154–156]. The stability of the DM particle is enforced by a residual discrete Z_2 symmetry that arises from the breaking of the new strong dynamics. All SM fields have an even parity under this symmetry, while the DM state has an odd parity. The particle spectrum then contains both odd and even new states.

Next-to-Minimal Setup

As a slight extension of the most simple model introduced above, one real scalar DM state can be included with two fermionic top partners or mediators. One Z_2-even state, labelled Y_t' and one Z_2-odd state labelled Y_t are introduced, and have the same quantum numbers as the right-handed SM top quark field t_R. The effective Lagrangian for the interactions between the real scalar DM state X can be written in a similar way to the notation introduced in Equation 2:

$$\mathcal{L}_{XY} = \lambda_t \bar{Y}_t t_R X + \lambda_t' \bar{Y}_t Y_t' X + \text{H.c.} \tag{3}$$

λ_t and λ_t' represent two new physics coupling constants, and the DM mass M_X and mediator masses M_Y and $M_{Y'}$ are added to the list of new parameters.

Less Minimal Setup

The final model used in this study is less minimal than the one described above, and is closer to UV completeness.[4] In this case, there are a sufficient number of mediator fields that generate the top quark mass through partial compositeness. Weak singlet and doublet mediators are required in this scenario [159], and are assumed to be Z_2-odd for simplicity. The effective Lagrangian for this scenario is given by:

$$\mathcal{L}_{XY} = \lambda_t \bar{Y}_t t_R X + \lambda_Q \bar{Y}_Q Q_L X + \text{H.c. with } Y_Q = \begin{pmatrix} Y_{Q,t} \\ Y_{Q,b} \end{pmatrix} \text{ and } Q_L = \begin{pmatrix} t_L \\ b_L \end{pmatrix} \tag{4}$$

A number of free parameters are introduced in this model: the two new physics couplings λ_Q and λ_t, the DM mass M_X and three mediator masses M_{Y_t}, $M_{Y_{Q,t}}$ and $M_{Y_{Q,b}}$. The masses are taken to be free parameters, but are calculable in effective setups that incorporate partial compositeness.

[4] Ultraviolet or UV completeness means that quantum field theories that are viable at lower energies are also well-defined and viable at arbitrarily high energies.

In the DMSimpt framework introduced in Reference [157], this model can be selected using the F3S-VLQ classification, again stressing the use of a scalar DM particle and fermionic mediators.

6.1.3 Final Simplification and Model Setup

Moving away from the notation used in Reference [153], the $SU(2)_L$ doublet and singlet states can be written as:

$$Q_{L,R} = \begin{pmatrix} T_{L,R} \\ B_{L,R} \end{pmatrix} \text{ and } \tilde{T}_{L,R} \tag{5}$$

In the simplified model considered, the masses of the three mediators $T_{L,R}$, $\tilde{T}_{L,R}$, $B_{L,R}$, the mass of the dark matter particle X, and the couplings λ_Q and λ_T are free parameters that can be set. The Lagrangian for the BSM contributions can be written as follows, to show the six free parameters:

$$\mathcal{L}_{BSM} = \mathcal{L}_{kin} - M_T \bar{T} T - M_B \bar{B} B - M_{\tilde{T}} \bar{\tilde{T}} \tilde{T} - \frac{1}{2} M_X X^2 + \Big(\lambda_Q [\bar{T}_R t_L + \bar{B}_R b_L] X + \lambda_T \bar{\tilde{T}}_L X + H.c. \Big) \tag{6}$$

This is further simplified by setting the masses of the three VLQs equal, and denoting them by Y, and setting the BSM couplings equal as well. This leaves us with three parameters: the VLQ mass M_Y, the DM candidate mass M_X, and the BSM coupling λ.

6.2 Process Generalities and Event Generation

The simplified model and the processes that produced the DM particle and the mediator can be split into three different process types. This section explains these different processes and the implications they have in the event-generation of the samples used in the reinterpretation study.

6.2.1 The Three Contributing Processes

To fully understand and study the signal kinematics of the model, the production of DM particles and mediators need to be split up into three main subprocesses, and their contributions to the overall cross-section should be identified individually. At tree-level, the DM particle can couple to SM quarks and so diagrams that lead to the production of any pair of new physics states need to be included.

The production of a pair of DM or mediator states can be split up as follows:

- Production of a pair of DM states: $pp \to XX$
- Associated production of a DM particle and a mediator: $pp \to XY + X\bar{Y}$
- Production of a pair of mediator particles: $pp \to YY + Y\bar{Y} + \bar{Y}\bar{Y}$

The first two processes are labelled XX and XY, respectively. The production of a pair of mediator particles can be split up further. In the case of a real DM state, as is considered here, the production of two mediators or two anti-mediators can only take place in t-channel DM exchanges, and the processes are labelled YY and $\bar{Y}\bar{Y}$. The production of a mediator and an anti-mediator pair can be split up into three contributing components, and representative Feynman diagrams for the processes can be seen in Figure 6.1:

- QCD diagrams, or the s-channel production of the pair, labelled $Y\bar{Y}_{QCD}$
- t-channel exchange diagrams, labelled $Y\bar{Y}_t$
- the interference between these two production modes, labelled $Y\bar{Y}_i$

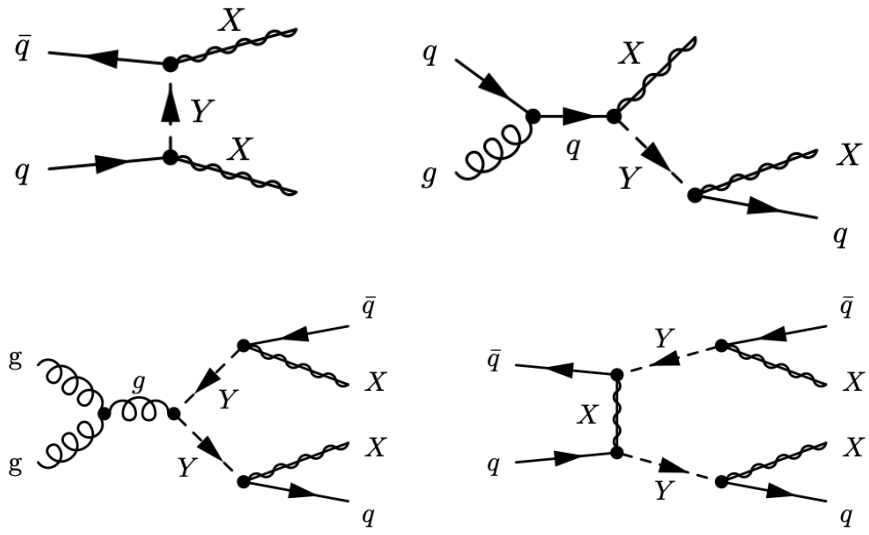


Figure 6.1: Feynman diagrams representing the different production processes. The first diagram (top left) shows the production of a pair of DM particles, while the second (top right) shows the associated production of a DM particle and a mediator, followed by the decay of the mediator into a DM particle and a quark. The third diagram (bottom left) shows the s-channel or purely QCD production of the pair of mediators, again with their decay, and the last diagram (bottom right) shows the t-channel DM exchange.

6.2.2 Dependency on the BSM Coupling

The squared of the matrix element of each of the processes has a different dependency on the BSM coupling λ and α_s, and this dependency is shown in Table 6.1.

Process	Label	ME^2 proportional to
Pair of DM states	XX	λ^4
DM state and (anti) mediator	XY	$\lambda^2\alpha_s$
Pair of (anti) mediators	YY_t	λ^4
	$\bar{Y}\bar{Y}_t$	λ^4
Mediator and anti-mediator	$Y\bar{Y}_{QCD}$	α_s^2
	$Y\bar{Y}_t$	λ^4
	$Y\bar{Y}_i$	$\lambda^2\alpha_s$

Table 6.1: Table showing the proportionality of the matrix element squared (ME^2) to the BSM coupling λ and α_s.

The importance of separating out the subprocesses can clearly be seen when looking at the total cross-section of the BSM process, and having factorised λ and writing the process cross-

sections as a function of the masses M_X and M_Y:

$$\begin{aligned}\sigma_{BSM} = &\lambda^4\sigma_{XX}(M_X, M_Y) + \lambda^2\sigma_{XY}(M_X, M_Y) + \lambda^4\sigma_{YY_t}(M_X, M_Y) \\ &+ \lambda^4\sigma_{\bar{Y}\bar{Y}_t}(M_X, M_Y) + \sigma_{Y\bar{Y}_{QCD}}(M_X, M_Y) + \lambda^4\sigma_{Y\bar{Y}_t}(M_X, M_Y) \\ &+ \lambda^2\sigma_{Y\bar{Y}_i}(M_X, M_Y)\end{aligned} \tag{7}$$

The cross-section of the BSM process can be written with the efficiency ε, which is also mass-dependent, factored out of the cross-section of each process. The cross-section as a function of the efficiency can therefore be written as:

$$\begin{aligned}\hat{\sigma}_{BSM} = &\lambda^4\hat{\sigma}_{XX}(M_X, M_Y)\varepsilon_{XX}(M_X, M_Y) + \lambda^2\hat{\sigma}_{XY}(M_X, M_Y)\varepsilon_{XY}(M_X, M_Y) \\ &+ \lambda^4\hat{\sigma}_{YY_t}(M_X, M_Y)\varepsilon_{YY_t}(M_X, M_Y) + \lambda^4\hat{\sigma}_{\bar{Y}\bar{Y}_t}(M_X, M_Y)\varepsilon\bar{Y}\bar{Y}_t(M_X, M_Y) \\ &+ \hat{\sigma}_{Y\bar{Y}_{QCD}}(M_X, M_Y)\varepsilon_{Y\bar{Y}_{QCD}}(M_X, M_Y) + \lambda^4\hat{\sigma}_{Y\bar{Y}_t}(M_X, M_Y)\varepsilon Y\bar{Y}_t(M_X, M_Y) \\ &+ \lambda^2\hat{\sigma}_{Y\bar{Y}_i}(M_X, M_Y)\varepsilon_{Y\bar{Y}_i}(M_X, M_Y)\end{aligned} \tag{8}$$

The equation shows that the kinematics from each component of the signal depend only on the masses M_X and M_Y, and each contribution can be rescaled by varying λ. Each process has a specific dependency on λ, as emphasised in Table 6.1, but all of the processes need to be included in the signal simulations:

- The XX process has a dependency of λ^4, but is modelled to have an additional visible object in the final state, like a jet.
- Processes with two mediators or anti-mediators in the final state (YY, $Y\bar{Y}$, $\bar{Y}\bar{Y}$) have different dependencies on λ, and are phase-space disfavoured because of large mediator masses and pair production of the mediators.
- The $Y\bar{Y}_{QCD}$ process has no dependency on λ, and serves as a baseline component independent of the DM mass.
- The other processes producing two (anti) mediators become more important as λ increases, and can benefit from parton density enhancements.
- The XY process has a weaker dependence on λ, only to the second power, but the production of a lighter DM state means that it is phase-space favoured.

6.2.3 Event Generation

The parameter space scan was performed by varying the mass of the DM particle X and the mass of the mediator M_Y, while keeping the BSM coupling λ equal to 1. The initial M_X values were varied from 50 GeV to 500 GeV, in steps of 50 GeV, while the M_Y values were varied from 500 GeV to 2000 GeV, in steps of 150 GeV, to set up a 10 x 10 grid of parameter values. This was performed at LO. A second run expanded the parameter space to a 15 x 10 grid, with the same values for M_Y but an M_X range from 50 GeV to 750 GeV. The second run was performed at LO and at NLO.

The matrix-element generator used is MadGraph5, version 2.9.20, using the MadSTR plugin [160]. MadSTR handles the resonant contributions that appear at NLO, when an intermediate mediator is produced on-shell and then decays into a DM state and a SM quark. Using MadSTR ensures that contributions are not double-counted across the three processes. For

example, at NLO, the associated production $pp \to XY \to X(Xj)$ includes configurations where the mediator is on-shell, and it should be included in XY simulations. However, off-shell contributions, which are included in the real-emission corrections to XX production, could be double counted. Using MadSTR resolves this error.

Matrix elements are generated for LO and NLO accuracy for the processes, using the UFO model introduced in Reference [157], and using the model selection F3S-VLQ. The respective matrix elements are convolved with the LO and NLO sets of NNPDF4.0 parton densities. MadSpin [161] and MadWidth [162] are used to retain off-shell propagation and spin correlation effects for the decays of heavy unstable particles. Pythia8 (version 8.306) is used for the parton showering and hadronisation, and is matched with fixed-order calculations in the MC@NLO fashion [163].

Full details of the event generation process and commands can be found in Reference [153], but it is important to place emphasis on running the processes individually. In the case of the LO event generation, all seven subprocesses were run. However the NLO generation of the $Y\bar{Y}_i$ process is not possible, and so the cross-sections of the parameter points were calculated by rescaling the LO parameter point cross-sections for the process, using the k-factor defined as:

$$k_{Y\bar{Y}_i} = \sqrt{K_{Y\bar{Y}_t} K_{Y\bar{Y}_{QCD}}} = \sqrt{\frac{\hat{\sigma}^{NLO}_{Y\bar{Y}_t}}{\hat{\sigma}^{LO}_{Y\bar{Y}_t}} \frac{\hat{\sigma}^{NLO}_{Y\bar{Y}_{QCD}}}{\hat{\sigma}^{LO}_{Y\bar{Y}_{QCD}}}} \tag{9}$$

The k-factor is the geometric mean of the k-factors of the $Y\bar{Y}_{QCD}$ and $Y\bar{Y}_t$ k-factors, and is calculated using the cross-sections $\hat{\sigma}^{LO}$ and $\hat{\sigma}^{NLO}$ evaluated at LO and NLO accuracy in QCD.

The subprocesses (seven at LO and six at NLO) are run independently, and the resulting output files are run through RIVET and CONTUR to find the exclusions in the parameter space. For the NLO $Y\bar{Y}_i$ process, the RIVET output file is rescaled using the calculated $K_{Y\bar{Y}_i}$ value for each parameter point.

6.3 Results

The results for the scans are split into two sections: the first section contains the exclusion plots for the reduced parameter space-run, which was only run at LO, and the second is for the extended parameter space run, which was run at LO and at NLO. Both sections compare the exclusions obtained from CONTUR with the exclusions obtained from MadAnalysis5. The BSM coupling λ is set to 1 in all runs.

6.3.1 Reduced Parameter Space

The reduced parameter space run was used to get an idea of the features of the parameter space. Two plots are produced that show the behaviour of the exclusions. The cross-sections used for the exclusions are the cross-sections of the individual processes added together. The reduced parameter space run was used as a proof-of-principle test, and is less detailed than the extended runs discussed in the following section.

Figure 6.2 shows the exclusions after running through the CONTUR framework. The leading analysis pool contributing to the exclusion is the missing transverse momentum and jet pool,

with the analysis contributing the most to the exclusion being the ATLAS differential cross-section measurement in events with jets and missing transverse momentum. The other analysis pools contributing to the exclusion are the $l^+l^-\gamma$, hadronic $t\bar{t}$ and l with missing transverse momentum and a jet analysis pools. The top left corner in the graph is not kinematically viable, and is unconstrained. The lower left part of the graph, for low mediator masses and low DM masses is excluded, and because the shape of the exclusion contours could not be seen above $M_X = 500$ GeV, the parameter space was extended in the next iteration of the project. Mediator masses up to roughly 1.5 TeV can be excluded for low M_X values at LO.

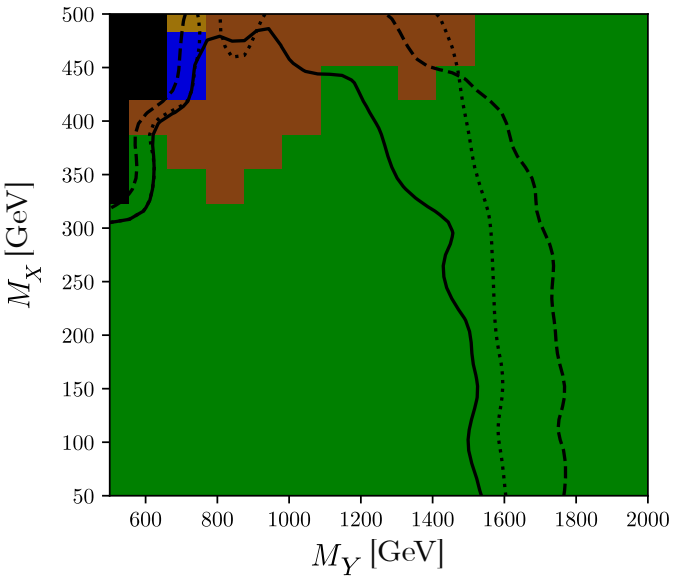


Figure 6.2: CONTUR plot showing the exclusions in the reduced parameter space. The solid black line shows the 95% observed exclusion, and the 68% observed exclusion is shown by the dashed line, while the expected exclusion is shown by the dotted line show. The plot also shows the leading analysis pools and specific analyses that contribute to the exclusion for each parameter point. The majority of the parameter space is excluded by the missing energy and jets analysis pool, shown in green, with the leading analysis being the ATLAS measurement of the differential cross-section of events with MET and a jet [164]. The exclusion in the light brown region in the top left is driven by the $l^+l^-\gamma$ analysis pool, and exclusion in the blue region just below is driven by the lepton with missing transverse momentum and a jet analysis pool. The remaining brown region represents the hadronic $t\bar{t}$ analysis pool. The black region denotes the unconstrained region.

The exclusions obtained from CONTUR can be compared to those from the MadAnalysis5 framework, as shown in Figure 6.3. The analyses used in CONTUR are mostly measurement based, while MadAnalysis5 uses searches to calculate the exclusions. This means that the frameworks use different analyses to calculate the exclusions. The exclusion from CONTUR, shown by the dashed line, is less sensitive than the exclusion obtained from MadAnalysis5, shown by the solid line. Both of the lines give the exclusion at 95% CL, and the correct DM relic abundance (indicated by Ωh^2) is superimposed on the graph. MadAnalysis5 excludes mediator masses up to roughly 1.7 TeV for values of M_X less than 400 GeV.

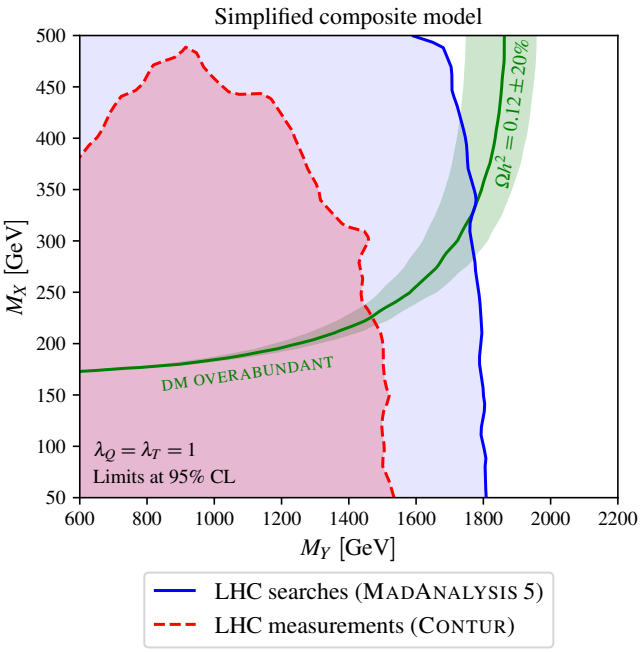


Figure 6.3: Exclusion contours showing the exclusion obtained by CONTUR (red, dashed line) and MadAnalysis5 (blue, solid line), along with the correct DM relic abundance shown in green.

6.3.2 Extended Parameter Space

After running the LO processes in the original parameter space, the maximum value of the M_X mass was extended from 500 GeV to 750 GeV, to form a 15 x 10 grid over which the scan took place. The scans were performed at LO and at NLO, using the CONTUR framework and the MadAnalysis5 framework for both orders.

The cross-section of each process at each parameter point determined the exclusion. The process with the highest production cross-section, $Y\bar{Y}_{QCD}$, drove the exclusion in all combinations of order and frameworks. Table 6.2 shows the cross-sections for a point $M_X =$ GeV, $M_Y =$ GeV for all different processes, at LO and at NLO. The total cross-section of the production of the mediators is shown in the last column, and the effect of the interference on the production of the mediator and the anti-mediator can be seen as well.

Contributions from $Y\bar{Y}_{QCD}$

The CONTUR exclusion plots for the $Y\bar{Y}_{QCD}$ process at LO and at NLO are shown in Figure 6.4. The parameter space is excluded for parameter points with low M_X and M_Y values, and the upper left points in the parameter space are not kinematically accessible. The contribution of the NLO simulations is clear: the exclusion in the parameter space is more in the NLO case than in the LO case. The exclusion curves flatten and spread out in the NLO case, excluding up to 1.4 TeV mediator masses for low DM masses. The prominent bump around $M_Y = 800$ GeV and $M_X = 400$ GeV in the LO case is shifted further to the right and higher in the NLO case.

The exclusions are mainly driven by two analysis pools: the ATLAS missing transverse momentum and jet final state, specifically the measurement made in Reference [164], and the

Process	XX	XY	YY_t	$\bar{Y}\bar{Y}_t$	$Y\bar{Y}_t$	$Y\bar{Y}_{QCD}$	$Y\bar{Y}_i$
LO	4.90e-06	6.62e-04	2.36e-06	2.36e-06	4.49e-06	2.43e-02	-5.04e-06
NLO	5.86e-05	1.21e-03	4.04e-06	4.04e-06	8.01e-06	3.27e-02	-7.74e-06
LO	4.66e-07	4.73e-05	1.72e-07	1.72e-07	3.28e-07	2.78e-01	-3.97e-07
NLO	5.45e-07	9.59e-05	3.21e-07	3.21e-07	6.35e-07	3.88e-01	-1.99e-06

Table 6.2: Table showing the cross-section for the different processes for two points. The first point is at $M_X = 50$ GeV, $M_Y = 1166.67$ GeV and the cross-sections are shown in the first two lines of the table, while the second point is at $M_X = 500$ GeV, $M_Y = 1333.33$ GeV and the cross-sections are shown in the last two lines, for the LO and NLO processes. The leading contribution is the $Y\bar{Y}_{QCD}$ process, and for point 1, the exclusion is 99.5% at LO and 99.9% at NLO, and for point 2 the exclusion is 43.4% at LO and 54.2% at NLO. All cross sections are given in units of femtobarn (pb).

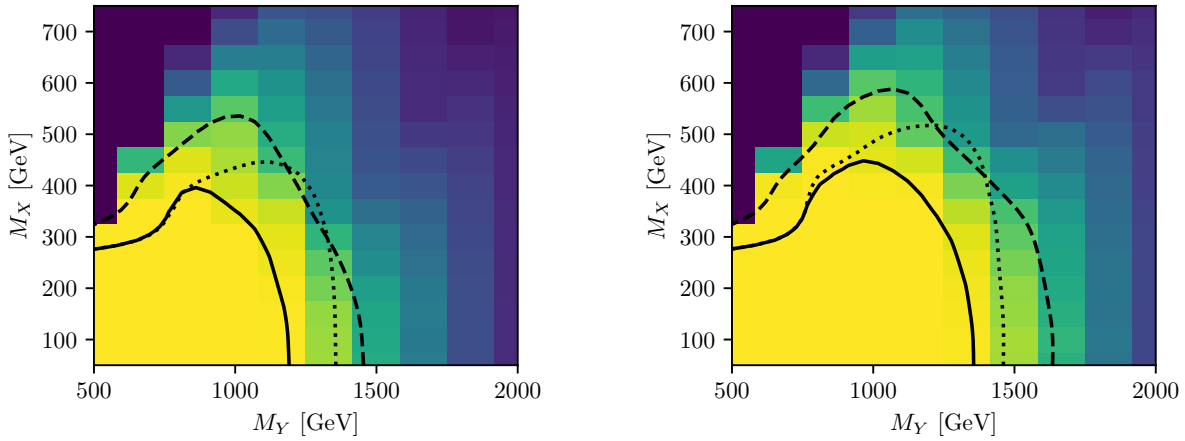


Figure 6.4: CONTUR exclusion plots for the $Y\bar{Y}_{QCD}$ process at LO (left) and at NLO (right). The yellow regions (bottom left) of the plots are excluded, while the darker blue points are not excluded. The solid line shows the 95% observed exclusion, the dashed line shows the 68% exclusion and the dotted line shows the expected exclusion. The upper left part of the parameter space is not kinematically accessible.

ATLAS measurement of the hadronic $t\bar{t}$ final state, in References [165–167]. The CMS measurements made in the lepton with missing transverse momentum and a jet final state in References [168, 169] are the leading contributors to the analysis pools for some of the points. The leading analysis pools for each parameter point can be seen in Figure 6.5, and the difference between the leading analysis pools in the LO and NLO cases are slight.

In both the LO and the NLO case, there is a region where the observed 68% exclusion (dashed line) is less than the expected exclusion (dotted line). In the LO case, this point is around $M_Y = 1250$ GeV, $M_X = 400$ GeV, and in the NLO this is around $M_Y = 1300$ GeV, $M_X = 500$ GeV. The plots shown in Figure 6.6, made in the NLO case for the point $M_Y = 1333.33$ GeV and $M_X = 500$ GeV, show why the expected exclusion is better than the observed exclusion. The RIVET plots compare the data from the relevant analysis (ATLAS missing transverse momentum and a jet) with the generated samples. The plot on the right has a discrepancy in the region around 1100 GeV, which stems from a small excess in the unfolded missing p_T spectrum. As a result, any signal that favours this kinematic regime slightly improves the data/prediction agreement, and leads to a marginally weaker exclusion limit.

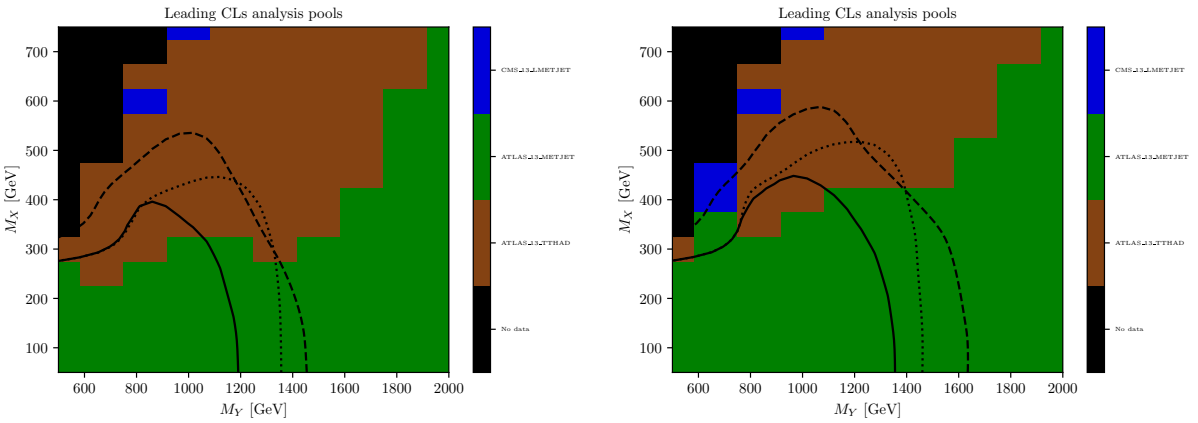


Figure 6.5: CONTUR exclusion plots for the $Y\bar{Y}_{QCD}$ process at LO (left) and at NLO (right), showing the leading analysis pools contributing to the exclusions. The solid line shows the 95% observed exclusion, the dashed line shows the 68% observed exclusion and the dotted line shows the expected exclusion. The upper left part of the parameter space is not kinematically accessible. The three leading analysis pools contributing to the exclusions are the ATLAS missing transverse momentum and jet (green), ATLAS hadronic $t\bar{t}$ (brown) and CMS lepton with missing transverse momentum and a jet (blue) pools.

The exclusions obtained from MadAnalysis5 are shown in Figure 6.7. Similar to the trend shown in the CONTUR plots (Figure 6.4), the exclusion is extended in the NLO case. The region for the low M_X and M_Y masses is excluded, and the leading analysis contributing to the exclusion is the ATLAS search for squarks and gluinos[5] [170] in final states with jets and missing transverse momentum. This is the same final state that is one of the leading contributions to the CONTUR exclusion, in the same parameter space, and reinforces the validity of the exclusion using the search-based (MadAnalysis5) and the measurement-based (CONTUR) approaches. The right side of both of the plots are excluded, up to roughly 70%. This exclusion is not seen in the CONTUR plots, and the leading analysis contributing to the exclusion in this high-M_Y region is a CMS search for new particles in events with energetic jets and missing transverse momentum [171]. This explains the exclusion in the high-M_Y region: the energetic jets would be produced by the decay products of the mediator, and the decay products high-mass mediators would be boosted, resulting in high-p_T (or energetic) decay products.

[5]Squarks and gluinos are hypothesised supersymmetric particles.

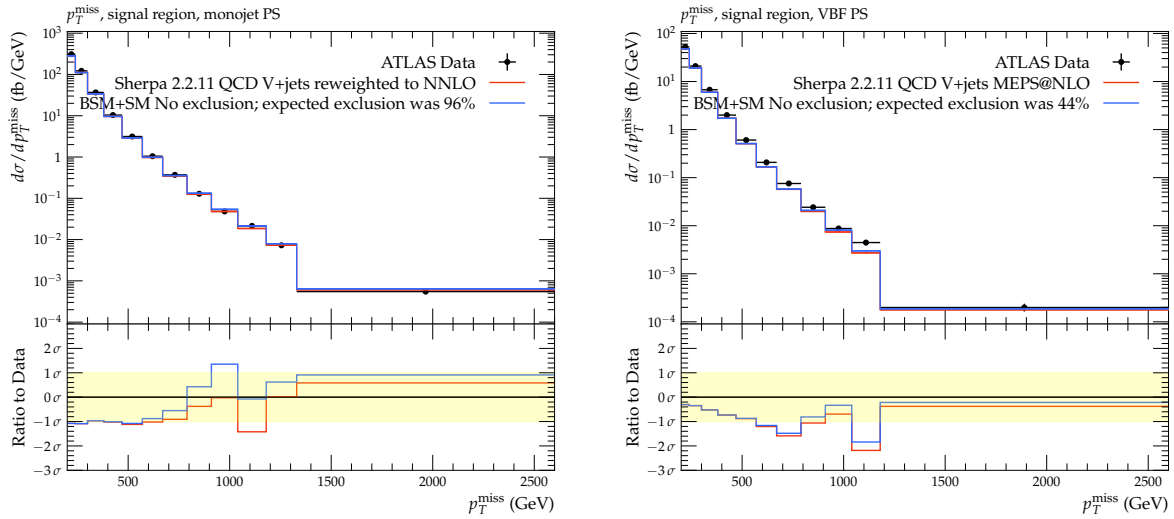


Figure 6.6: RIVET plots showing the measured p_T-miss differential cross-sections in the p_T-miss and jets region in the monojet and VBF phase spaces, in the ATLAS analysis from Reference [164]. The small excess that influences the discrepancy in the expected and observed exclusions can be seen in the bin around 1100 GeV in the VBF phase space plot.

Effect of the Interference Term

The process that contributes the most to the exclusion[6] is the $Y\bar{Y}_{QCD}$ process. However, the interference between the t-channel production of the mediator and anti-mediator pair $Y\bar{Y}_t$ and the QCD process can be calculated at LO, and at the cross-section can be rescaled using the k-factor in Equation 9 to get the new cross-section for the NLO process. The effect of the interference term can also be seen in Table 6.2: the term is always negative and as a result, the cross-section for the combined production of $Y\bar{Y}$ is less than the cross-section of the sum of the cross-sections of $Y\bar{Y}_{QCD}$ and $Y\bar{Y}_t$. The effect can be visualised by looking at Figure 6.8, and comparing them with Figure 6.4. In the both the LO and NLO cases, including the interference term broadens and flattens the peak of the 95% and 68% exclusion lines. This emphasizes the importance of including the interference term when setting the ultimate limits in the parameter space, especially if the BSM coupling λ is not set to 1, and the other processes have a bigger contribution to the overall cross-section of the production of a mediator and anti-mediator.

6.4 Conclusions

All of the scans performed in the study were made with the BSM coupling λ set to 1. The implications of using the different frameworks were clear: similar regions of the parameter space were excluded in both the measurement- and search-based approaches, although the use of MadAnalysis5 excluded more parameter points at high M_Y mass. The plots also clearly show that higher-order calculations increase the excluded region in the parameter space.

The project could be extended in a few ways. The BSM coupling could be varied over different λ values, the choice of which will be influenced by cosmological constraints, to see the effect of the variation on the cross-section and ultimately the exclusion of the parameter space.

[6] For the case $\lambda = 1$.

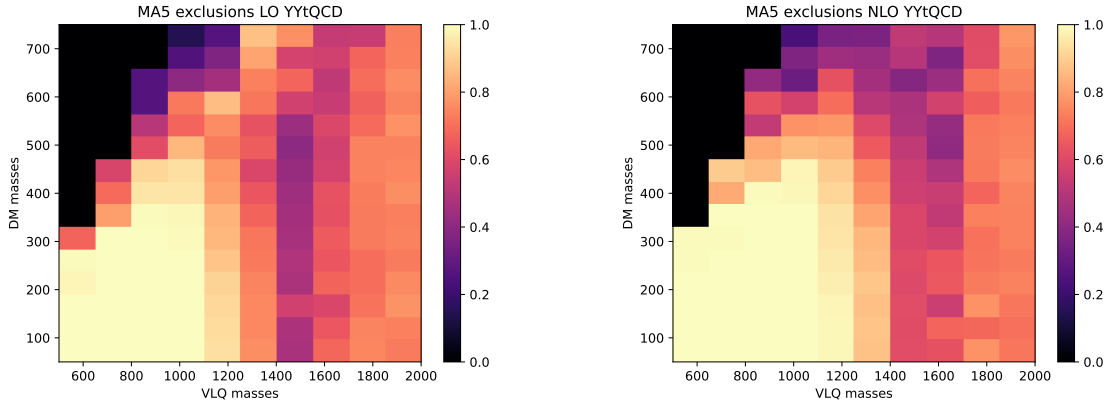


Figure 6.7: MadAnalysis5 exclusion plots for the $Y\bar{Y}_{QCD}$ process at LO (left) and at NLO (right). The leading contributions to the exclusions come from the ATLAS search for new particles in final states with jets and missing transverse momentum [170] in the lower M_Y regions and the CMS search for new particles with events with energetic jets and missing energy [171] in the higher M_Y region.

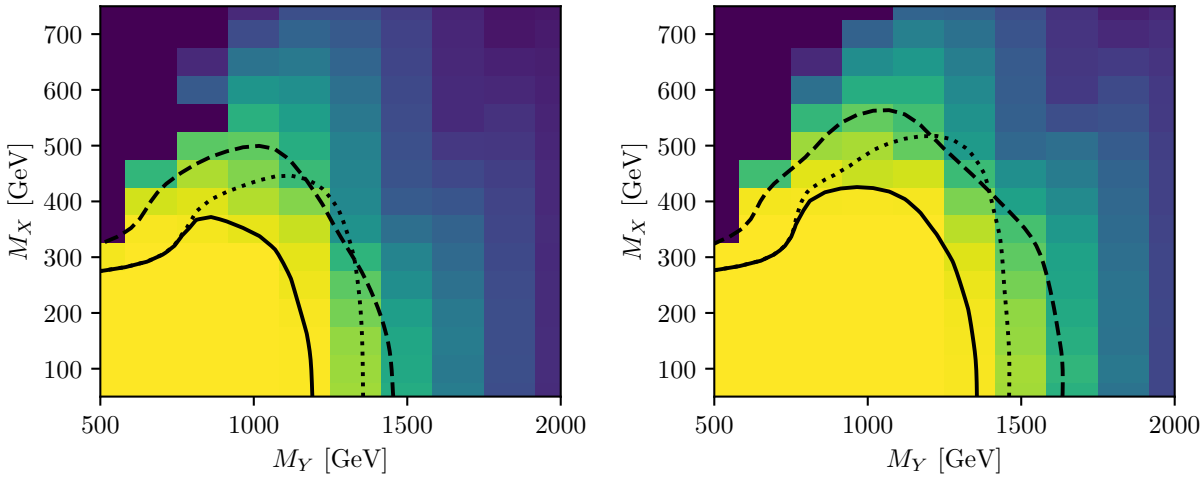


Figure 6.8: CONTUR exclusion plots for the $Y\bar{Y}$ process at LO (left) and at NLO (right), made by adding the contributions of the contributions of the $Y\bar{Y}_{QCD}$, $Y\bar{Y}_t$ and $Y\bar{Y}_i$ processes.

Additionally, the mass of the mediators could be assumed to be different from each other. Ultimately, the model setup was simplified, and next iterations of the study could aim to connect this simplified model to a concrete form featuring top partial compositeness.

7 Constraints on Dark-QCD Models

7.1 Theoretical Framework

Dark-QCD models are a class of extended dark sector models that are analogous to SM QCD. The SM is mirrored to have dark counterparts: dark quarks q_{dark} are charged under a new gauge group $SU(N_C^{dark})$, and have a number of different flavour possibilities given by N_F^{dark}, and dark gluons that interact with each other in similar ways that their SM inspirations interact via QCD. For the theory to be confined at a scale of Λ_{dark}, it is required that $N_F^{dark} < 3N_C^{dark}$ [172]. The confinement and hadronisation in the DS is assumed to lead to a spray of of composite states in the hidden sector, analogous to the process of confinement[1] and hadronisation[2] in the SM , and dark hadrons are formed. This follows a similar process to parton showers, and leads to dark showers and the formation of dark sector jets. The energy evolution in the DS plays an important role in the different dark shower signatures, further discussed in Section 7.2, but it follows the initial production at the hard process energy scale Q_{dark}. In SM QCD, the momentum flow from the hard-scattering energy scale Q to the confinement scale is led by collinear and soft singularities, meaning that perturbation theory can be used to describe the parton-showering process. Perturbation theory can also be used in the case of Dark-QCD, as long as the t'Hooft coupling $\lambda = \alpha_{dark}^2 N_C^{dark}$ is small enough [173]. Consequently, algorithms that are well-established can be used to model the parton evolution in the DS evolution, as explained in Section 2.4.2.

The dark showers include the production of dark mesons, which could possibly be degenerate, with masses m_{dark} and proper decay lengths $c\tau_{dark}$. The production of dark baryons is suppressed, since the masses scale with N_C^{dark}. The Dark-QCD models can be produced via a Z' mediator in the s-channel, or a bifundamental scalar Φ in the t-channel, as shown in Figure 7.1.

An important parameter in these models is the event-level fraction of unstable dark hadrons that decay into stable dark hadrons after the dark shower, R_{inv}. The effect of varying the R_{inv} parameter is illustrated in Figure 7.2: if all the dark hadrons are unstable on a collider timescale ($R_{\text{inv}} = 0$) the jet can easily be mistaken for a SM QCD jet, since all the dark hadrons have decayed to SM quarks. If stable and unstable dark hadrons are produced ($0 < R_{\text{inv}} < 1$), the jet will contain visible SM quarks and invisible stable dark hadrons and this results in Semi-Visible Jets (SVJs). If only stable dark hadrons are produced ($R_{\text{inv}} = 1$) the jet will be invisible to the detector since all of its constituent particles are dark. A Feynman diagram showing the

[1] Confinement is explained in Section 2.1.4

[2] Hadronisation is explained in more detail in Section 2.4.2.

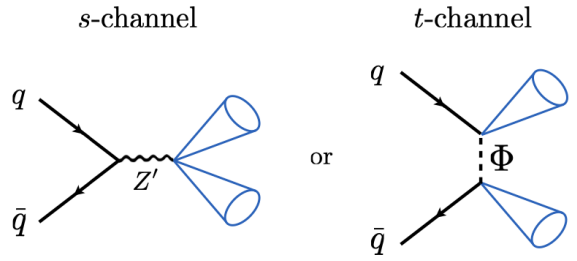


Figure 7.1: Production of the Dark-QCD signatures via a mediator Z' in the s-channel, or through a bifundamental scalar Φ in the t-channel, taken from [174].

production of a SVJ is shown in the left diagram in Figure 7.3.

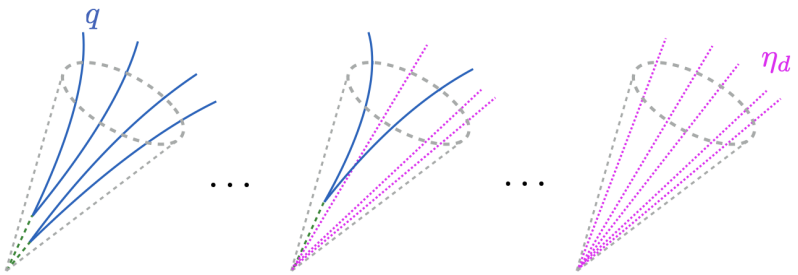


Figure 7.2: Diagrams illustrating how varying R_{inv} affects the jet-type. The left diagram shows the case of $R_{\text{inv}} = 0$, where only unstable dark hadrons (dotted green line) that decay to SM quarks (solid blue line) are produced. The middle diagram shows the case of $0 < R_{\text{inv}} < 1$, where stable dark hadrons (dotted pink line) and unstable dark hadrons are produced, resulting in Semi-Visible Jets. The diagram on the right shows the case $R_{\text{inv}} = 1$, where only stable dark hadrons are produced. Taken from [174].

The proper decay length $c\tau_{dark}$ also affects the Dark-QCD signature. In the case that dark mesons are produced on a shorter timescale than the dark-meson decay to SM quarks, then the dark mesons travel a significant distance and then decay to SM quarks. This forms an emerging jet. The decays of the dark mesons form multiple smaller displaced jets, which in turn form the emerging jet. A Feynman diagram showing the production of an emerging jet is shown in the middle of Figure 7.3, and the relationship between the parameters R_{inv} and $c\tau_{dark}$ is shown in Figure 7.4. A discussion of the novel detector final states that these jets result in, follows in Section 7.2.

7.2 Novel Detector Final States

Searches for Dark-QCD are determined to the available final states in the detector, and searches are generally designed to be model-independent. As introduced in the previous section, there are two definitions of R_{inv} used interchangeably in the literature:

- the fraction of stable dark hadrons relative to all dark hadrons in the event R_{inv}^{ratio}
- the event-level fraction of unstable dark hadrons that decay into stable dark hadrons after the dark shower R_{inv}^{BF}

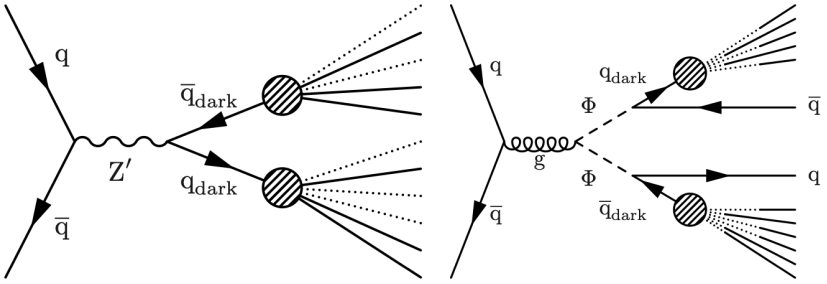


Figure 7.3: Feynman diagrams illustrating the production of semi-visible jets (left), emerging jets (right). Taken from [75].

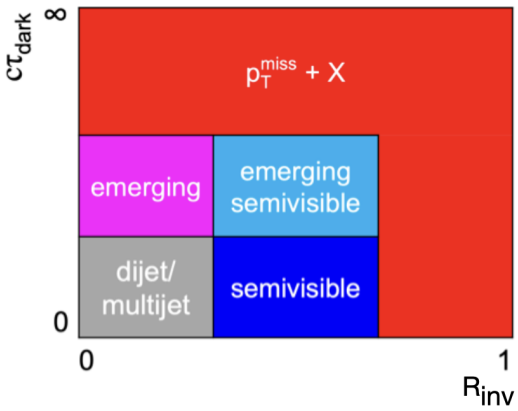


Figure 7.4: Graph showing the relationship between the parameters R_{inv} and $c\tau_{dark}$. The grey block indicates SM dijet or multijet events, where no unstable dark hadrons are produced, or if the lifetime of the dark hadrons are small enough for prompt decay to SM particles. The light-blue block shows the overlap of emerging jet signatures and SVJs, and the red portion of the graph represents the experimental signature of missing transverse momentum p_T^{miss} (from invisible particles) and the production of some visible SM signature labelled X. Taken from [75].

R_{inv}^{BF} is used as an input parameter in the Pythia8 Hidden Valley runcard, and experimentally it is challenging to define or use an output R_{inv} based on dark hadron multiplicities, since there is no way to construct a measurable particle-level output observable.

The novel final states can broadly be split into three classes: dark jets, semi-visible jets and emerging jets, with the classification based on R_{inv} values and the lifetime of the dark hadrons.

While not a focus of this work, it is useful to note that in the emerging jets scenario, the lifetime of the dark quarks plays an important role. The non-prompt decay of the dark quarks lead to displaced vertices. Calorimeter jets containing predominantly displaced tracks and with different vertices inside the cone are used as the final state in this scenario [175]. This final state is used to investigate composite dark sectors, where a parton shower in the dark sector is followed by displaced decays of dark mesons (π_D and ρ_D) back to SM jets. The dark meson decays happen at different points from the interaction point, leading to the slow emergence of the jet in the detector. Both CMS and ATLAS have recently come out with searches for emerging jets [176, 177].

7.2.1 Dark Jets

The first class of unusual jet-like final states that are caused by Dark-QCD and that have been studied by ATLAS [178], Dark Jets are/can be formed from the decay of a heavy Z' resonance, which decay into a dark quark pair. These dark quarks hadronise to form dark hadrons, which then decay back into SM particles. The fraction of invisible components, the stable dark hadrons, produced or left over are assumed to be negligible (R_{inv} =0). The final detector objects appear as jets with properties that depend on the underlying theory parameters.

The double hadronisation that takes place in the formation of the dark jets lead to wider jets than their SM QCD counterparts. First, there is the dark sector hadronisation, after which dark mesons decay into high-momentum SM quarks. These SM quarks then undergo standard hadronisation and form SM jets. Furthermore, investigating the substructure in these jets can help distinguish dark jets from SM QCD jets. Tracks associated to SM gluon and quark jets mostly come from charged pions, while charged particles inside the dark jets come from charged rho meson decays. Using tracks and jet-substructure as a distinguishing factor in dark-jet identification is model-dependent [179], and is dependent on the dark fragmentation and dark meson mass, and the decay channels of the dark mesons into SM quarks. In the case of the ATLAS analysis [178], the dark jets had a larger charged-particle multiplicity than their SM counterparts and this was used to distinguish SM QCD di-jet final states to dark sector di-jet final states.

7.2.2 Semi-Visible Jets

Arising from the hypothetical strongly-interacting dark sector, the parton evolution of Semi-Visible Jets (SVJs) includes the production and decay of dark quarks inside hadronic jets [180]. In the scenario where two dark quarks are produced, and dominantly interact with SM QCD, a fraction of the unstable dark mesons (π_D and ρ_D) produced in hadronisation promptly decay to SM quarks, while the rest decay to stable dark mesons (π'_D and ρ'_D). The input parameter R_{inv} is used in Pythia8 to set this fraction. As a result, the final state visible in the detector is a multi-jet final state, with the missing transverse energy/momentum aligned with one of the jets.

SVJs are the second class of dark-sector jets that have been studied by both ATLAS [181] and CMS [182]. The ATLAS search was for the non-resonant (t-channel) production mode of SVJs, while the CMS search was for the resonant (s-channel) production mode.

The experimental results add to recent developments in the phenomenology and theory behind SVJs. These developments include ways to establish systematic uncertainties on SVJ production to account for systematic errors in signal modelling [183], testing jet substructure (or similar) variables [179] [184] [185], and machine-learning techniques to distinguish between SVJs and Standard Model jets [186–191]. New SVJ production modes have expanded the theoretical environment to include ISR [192], where the SVJ is produced with some particle X, b-jet SVJs [193] where only heavy flavour SM quarks are considered in the dark shower, and the production of SVJs through dark glueballs [194], where the glueballs (composite particles that only contain gluons) are the lightest dark hadronic states. As new production modes develop, it is natural for new signatures involving SVJs to develop too: SVJ models with light leptons [195], tau leptons [196] and photons [197] have been developed. Community contributions and reviews for SVJ Monte Carlo generation and modelling have been discussed and

presented in the Snowmass white paper [172] and the MITP Colours in Darkness workshop summary report [198].

7.3 Probing the sensitivity of SVJs to current LHC measurements using the CONTUR toolkit

In light of developments in SVJ signatures and models, re-interpretation of SM measurements is crucial to determine future search strategies and model development. Using CONTUR, this work derived constraints on selected SVJ models and parameter choices, in resonant and non-resonant production modes.

7.3.1 SVJ Generation

For the resonant production mode, samples are generated using Pythia8 where a pair of dark quarks are generated via a heavy Z' mediator. In the non-resonant case, the dark quarks are generated through a scalar bifundamental mediator using the UFO in Ref. [199] in MadGraph [34], as expressed in Ref. [174]. For both production modes, the dark quarks undergo dark hadronisation using the Pythia8 Hidden Valley (HV) module, and for the non-resonant case, the particle IDs of the DM candidates were changed to match the HV particle ID scheme. The dark hadronisation gives rise to flavour-diagonal (spin 0) and off-diagonal (spin 1) π_D and ρ_D mesons.

The HV module has many parameters that can be changed for dark hadronisation. These parameters are important on a theoretical and phenomenological level, but do not influence the final state topology. For the two models considered here, the parameters of importance are:

- the Dark-QCD confinement scale value (Λ_D)
- the number of dark colours (N_C)
- the number of dark flavours (N_F)
- the dark quark masses (M_{q_D}
- the dark hadron masses (M_{ρ_D}, M_{π_D})

In any model involving SVJs, a crucial parameter is R_{inv} , as described in Section 7.2. The unstable dark hadrons, with mass choices to ensure decays that are kinematically possible, decay to SM quarks and stable dark hadrons in a ratio dependent on R_{inv}. R_{inv} is not a fundamental theory parameter, but is used as a handle to generate and scan different kinematics for the collider final state. The definition used in the event generation is therefore the same as defined for R_{inv}^{BF}, with the parameter $(1 - R_{inv})$ defined as the fraction of decays of dark quarks into SM particles.

In this study, flavour-diagonal π_D and ρ_D mesons were promptly decayed into off-diagonal stable dark π_D and ρ_D pairs respectively, as well as SM quarks.

Parameter	Range	Comments
$M_{Z'}$	1, 3, 5 TeV	Both channels
M_{π_D}	10, 50, 100 TeV	Both channels
R_{inv}	0.0 - 1.0	Both channels
N_F	1, 2, 3	Only s-channel
λ	0.1 - 7	Only t-channel
M_{ρ_D}	16, 80, 160 TeV	Function of M_{π_D}
Λ_D	5, 25, 50	Function of M_{π_D} and M_{ρ_D}
pTminFSR	5.5, 7.5, 55	Function of Λ_D

Table 7.1: Parameter and ranges on which the CONTUR scans were performed. The parameters in the lower bock depend on parameters set in the upper block.

7.3.2 Constraints on SVJs

The study used the CONTUR toolkit [93,94] to place constraints on the SVJ signatures using measurements made at the LHC, with the goal of gaining insights from these measurements that are complimentary to the experimental results in the s- and t-channel searches. The SVJ final states are dominated by jets and p_T^{miss}, and so measurements with a purely hadronic final state are considered in this study.

For both production modes, the number of dark flavours is set to two ($N_F = 2$). This does not produce the same fraction of dark hadrons in the output as specified by the R_{inv} input parameter. This is because stable dark π and ρ mesons can also be directly produced during the dark hadronisation, rather than exclusively during decays. The dark quark mass is set to 10 GeV, while the ρ_D meson mass was set to 1.6 times the mass of the π_D meson, following the Snowmass report [172]. The corresponding off-diagonal π_D and ρ_D meson masses were set to 0.01 GeV less than half of the corresponding flavour-diagonal ones. The number of dark colours was set to 3, and the Pythia8 HV coupling α_{dark} was set to be running at one-loop. The dark-QCD confinement scale Λ_D was calculated for each dark meson mass, again following the guidelines in [172], and the lowest allowed p_T of the HV Final State Radiation (FSR) emission (pTminFSR) was set to 1.1 times Λ_D.

Fixing these parameters meant that a simple scan could be performed in which the mediator mass, flavour-diagonal π_D mass and input R_{inv} parameter values were varied. In the s-channel production mode, a further scan was performed in which N_F was varied, while in the t-channel production mode, the coupling strength between the SM and the DM sector λ was varied. Varying λ effectively translates to a cross-section scaling, since the cross-section scales as λ^4 without affecting the kinematic distributions for mediator masses above 2.5 TeV. Scaling the cross-sections do not affect the validity of the model. The parameter values used in the scan are shown in Table 7.1.

Resonant Production Mode

For the resonant production mode, the SVJ signature was generated using the Pythia8 HV module, with a Z' mediator decaying to a dark-quark pair. The cross-section of the process is very low in the default Pythia8 setup, and so the cross-sections were scaled up to match the cross-sections in the CMS search [182] to increase the sensitivity and derive meaningful exclusions, as seen in Table 7.2. This study is considered to be a proof-of-principle exercise, since the CMS search set strong constraints on the topology, and the cross-section of the

process is highly model-parameter dependent. The sensitivity of measurements on the shapes of the kinematic distributions is nonetheless explored.

$M_{Z'}$ [TeV]	Generated cross-section [pb]	Scaled cross-section [pb]
1.0	1.29×10^{-2}	6.69
1.5	1.42×10^{-3}	1.88
2.0	2.48×10^{-4}	0.47
2.5	5.68×10^{-5}	0.13
3.0	1.49×10^{-5}	0.004

Table 7.2: Generated and scaled cross-sections for the different Z' masses in the resonant channel.

The most sensitive analysis for the SVJ signature is the ATLAS differential cross-section measurement of events with missing transverse momentum and jets [200], where only the cross-section distributions were used rather than their ratios.

The $p_{\mathrm{T}}^{\mathrm{miss}}$ distribution for the parameter choices $M_{Z'} = 1$ TeV, $M_{\pi_D} = 100$ GeV is shown in Figure 7.5. This is for a representative value of R_{inv} of 0.5 and $N_F = 2$. Subsequent plots will show how the M_{π_D} choice drives the exclusion values.

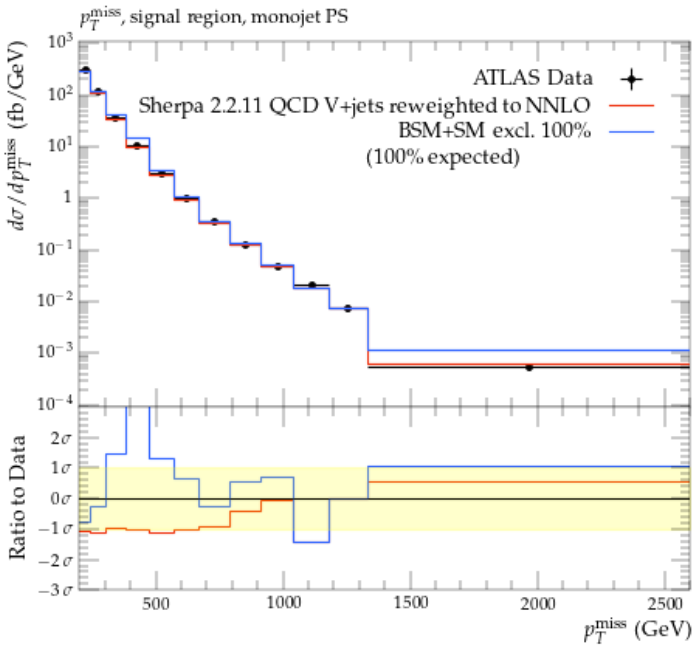


Figure 7.5: The dominant exclusion histogram for the s-channel process with $M_{Z'} = 1$ TeV, $M_{\pi_D=100}$ GeV, $R_{\mathrm{inv}} = 0.5$, and $N_F = 2$. The exclusion is driven by the missing energy (MET) distribution measured in [200] (specifically, Figure 7a). The black points represent the data from ATLAS. The blue line shows the predicted events from the new physics benchmark added to the SM prediction, which shows a non-negligible disagreement with the number of observed events in data. The red line shows the SM prediction.

Figure 7.6 shows the exclusion of M_{π_D} as a function of $M_{Z'}$, for R_{inv} values of 0.2, 0.5 and 0.8. The binned heatmaps used for the exclusion plot range from dark blue (0 CLs) to yellow

(1.0 CLs), and the exclusion contours are drawn from this, where CLs refer to the common limit setting technique of confidence limits [95]. The black solid line is the 95%-confidence exclusion, the black dashed line is 68% and the black dotted line is the 95% expected exclusion.

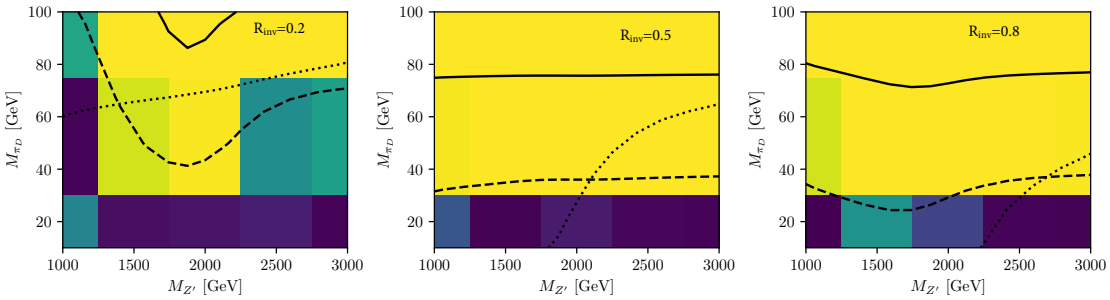


Figure 7.6: Contours showing the exclusion for the s-channel process as a function of M_{π_D} and $M_{Z'}$ for R_{inv} values of 0.2, 0.5 and 0.8 are shown respectively. The dotted line is the expected exclusion, the dashed line is the observed 68% CL exclusion and the solid line is the observed exclusions at 95% CL. The area above the curves is excluded. The yellow regions in the plots are excluded, while the blue regions are not excluded. Smooth exclusion contours are achieved through interpolation functions based on the exclusion of each bin in the heatmap.

The conclusion drawn for this proof-of-principle study is that for the chosen coupling value of the Z' mediator to the dark quarks, where 100% branching fraction for this decay is assumed, measurements place more stringent constraints on higher values of the dark pion masses M_{π_D}, except at low R_{inv} and low $M_{Z'}$.

Plotting the exclusion of R_{inv} as a function of $M_{Z'}$ for different M_{π_D}, supports this conclusion, and can be seen in Figure 7.7. All the plots were made with the number of flavours N_F set to 2.

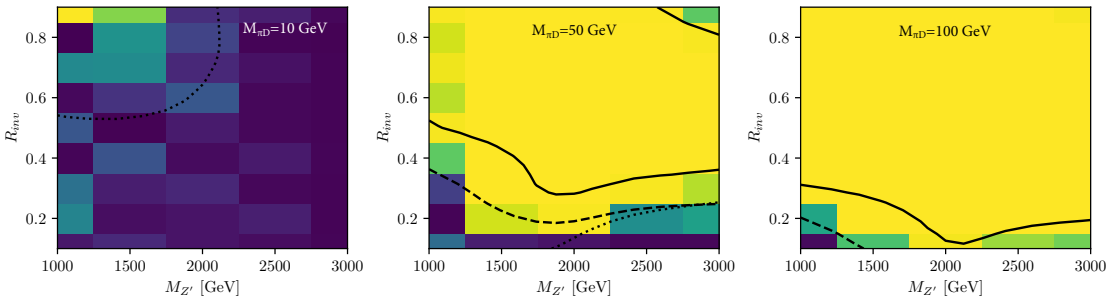


Figure 7.7: Contours showing the exclusion for the s-channel process as a function of R_{inv} and $M_{Z'}$ for M_{π_D} values of 10, 50 and 100 GeV are shown. The dotted line is the expected exclusion, the dashed line is the observed 68% CL exclusion and the solid line is the observed exclusions at 95% CL. The area above the curves is excluded. The yellow regions in the plots are excluded, while the blue regions are not excluded. Smooth exclusion contours are achieved through interpolation functions based on the exclusion of each bin in the heatmap.

An additional check on the choice of number of flavours was also conducted, to see if higher or lower values would be constrained. This is shown in Figure 7.8, where the top panel shows the exclusion plots for a fixed M_{π_D} of 10 GeV and varying R_{inv} , and the bottom panel for a fixed R_{inv} and varying $M_{Z'}$. The sensitivity is dependent on the dark pion masses, as the Z' mediator

masses, but the exclusions are not sensitive to the changes in N_F. The CMS result [182], using a Z' with a universal coupling of 0.25 to the SM quarks, excluded Z' masses of 1.5-4.0 TeV at 95% confidence level, depending on the other signal-model parameters.

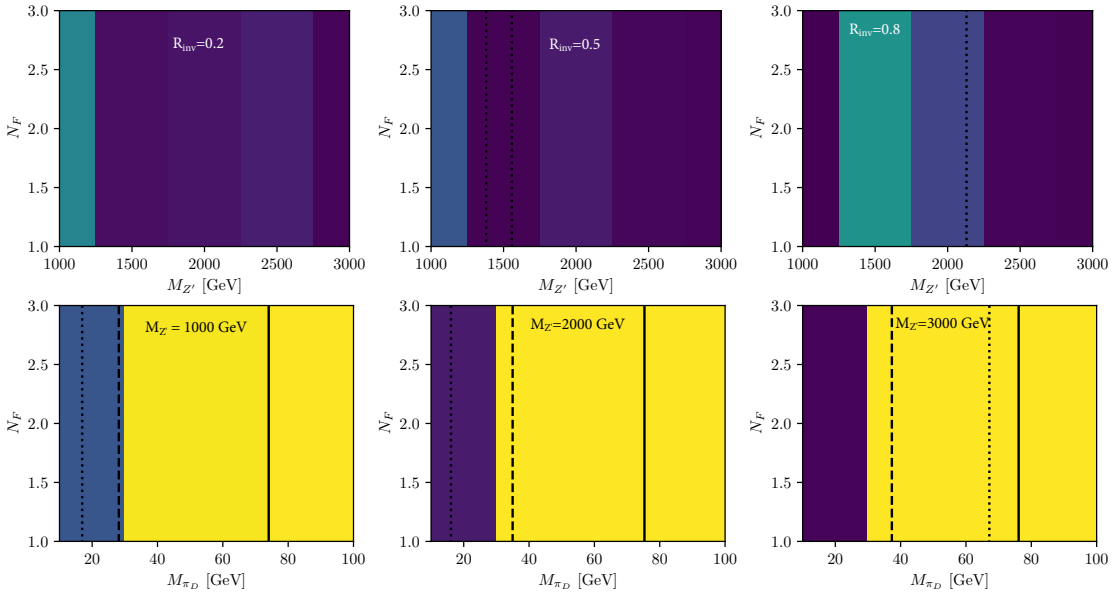


Figure 7.8: Contours showing the exclusion for the s-channel process as a function of N_F and R_{inv} or $M_{Z'}$ are shown. The dotted line is the expected exclusion, the dashed line is the observed 68% CL exclusion and the solid line is the observed exclusions at 95% CL. The area to the left of the curves is excluded.

Non-Resonant Production Mode

Following Reference [199], the t-channel SVJ signature was generated using Madgraph5 to calculate matrix elements with up to two extra partons at LO. The MLM [201] jet matching scheme, with the matching parameter set to 100 GeV, was used and showering was done in Pythia8, again making use of the HV module. The cross-sections for the different mediator masses for the coupling strength $\lambda = 1$ is show in Table 7.3.

M_{med} [TeV]	Generated cross-section [pb]
1.0	2.11
1.5	0.44
2.0	0.14
2.5	0.006
3.0	0.003

Table 7.3: The generated cross-sections for different M_{med} values for the t-channel process for $\lambda = 1$.

Due to the similar final state, the most sensitive analysis for the t-channel signature is once again the ATLAS differential cross-section measurement of events with missing transverse momentum and jets [200], but this time the ratio measurements were included. The $p_{\text{T}}^{\text{miss}}$ distribution shown in Figure 7.9, for $M_{\pi_D} = 50$ GeV, $\lambda = 2.5$ and R_{inv} set to 0.5, is taken from the comparison to the ATLAS measurement. For these parameter choices, λ drives the exclusion.

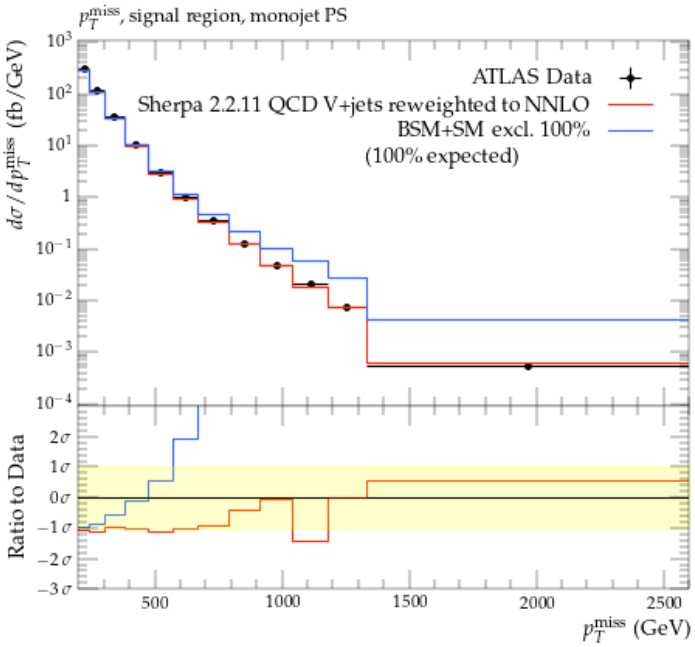


Figure 7.9: The dominant exclusion histogram for the t-channel process with $M_{med} = 1$ TeV, $M_{\pi_D=50}$ GeV, $R_{\text{inv}} = 0.5$, and $\lambda = 2.5$. The exclusion is driven by the missing energy (MET) distribution measured in [200] (specifically, Figure 7a). The black points represent the data from ATLAS. The blue line shows the predicted events from the new physics benchmark added to the SM prediction, which shows a non-negligible disagreement with the number of observed events in data, and the red line shows the SM prediction.

The exclusion for M_{π_D} as a function of M_{med} for R_{inv} values of 0.2, 0.5 and 0.8 are shown in Figure 7.10. There is a dependence of R_{inv} for excluded mediator masses, and mediator masses up to 1.75 TeV are excluded for high R_{inv} values.

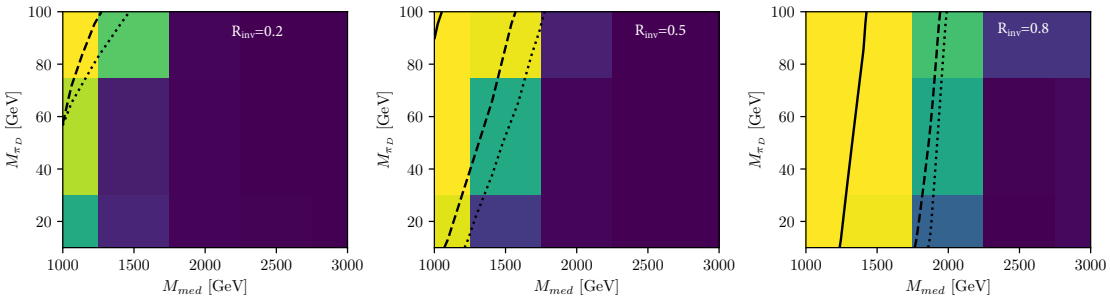


Figure 7.10: Contours showing the exclusion for the t-channel process as a function of M_{π_D} and M_{med} for R_{inv} values of 0.2, 0.5 and 0.8 are shown. The dotted line is the expected exclusion, the dashed line is the observed 68% CL exclusion and the solid line is the observed exclusions at 95% CL. The area to the left of the curves is excluded.

Figure 7.11 shows the exclusion plots for R_{inv} versus M_{med} for different values of M_{π_D}, and these plots confirm that higher values of M_{π_D} are excluded, except at low R_{inv} and M_{med}.

The plots in Figures 7.10 and 7.11 are all made with the λ coupling set to unity. For values of λ greater than 7.5, the entire parameter space is excluded. However, varying λ can give insights into how cross-section scaling changes exclusions, as seen in 7.12. The exclusions

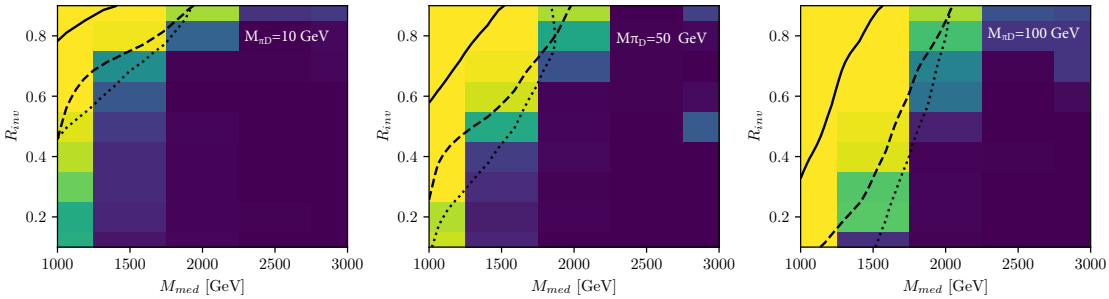


Figure 7.11: Contours showing the exclusion for the t-channel process as a function of R_{inv} and M_{med} for M_{π_D} values of 10, 50 and 100 GeV are shown. The dotted line is the expected exclusion, the dashed line is the observed 68% CL exclusion and the solid line is the observed exclusions at 95% CL. The area to the left of the curves is excluded.

are shown for a fixed π_D mass of 10 GeV, for different values of R_{inv} , and plotting M_{med} versus λ. These results set a stringent limit on the specific production cross-section of these signals. The ATLAS search [181] set a limit of up to 2.7 TeV on M_{med} for λ set to unity, and the number of flavours, N_F, set to 1. A direct comparison with the public experimental result is not possible, due to the shift to a physically motivated value of N_F for the current study.

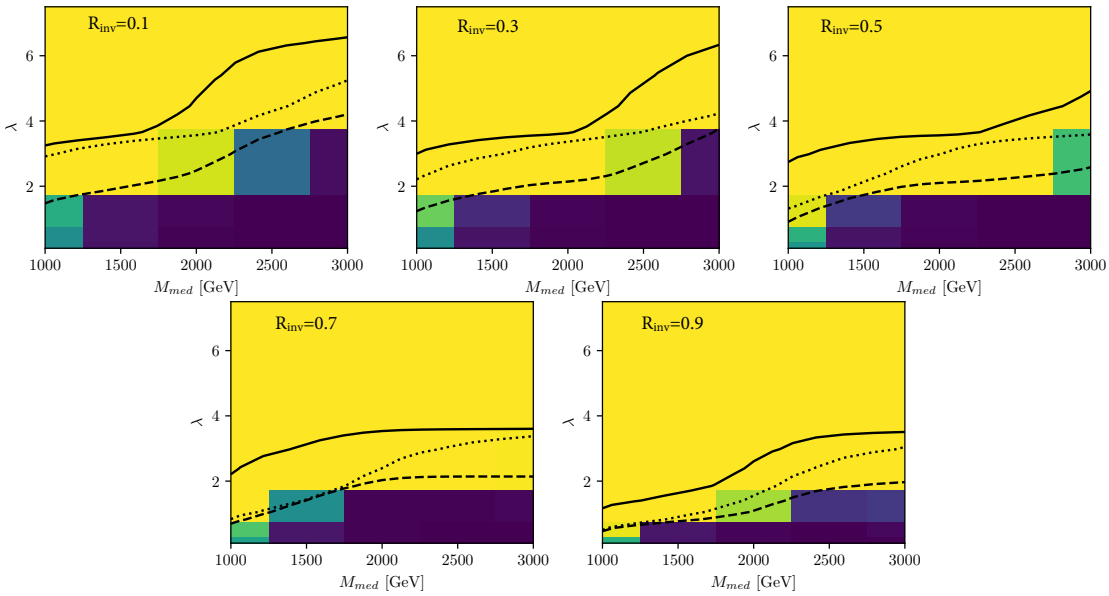


Figure 7.12: Contours showing the exclusion for the t-channel process as a function of R_{inv} and M_{med} are shown. The dotted line is the expected exclusion, the dashed line is the observed 68% CL exclusion and the solid lines represent the observed exclusions at 95% CL. The area to the left of the curves is excluded.

7.3.3 Summary

This chapter presents a study covering resonant and non-resonant production modes of SVJs, an exciting and developing research area in novel final state topologies. The parameter space of benchmark SVJ models generated using the Pythia8 HV module are constrained by the ATLAS differential cross-section measurement of events with missing transverse momentum

and hadronic jets. The constraints presented here are generally weaker than those set by the CMS and ATLAS searches, but are applicable to $p_{\mathrm{T}}^{\mathrm{miss}}$ values lower than the ATLAS search in the non-resonant case, showing complementarity with the existing results.

8 Conclusions

The validity of the Standard Model was cemented by the discovery of the Higgs boson, but the work to understand the missing pieces in particle physics is not yet done. This thesis introduced some BSM models and hypothetical particles that aim to answer the question of Dark Matter in the context of collider experiments. The focus was on Dark Sector models that introduce hypothetical particles and quantum fields and give a framework in which searches can be carried out at colliders.

A large component of the work presented was done as part of an ATLAS search for a Maverick top partner that decays into a Dark Photon, which then decays into a collimated lepton pair. The work required a good understanding of various frameworks and experimental knowledge, and the analysis is ongoing. The importance of operations in big collaborations was briefly touched upon, through the inclusion of a summer project working on the ATLAS Trigger Menu.

Two phenomenological models were explored and included the use of frameworks for reinterpretation. The first was a t-channel DM model, and the project involved a range of generators at different levels of complexity. The model was split into several sub-processes, which were run at LO and at NLO. The results from each sub-process were compared, and the exclusions obtained from the two reinterpretation frameworks, CONTUR and MadAnalysis5, were compared as well. The second study used CONTUR to place exclusions on Semi-Visible Jets, a novel final state topology.

Performing phenomenological studies and experimental searches go hand-in-hand. The field is in a position where new models can be excluded using data from the LHC, and this should be a driving force to direct dedicated searches. The work presented in this thesis relied on skills and techniques that will always be relevant, and that can be built upon, in searches for Dark Matter at colliders.

Bibliography

[1] S. Weinberg, The Making of the Standard Model, The European Physical Journal C 34 (1) (2004) 5–13. doi:10.1140/epjc/s2004-01761-1.

[2] T. W. B. Kibble, The Standard Model of Particle Physics (2014). arXiv:1412.4094.

[3] ATLAS Collaboration, Observation of a New Particle in the Search for the Standard Model Higgs Boson with the ATLAS Detector at the LHC, Physics Letters B 716 (1) (2012) 1–29. doi:10.1016/j.physletb.2012.08.020.

[4] CMS Collaboration, Observation of a New Boson at a Mass of 125 GeV with the CMS Experiment at the LHC, Physics Letters B 716 (1) (2012) 30–61. doi:10.1016/j.physletb.2012.08.021.

[5] A. Arbey, F. Mahmoudi, Dark Matter and the Early Universe: A Review, Progress in Particle and Nuclear Physics 119 (2021) 103865. doi:10.1016/j.ppnp.2021.103865.

[6] K. Freese, Status of Dark Matter in the Universe, International Journal of Modern Physics D 26 (06) (2017) 1730012. doi:10.1142/s0218271817300129.

[7] S. L. Glashow, Partial-Symmetries of Weak Interactions, Nuclear Physics 22 (1961). doi:10.1016/0029-5582(61)90469-2.

[8] M. Gell-Mann, A Schematic Model of Baryons and Mesons, Phys. Lett. 8 (1964) 214–215. doi:10.1016/S0031-9163(64)92001-3.

[9] G. Zweig, An SU(3) Model for Strong Interaction Symmetry and its Breaking., 1964, pp. 22–101. doi:10.17181/CERN-TH-412.

[10] O. W. Greenberg, Spin and Unitary-Spin Independence in a Paraquark Model of Baryons and Mesons, Phys. Rev. Lett. 13 (1964) 598–602. doi:10.1103/PhysRevLett.13.598.

[11] F. Englert, R. Brout, Broken Symmetry and the Masses of Gauge Vector Mesons, Phys. Rev. Lett. 13 (1964) 321–323. doi:10.1103/PhysRevLett.13.321.

[12] P. W. Higgs, Broken Symmetries, Massless Particles and Gauge Fields, Phys. Lett. 12 (1964) 132–133. doi:10.1016/0031-9163(64)91136-9.

[13] P. W. Higgs, Broken Symmetries and the Masses of Gauge Bosons, Phys. Rev. Lett. 13 (1964) 508–509. doi:10.1103/PhysRevLett.13.508.

[14] G. S. Guralnik, C. R. Hagen, T. W. B. Kibble, Global Conservation Laws and Massless Particles, Phys. Rev. Lett. 13 (1964) 585–587. doi:10.1103/PhysRevLett.13.585.

[15] S. Weinberg, A Model of Leptons, Phys. Rev. Lett. 19 (1967) 1264–1266. doi:10.1103/PhysRevLett.19.1264.

[16] A. Salam, Weak and Electromagnetic Interactions, Conf. Proc. C 680519 (1968) 367–377. doi:10.1142/9789812795915_0034.

[17] D. J. Gross, F. Wilczek, Ultraviolet Behavior of Non-Abelian Gauge Theories, Phys. Rev. Lett. 30 (1973) 1343–1346. doi:10.1103/PhysRevLett.30.1343.

[18] H. D. Politzer, Reliable Perturbative Results for Strong Interactions?, Phys. Rev. Lett. 30 (1973) 1346–1349. doi:10.1103/PhysRevLett.30.1346.

[19] L. Kluberg, Neutral Currents in Gargamelle, in: 9th Rencontres de Moriond: high energy leptonic interactions, 1974, pp. 111–123.

[20] M. L. Perl, The Discovery of the Tau Lepton, NATO Sci. Ser. B 352 (1996) 277–302. doi:10.1007/978-1-4613-1147-8_15.

[21] J. Yoh, The Discovery of the b-Quark at Fermilab in 1977: The Experiment Coordinator's Story, AIP Conf. Proc. 424 (1) (1998) 29–42. doi:10.1063/1.55114.

[22] UA1 Collaboration, Experimental Observation of Isolated Large Transverse Energy Electrons with Associated Missing Energy at $\sqrt{s} = 540$ GeV, Phys. Lett. B 122 (1983) 103–116. doi:10.1016/0370-2693(83)91177-2.

[23] UA2 Collaboration, Observation of Single Isolated Electrons of High Transverse Momentum in Events with Missing Transverse Energy at the CERN anti-p p Collider, Phys. Lett. B 122 (1983) 476–485. doi:10.1016/0370-2693(83)91605-2.

[24] UA1 Collaboration, Experimental Observation of Lepton Pairs of Invariant Mass Around 95-GeV/c^2 at the CERN SPS Collider, Phys. Lett. B 126 (1983) 398–410. doi:10.1016/0370-2693(83)90188-0.

[25] D0 Collaboration, Observation of the Top Quark, Physical Review Letters 74 (14) (1995) 2632–2637. doi:10.1103/physrevlett.74.2632.

[26] ATLAS Collaboration, The Standard Model, general Photo (2021).
URL https://cds.cern.ch/record/2765709

[27] G. Hooft, The Evolution of Quantum Field Theory: From QED to Grand Unification, 2016, p. 1–27. doi:10.1142/9789814733519_0001.

[28] ATLAS Collaboration, Combined Measurement of the Higgs Boson Mass from the $H \to \gamma\gamma$ and $H \to ZZ^* \to 4\ell$ Decay Channels with the ATLAS Detector Using $\sqrt{s} = 7$, 8, and 13 TeV pp Collision Data, Phys. Rev. Lett. 131 (25) (2023) 251802. doi:10.1103/PhysRevLett.131.251802.

[29] K. G. Wilson, Confinement of Quarks, Phys. Rev. D 10 (1974) 2445–2459. doi:10.1103/PhysRevD.10.2445.

[30] M. Thomson, Modern Particle Physics, Cambridge University Press, New York, 2013. doi:10.1017/CBO9781139525367.

[31] J. Ellis, Higgs Physics (2013). arXiv:1312.5672.

[32] P. A. Zyla, et al., Review of Particle Physics, PTEP 2020 (8) (2020) 083C01. doi:10.1093/ptep/ptaa104.

[33] R. P. Feynman, Space-time Approach to Quantum Electrodynamics, Phys. Rev. 76 (1949) 769–789. doi:10.1103/PhysRev.76.769.

[34] J. Alwall, R. Frederix, S. Frixione, V. Hirschi, F. Maltoni, O. Mattelaer, H.-S. Shao, T. Stelzer, P. Torrielli, M. Zaro, The automated computation of tree-level and next-to-leading order differential cross sections, and their matching to parton shower simulations, Journal of High Energy Physics 2014 (7) (Jul. 2014). doi:10.1007/jhep07(2014)079.

[35] M. H. Seymour, M. Marx, Monte Carlo Event Generators (2013). arXiv:1304.6677.

[36] D. Kar, Experimental Particle Physics: Understanding the Measurements and Searches at the Large Hadron Collider, Institute of Physics Pub, 2019. doi:10.1088/2053-2563/ab1be6.

[37] J. Alwall, M. Herquet, F. Maltoni, O. Mattelaer, T. Stelzer, MadGraph 5: Going Beyond, Journal of High Energy Physics 2011 (6) (Jun. 2011). doi:10.1007/jhep06(2011)128.

[38] D. E. Soper, Parton Distribution Functions, Nuclear Physics B - Proceedings Supplements 53 (1–3) (1997) 69–80. doi:10.1016/s0920-5632(96)00600-7.

[39] A. Buckley, J. Ferrando, S. Lloyd, K. Nordström, B. Page, M. Rüfenacht, M. Schönherr, G. Watt, LHAPDF6: Parton Density Access in the LHC Precision Era, The European Physical Journal C 75 (3) (Mar. 2015). doi:10.1140/epjc/s10052-015-3318-8.

[40] J. Alwall, et al., A Standard Format for Les Houches Event Files, Computer Physics Communications 176 (4) (2007) 300–304. doi:10.1016/j.cpc.2006.11.010.

[41] B. Webber, Hadronization (1994). arXiv:hep-ph/9411384.

[42] J. Altmann, A. Dubla, V. Greco, A. Rossi, P. Skands, Towards the Understanding of Heavy Quarks Hadronization: From Leptonic to Heavy-ion Collisions, The European Physical Journal C 85 (1) (Jan. 2025). doi:10.1140/epjc/s10052-024-13641-5.

[43] Z. Nagy, D. E. Soper, What is a Parton Shower?, Physical Review D 98 (1) (Jul. 2018). doi:10.1103/physrevd.98.014034.

[44] C. Bierlich, S. Chakraborty, N. Desai, L. Gellersen, I. Helenius, P. Ilten, L. Lönnblad, S. Mrenna, S. Prestel, C. T. Preuss, T. Sjöstrand, P. Skands, M. Utheim, R. Verheyen, A Comprehensive Guide to the Physics and Usage of PYTHIA 8.3 (2022). arXiv:2203.11601.

[45] P. Bartalini, J. R. Gaunt, et al., Multiple Parton Interactions at the LHC, Vol. 29, WSP, 2019. doi:10.1142/10646.

[46] B. Andersson, G. Gustafson, B. Soderberg, A General Model for Jet Fragmentation, Z. Phys. C 20 (1983) 317. doi:10.1007/BF01407824.

[47] T. Sjöstrand, Jet Fragmentation of Multiparton Configurations in a String Framework, Nuclear Physics, Section B 248 (2) (1984) 469–502. doi:10.1016/0550-3213(84)90607-2.

[48] A. Buckley, P. Ilten, D. Konstantinov, L. Lönnblad, J. Monk, W. Pokorski, T. Przedzinski, A. Verbytskyi, The HepMC3 Event Record Library for Monte Carlo Event Generators, Computer Physics Communications 260 (2021) 107310. doi:10.1016/j.cpc.2020.107310.

[49] A. Buckley, J. Butterworth, D. Grellscheid, H. Hoeth, L. Lönnblad, J. Monk, H. Schulz, F. Siegert, Rivet User Manual, Computer Physics Communications 184 (12) (2013) 2803–2819. doi:10.1016/j.cpc.2013.05.021.

[50] C. Bierlich, et al., Robust Independent Validation of Experiment and Theory: Rivet version 3, SciPost Physics 8 (2) (Feb. 2020). doi:10.21468/scipostphys.8.2.026.

[51] C. Bierlich, A. Buckley, J. Butterworth, C. Gutschow, L. Lonnblad, T. Procter, P. Richardson, Y. Yeh, Robust Independent Validation of Experiment and Theory: Rivet Version 4 Release Note (2024). arXiv:2404.15984.

[52] E. Maguire, L. Heinrich, G. Watt, HEPData: a Repository for High Energy Physics Data, Journal of Physics: Conference Series 898 (2017) 102006. doi:10.1088/1742-6596/898/10/102006.

[53] E. Conte, B. Fuks, G. Serret, MadAnalysis5, a User-friendly Framework for Collider Phenomenology, Computer Physics Communications 184 (1) (2013) 222–256. doi:10.1016/j.cpc.2012.09.009.

[54] S. Ovyn, X. Rouby, V. Lemaitre, Delphes, a Framework for Fast Simulation of a Generic Collider Experiment (2010). arXiv:0903.2225.

[55] R. Brun, et al., root-project/root: v6.18/02 (August 2019). doi:10.5281/zenodo.3895860.

[56] M. Cirelli, A. Strumia, J. Zupan, Dark Matter (2024). arXiv:2406.01705.

[57] D. Huterer, D. L. Shafer, Dark Energy Two Decades After: Observables, Probes, Consistency Tests, Reports on Progress in Physics 81 (1) (2017) 016901. doi:10.1088/1361-6633/aa997e.

[58] M. E. Peskin, What is the Hierarchy Problem? (2025). arXiv:2505.00694.

[59] N. Arkani–Hamed, S. Dimopoulos, G. Dvali, The Hierarchy Problem and New Dimensions at a Millimeter, Physics Letters B 429 (3–4) (1998) 263–272. doi:10.1016/s0370-2693(98)00466-3.

[60] M. J. Dugan, H. Georgi, D. B. Kaplan, Anatomy of a Composite Higgs Model, Nucl. Phys. B 254 (1985) 299–326. doi:10.1016/0550-3213(85)90221-4.

[61] R. Contino, Tasi 2009 Lectures: The Higgs as a Composite Nambu-Goldstone Boson (2010). arXiv:1005.4269.

[62] A. Arbey, F. Mahmoudi, Dark Matter and the Early Universe: A Review, Progress in Particle and Nuclear Physics 119 (2021) 103865. doi:10.1016/j.ppnp.2021.103865.

[63] A. G. Riess, et al., Observational Evidence from Supernovae for an Accelerating Universe and a Cosmological Constant, The Astronomical Journal 116 (3) (1998) 1009–1038. doi:10.1086/300499.

[64] S. Perlmutter, et al., Measurements of Ω and Λ from 42 High-Redshift Supernovae, The Astrophysical Journal 517 (2) (1999) 565–586. doi:10.1086/307221.

[65] S. Dodelson, K. Honscheid, K. Abazajian, J. Carlstrom, D. Huterer, B. Jain, A. Kim, D. Kirkby, A. Lee, N. Padmanabhan, J. Rhodes, D. Weinberg, Dark Energy and CMB (2013). arXiv:1309.5386.

[66] J. A. S. Lima, J. V. Cunha, J. S. Alcaniz, Constraining the Dark Energy with Galaxy Cluster X-Ray Data, Physical Review D 68 (2) (Jul. 2003). doi:10.1103/physrevd.68.023510.

[67] D. Huterer, Weak Lensing, Dark Matter and Dark Energy, General Relativity and Gravitation 42 (9) (2010) 2177–2195. doi:10.1007/s10714-010-1051-z.

[68] DESI Collaboration, Data Release 1 of the Dark Energy Spectroscopic Instrument (2025). arXiv:2503.14745.

[69] DESI Collaboration, DESI DR2 Results I: Baryon Acoustic Oscillations from the Lyman Alpha Forest (2025). arXiv:2503.14739.

[70] DESI Collaboration, DESI DR2 Results II: Measurements of Baryon Acoustic Oscillations and Cosmological Constraints (2025). arXiv:2503.14738.

[71] JWST, Webb's First Deep Field (NIRCam Image).
URL https://shorturl.at/qWUDy

[72] Chandra X-ray Observatory, Image of the Bullet Cluster (1E 0657-56), image taken from https://chandra.harvard.edu/photo/2006/1e0657/.

[73] D. Clowe, M. Bradač, A. H. Gonzalez, M. Markevitch, S. W. Randall, C. Jones, D. Zaritsky, A Direct Empirical Proof of the Existence of Dark Matter, The Astrophysical Journal 648 (2) (2006) L109–L113. doi:10.1086/508162.

[74] O. Baker, et al., Particle Physics of the Dark Sector, Symmetry 14 (11) (2022) 2238. doi:10.3390/sym14112238.

[75] CMS Collaboration, Dark Sector Searches with the CMS Experiment, Physics Reports (2025) 448–569doi:10.1016/j.physrep.2024.09.013.

[76] J. Abdallah, et al., Simplified Models for Dark Matter Searches at the LHC, Physics of the Dark Universe 9–10 (2015) 8–23. doi:10.1016/j.dark.2015.08.001.

[77] M. Fabbrichesi, E. Gabrielli, G. Lanfranchi, The Physics of the Dark Photon: A Primer, Springer International Publishing, 2021. doi:10.1007/978-3-030-62519-1.

[78] C. Arina, B. Fuks, L. Mantani, A Universal Framework for t-Channel Dark Matter Models, The European Physical Journal C 80 (5) (May 2020). doi:10.1140/epjc/s10052-020-7933-7.

[79] A. M. Abdullahi, et al., The Present and Future Status of Heavy Neutral Leptons, Journal of Physics G: Nuclear and Particle Physics 50 (2) (2023) 020501. doi:10.1088/1361-6471/ac98f9.

[80] Y. Hochberg, E. Kuflik, R. McGehee, H. Murayama, K. Schutz, Strongly Interacting Massive Particles through the Axion Portal, Physical Review D 98 (11) (Dec. 2018). doi:10.1103/physrevd.98.115031.

[81] M. J. Strassler, K. M. Zurek, Echoes of a Hidden Valley at Hadron Colliders, Physics Letters B 651 (5–6) (2007) 374–379. doi:10.1016/j.physletb.2007.06.055.

[82] CMS Collaboration, Search for Soft Unclustered Energy Patterns in Proton-Proton Collisions at 13 TeV, Phys. Rev. Lett. 133 (19) (2024) 191902. arXiv:2403.05311, doi:10.1103/PhysRevLett.133.191902.

[83] S. Argyropoulos, U. Haisch, Benchmarking LHC Searches for Light 2HDM+**a** Pseudoscalars (2022). arXiv:2202.12631.

[84] G. Branco, P. Ferreira, L. Lavoura, M. Rebelo, M. Sher, J. P. Silva, Theory and Phenomenology of Two-Higgs-doublet Models, Physics Reports 516 (1–2) (2012) 1–102. doi:10.1016/j.physrep.2012.02.002.

[85] CMS Collaboration, Search for Dark Matter Produced in Association with a Higgs Boson Decaying to a Pair of Bottom Quarks in Proton–proton Collisions at $\sqrt{s} =$ 13 TeV, The European Physical Journal C 79 (3) (Mar. 2019). doi:10.1140/epjc/s10052-019-6730-7.

[86] G. Jungman, M. Kamionkowski, K. Griest, Supersymmetric Dark Matter, Physics Reports 267 (5–6) (1996) 195–373. doi:10.1016/0370-1573(95)00058-5.

[87] J. Fan, M. Reece, J. T. Ruderman, Stealth Supersymmetry, Journal of High Energy Physics 2011 (11) (Nov. 2011). doi:10.1007/jhep11(2011)012.

[88] E. Izaguirre, G. Krnjaic, B. Shuve, Discovering Inelastic Thermal Relic Dark Matter at Colliders, Physical Review D 93 (6) (Mar. 2016). doi:10.1103/physrevd.93.063523.

[89] A. Alloul, N. D. Christensen, C. Degrande, C. Duhr, B. Fuks, FeynRules 2.0 - A Complete Toolbox for Tree-level Phenomenology, Computer Physics Communications 185 (8) (2014) 2250–2300. doi:10.1016/j.cpc.2014.04.012.

[90] C. Degrande, C. Duhr, B. Fuks, D. Grellscheid, O. Mattelaer, T. Reiter, UFO – The Universal FeynRules Output, Computer Physics Communications 183 (6) (2012) 1201–1214. doi:10.1016/j.cpc.2012.01.022.

[91] L. Carloni, T. Sjöstrand, Visible Effects of Invisible Hidden Valley Radiation, Journal of High Energy Physics 2010 (9) (Sep. 2010). doi:10.1007/jhep09(2010)105.

[92] L. Carloni, J. Rathsman, T. Sjöstrand, Discerning Secluded Sector Gauge Structures, Journal of High Energy Physics 2011 (4) (Apr. 2011). doi:10.1007/jhep04(2011)091.

[93] J. M. Butterworth, D. Grellscheid, M. Krämer, B. Sarrazin, D. Yallup, Constraining New Physics with Collider Measurements of Standard Model Signatures, Journal of High Energy Physics 2017 (3) (Mar. 2017). doi:10.1007/jhep03(2017)078.

[94] A. Buckley, et al., Testing New Physics Models with Global Comparisons to Collider Measurements: the CONTUR Toolkit, SciPost Physics Core 4 (2) (May 2021). doi:10.21468/scipostphyscore.4.2.013.

[95] A. L. Read, Presentation of Search Results: the CLs Technique, Journal of Physics G: Nuclear and Particle Physics 28 (10) (2002) 2693. doi:10.1088/0954-3899/28/10/313.

[96] T. Junk, Confidence Level Computation for Combining Searches with Small Statistics, Nuclear Instruments and Methods in Physics Research Section A: Accelerators, Spectrometers, Detectors and Associated Equipment 434 (2–3) (1999) 435–443. doi:10.1016/s0168-9002(99)00498-2.

[97] J. Y. Araz, B. Fuks, G. Polykratis, Simplified Fast Detector Simulation in MadAnalysis5, The European Physical Journal C 81 (4) (Apr. 2021). doi:10.1140/epjc/s10052-021-09052-5.

[98] E. Conte, B. Dumont, B. Fuks, C. Wymant, Designing and Recasting LHC Analyses with MadAnalysis5, The European Physical Journal C 74 (10) (Oct. 2014). doi:10.1140/epjc/s10052-014-3103-0.

[99] E. Mobs, The CERN accelerator complex in 2019General Photo (2019).
URL https://cds.cern.ch/record/2684277

[100] G. Strong, ATLAS Coordinate System, image compiled from code made available under CC BY-SA 4.0 by Izaak Neutelings, modified version available at https://github.com/GilesStrong/cc_by_sa_4/blob/master/atlas_coord_system.tex.

[101] ATLAS Collaboration, The ATLAS Experiment at the CERN Large Hadron Collider: a Description of the Detector Configuration for Run 3, Journal of Instrumentation 19 (05) (May 2024). doi:10.1088/1748-0221/19/05/p05063.

[102] R. M. Bianchi, A. Collaboration, ATLAS Experiment Schematic or Layout Illustration, general Photo (2022).
URL https://cds.cern.ch/record/2837191

[103] ATLAS Collaboration, The ATLAS Trigger System for LHC Run 3 and Trigger Performance in 2022, Journal of Instrumentation 19 (06) (Jun. 2024). doi:10.1088/1748-0221/19/06/p06029.

[104] ATLAS collaboration, Operation of the ATLAS Trigger System in Run 2, Journal of Instrumentation 15 (10) (2020) P10004–P10004. doi:10.1088/1748-0221/15/10/p10004.

[105] ATLAS Collaboration, Athena, Version 22.0.1 (Apr. 2019). doi:10.5281/zenodo.2641997.

[106] M. Elsing, M. Goossens, A. Nairz, G. Negri, The ATLAS Tier-0: Overview and Operational Experience, J. Phys.: Conf. Ser. 219 (2010) 072011. doi:10.1088/1742-6596/219/7/072011.

[107] S. D. Ellis, D. E. Soper, Successive Combination Jet Algorithm for Hadron Collisions, Physical Review D 48 (7) (1993) 3160–3166. doi:10.1103/physrevd.48.3160.

[108] M. Cacciari, G. P. Salam, G. Soyez, The Anti-KT Jet Clustering Algorithm, Journal of High Energy Physics 2008 (04) (2008) 063–063. doi:10.1088/1126-6708/2008/04/063.

[109] Y. Dokshitzer, G. Leder, S. Moretti, B. Webber, Better Jet Clustering Algorithms, Journal of High Energy Physics 1997 (08) (1997) 001–001. doi:10.1088/1126-6708/1997/08/001.

[110] ATLAS Collaboration, Optimisation of Large-radius Jet Reconstruction for the ATLAS Detector in 13 TeV Proton–Proton Collisions, The European Physical Journal C 81 (4) (Apr. 2021). doi:10.1140/epjc/s10052-021-09054-3.

[111] Early Inner Detector Tracking Performance in the 2015 data at $\sqrt{s} = 13$ TeV, Tech. rep., CERN, Geneva, all figures including auxiliary figures are available at https://atlas.web.cern.ch/Atlas/GROUPS/PHYSICS/PUBNOTES/ATL-PHYS-PUB-2015-051 (2015).

[112] ATLAS Collaboration, Topological Cell Clustering in the ATLAS Calorimeters and its Performance in LHC Run 1, The European Physical Journal C 77 (7) (Jul. 2017). doi:10.1140/epjc/s10052-017-5004-5.

[113] ATLAS Collaboration, ATLAS Event Display: Multijet Event, General Photo (2023). URL https://cds.cern.ch/record/2865016

[114] ATLAS Collaboration, Electron and Photon Efficiencies in LHC Run 2 with the ATLAS Experiment, Journal of High Energy Physics 2024 (5) (May 2024). doi:10.1007/jhep05(2024)162.

[115] ATLAS Collaboration, Electron Reconstruction and Identification in the ATLAS Experiment Using the 2015 and 2016 LHC Proton-proton Collision Data at $\sqrt{s} = 13$ TeV, Eur. Phys. J. C 79 (8) (2019) 639. arXiv:1902.04655, doi:10.1140/epjc/s10052-019-7140-6.

[116] ATLAS Collaboration, Studies of the Muon Momentum Calibration and Performance of the ATLAS Detector with *pp* Collisions at $\sqrt{s} = 13$TeV, The European Physical Journal C 83 (8) (Aug. 2023). doi:10.1140/epjc/s10052-023-11584-x.

[117] S. Mehlhase, ATLAS Detector Slice and Particle Visualisations (2021). URL https://cds.cern.ch/record/2770815

[118] ATLAS Collaboration, Trigger monitoring and rate predictions using Enhanced Bias data from the ATLAS Detector at the LHC, Tech. rep., CERN, Geneva (2016). URL https://cds.cern.ch/record/2223498

[119] ATLAS Collaboration, The ATLAS Inner Detector Trigger Performance in pp Collisions at 13 TeV during LHC Run 2, The European Physical Journal C 82 (3) (Mar. 2022). doi:10.1140/epjc/s10052-021-09920-0.

[120] J. H. Kim, S. D. Lane, H.-S. Lee, I. M. Lewis, M. Sullivan, Searching for Dark Photons with Maverick Top Partners, Physical Review D 101 (3) (Feb. 2020). doi:10.1103/physrevd.101.035041.

[121] K. du Plessis, M. M. Flores, D. Kar, S. Sinha, H. van der Schyf, Hitting two BSM Particles with One Lepton-Jet: Search for a Top Partner Decaying to a Dark Photon, Resulting in a Lepton-Jet, SciPost Physics 13 (2) (Aug. 2022). doi:10.21468/scipostphys.13.2.018.

[122] G. C. Branco, M. N. Rebelo, Vector-like Quarks (2022). arXiv:2208.07235.

[123] P. Ramond, Fermions in the Desert, in: Europhysics Study Conference: Unification of Fundamental Interactions II:, 1981, p. 467.

[124] M. Buchkremer, G. Cacciapaglia, A. Deandrea, L. Panizzi, Model-independent Framework for Searches of Top Partners, Nuclear Physics B 876 (2) (2013) 376–417. doi:10.1016/j.nuclphysb.2013.08.010.

[125] J. Erdmann, Overview of Searches for Single Production of Vector-like Top and Bottom Quarks with the ATLAS Experiment at 13 TeV (2018). arXiv:1811.11496.

[126] A. Cagnotta, VLQ Searches and Hadronic Final States at the CMS Experiment, PoS LHCP2023 (2024) 154. doi:10.22323/1.450.0154.

[127] ATLAS Collaboration, Search for Dark Photons in Rare Z Boson Decays with the ATLAS Detector, Physical Review Letters 131 (25) (Dec. 2023). doi:10.1103/physrevlett.131.251801.

[128] ATLAS Collaboration, Search for Light Neutral Particles Decaying Promptly into Collimated Pairs of Electrons or Muons in pp Collisions at $\sqrt{s} = 13$ TeV with the ATLAS Detector, The European Physical Journal C 85 (3) (Mar. 2025). doi:10.1140/epjc/s10052-025-13916-5.

[129] LHCb Collaboration, Search for Dark Photons Produced in 13 TeV Collisions, Physical Review Letters 120 (6) (Feb. 2018). doi:10.1103/physrevlett.120.061801.

[130] LHCb Collaboration, Search for $A' \to \mu^+\mu^-$ Decays, Physical Review Letters 124 (4) (Jan. 2020). doi:10.1103/physrevlett.124.041801.

[131] CMS Collaboration, Search for a Narrow Resonance Lighter than 200 GeV Decaying to a Pair of Muons in Proton-Proton Collisions at 13 TeV, Physical Review Letters 124 (13) (Apr. 2020). doi:10.1103/physrevlett.124.131802.

[132] T. G. Rizzo, Kinetic Mixing and Portal Matter Phenomenology, Physical Review D 99 (11) (Jun. 2019). doi:10.1103/physrevd.99.115024.

[133] N. Arkani-Hamed, N. Weiner, LHC Signals for a SuperUnified Theory of Dark Matter, Journal of High Energy Physics 2008 (12) (2008) 104–104. doi:10.1088/1126-6708/2008/12/104.

[134] ATLAS Collaboration, A Search for Prompt Lepton-jets in pp Collisions at $\sqrt{s} = 8$ TeV with the ATLAS Detector, Journal of High Energy Physics 2016 (2) (Feb. 2016). doi:10.1007/jhep02(2016)062.

[135] ATLAS Collaboration, Performance of the ATLAS Muon Triggers in Run 2, JINST 15 (09) (2020) P09015. arXiv:2004.13447, doi:10.1088/1748-0221/15/09/p09015.

[136] R. D. Ball, V. Bertone, S. Carrazza, L. Del Debbio, S. Forte, A. Guffanti, N. P. Hartland, J. Rojo, Parton Distributions with QED Corrections, Nuclear Physics B 877 (2) (2013) 290–320. doi:10.1016/j.nuclphysb.2013.10.010.

[137] ATLAS Collaboration, ATLAS Pythia 8 Tunes to 7 TeV Data, Tech. rep., CERN, Geneva, https://cds.cern.ch/record/1966419 (2014).

[138] S. Frixione, G. Ridolfi, P. Nason, A positive-weight next-to-leading-order monte carlo for heavy flavour hadroproduction, Journal of High Energy Physics 2007 (09) (2007) 126–126. doi:10.1088/1126-6708/2007/09/126.

[139] P. Nason, A New Method for Combining NLO QCD with Shower Monte Carlo Algorithms, Journal of High Energy Physics 2004 (11) (2004) 040–040. doi:10.1088/1126-6708/2004/11/040.

[140] S. Frixione, P. Nason, C. Oleari, Matching NLO QCD Computations with Parton Shower Simulations: the POWHEG Method, Journal of High Energy Physics 2007 (11) (2007) 070–070. doi:10.1088/1126-6708/2007/11/070.

[141] S. Alioli, P. Nason, C. Oleari, E. Re, A General Framework for Implementing NLO Calculations in Shower Monte Carlo Programs: the POWHEG BOX, Journal of High Energy Physics 2010 (6) (Jun. 2010). doi:10.1007/jhep06(2010)043.

[142] Studies on Top-quark Monte Carlo Modelling for Top2016, Tech. rep., CERN, Geneva, all figures including auxiliary figures are available at https://atlas.web.cern.ch/Atlas/GROUPS/PHYSICS/PUBNOTES/ATL-PHYS-PUB-2016-020 (2016).

[143] R. D. Ball, V. Bertone, S. Carrazza, C. S. Deans, L. Del Debbio, S. Forte, A. Guffanti, N. P. Hartland, J. I. Latorre, J. Rojo, M. Ubiali, Parton distributions for the lhc run 2, Journal of High Energy Physics 2015 (4) (Apr. 2015). doi:10.1007/jhep04(2015)040.

[144] T. Sjöstrand, S. Ask, J. R. Christiansen, R. Corke, N. Desai, P. Ilten, S. Mrenna, S. Prestel, C. O. Rasmussen, P. Z. Skands, An Introduction to PYTHIA 8.2, Computer Physics Communications 191 (2015) 159–177. doi:10.1016/j.cpc.2015.01.024.

[145] E. Bothmann, G. Singh Chahal, S. Höche, J. Krause, F. Krauss, S. Kuttimalai, S. Liebschner, D. Napoletano, M. Schönherr, H. Schulz, S. Schumann, F. Siegert, Event Generation with Sherpa 2.2, SciPost Physics 7 (3) (Sep. 2019). doi:10.21468/scipostphys.7.3.034.

[146] S. Schumann, F. Krauss, A Parton Shower Algorithm based on Catani-Seymour Dipole Factorisation, Journal of High Energy Physics 2008 (03) (2008) 038–038. doi:10.1088/1126-6708/2008/03/038.

[147] C. Anastasiou, L. Dixon, K. Melnikov, F. Petriello, High-precision QCD at Hadron Colliders: Electroweak Gauge Boson Rapidity Distributions at Next-to-next-to Leading Order, Physical Review D 69 (9) (May 2004). doi:10.1103/physrevd.69.094008.

[148] S. Agostinelli, et al., GEANT4 - A Simulation Toolkit, Nucl. Instrum. Meth. A 506 (2003) 250–303. doi:10.1016/S0168-9002(03)01368-8.

[149] ATLAS Collaboration, The ATLAS Simulation Infrastructure, Eur. Phys. J. C 70 (2010) 823–874. arXiv:1005.4568, doi:10.1140/epjc/s10052-010-1429-9.

[150] ATLAS Collaboration, Muon Reconstruction and Identification Efficiency in ATLAS Using the Full Run 2 *pp* Collision Data Set at $\sqrt{s} = 13$ TeV, Eur. Phys. J. C 81 (7) (2021) 578. arXiv:2012.00578, doi:10.1140/epjc/s10052-021-09233-2.

[151] J. Alwall, P. C. Schuster, N. Toro, Simplified Models for a First Characterization of New Physics at the LHC, Physical Review D 79 (7) (Apr. 2009). doi:10.1103/physrevd.79.075020.

[152] D. Alves, N. Arkani-Hamed, et al., Simplified Models for LHC New Physics Searches, Journal of Physics G: Nuclear and Particle Physics 39 (10) (2012) 105005. doi:10.1088/0954-3899/39/10/105005.

[153] C. Arina, B. Fuks, et al., t-Channel Dark Matter at the LHC (2025). arXiv:2504.10597.

[154] S. Colucci, B. Fuks, F. Giacchino, L. L. Honorez, M. H. Tytgat, J. Vandecasteele, Top-philic Vectorlike Portal to Scalar Dark Matter, Physical Review D 98 (3) (Aug. 2018). doi:10.1103/physrevd.98.035002.

[155] A. S. Cornell, A. Deandrea, T. Flacke, B. Fuks, L. Mason, Contact interactions and top-philic scalar dark matter, Journal of High Energy Physics 2021 (7) (Jul. 2021). doi:10.1007/jhep07(2021)026.

[156] A. S. Cornell, A. Deandrea, T. Flacke, B. Fuks, L. Mason, Top Partners and Scalar Dark Matter: A Nonminimal Reappraisal, Physical Review D 107 (7) (Apr. 2023). doi:10.1103/physrevd.107.075004.

[157] C. Arina, B. Fuks, L. Mantani, A Universal Framework for t-Channel Dark Matter Models, The European Physical Journal C 80 (5) (May 2020). doi:10.1140/epjc/s10052-020-7933-7.

[158] D. B. Kaplan, Flavor at SSC Energies: A New Mechanism for Dynamically Generated Fermion Masses, Nucl. Phys. B 365 (1991) 259–278. doi:10.1016/S0550-3213(05)80021-5.

[159] A. Belyaev, R. S. Chivukula, B. Fuks, E. H. Simmons, X. Wang, Vector-like Top Quark Production via a Chromomagnetic Moment at the LHC, Physical Review D 104 (9) (Nov. 2021). doi:10.1103/physrevd.104.095024.

[160] S. Frixione, B. Fuks, V. Hirschi, K. Mawatari, H.-S. Shao, M. P. A. Sunder, M. Zaro, Automated Simulations Beyond the Standard Model: Supersymmetry, Journal of High Energy Physics 2019 (12) (Dec. 2019). doi:10.1007/jhep12(2019)008.

[161] P. Artoisenet, R. Frederix, O. Mattelaer, R. Rietkerk, Automatic Spin-entangled Decays of Heavy Resonances in Monte Carlo Simulations, Journal of High Energy Physics 2013 (3) (Mar. 2013). doi:10.1007/jhep03(2013)015.

[162] J. Alwall, C. Duhr, B. Fuks, O. Mattelaer, D. G. Öztürk, C.-H. Shen, Computing Decay Rates for New Physics Theories with FeynRules and MadGraph 5_a*MC@NLO*, Computer Physics Communications 197 (2015) 312–323. doi:10.1016/j.cpc.2015.08.031. URL http://dx.doi.org/10.1016/j.cpc.2015.08.031

[163] S. Frixione, B. R. Webber, Matching NLO QCD Computations and Parton Shower Simulations, Journal of High Energy Physics 2002 (06) (2002) 029–029. doi:10.1088/1126-6708/2002/06/029.

[164] ATLAS Collaboration, Differential Cross-sections for Events with Missing Transverse Momentum and Jets Measured with the ATLAS Detector in 13 TeV Proton-proton Collisions, JHEP 08 (2024) 223. arXiv:2403.02793, doi:10.1007/JHEP08(2024)223.

[165] ATLAS Collaboration, Measurements of $t\bar{t}$ Differential Cross-sections of Highly Boosted Top Quarks Decaying to All-hadronic Final States in pp Collisions at $\sqrt{s} = 13$ TeV using the ATLAS Detector, Phys. Rev. D 98 (1) (2018) 012003. arXiv:1801.02052, doi:10.1103/PhysRevD.98.012003.

[166] ATLAS Collaboration, Measurements of Top-quark Pair, Single- and Double-differential Cross-sections in the All-hadronic Channel in pp Collisions at $\sqrt{s} = 13$ TeV using the ATLAS Detector, Journal of High Energy Physics 2021 (1) (Jan. 2021). doi:10.1007/jhep01(2021)033.

[167] ATLAS Collaboration, Differential $t\bar{t}$ Cross-section Measurements using Boosted Top Quarks in the All-hadronic Final State with 139 fb^1 of ATLAS Data, Journal of High Energy Physics 2023 (4) (Apr. 2023). doi:10.1007/jhep04(2023)080.

[168] CMS Collaboration, Measurement of Differential Cross Sections and Charge Ratios for t-Channel Single Top Quark Production in Proton–proton Collisions at $\sqrt{s} = 13$ TeV, The European Physical Journal C 80 (5) (May 2020). doi:10.1140/epjc/s10052-020-7858-1.

[169] CMS Collaboration, Measurement of Differential Cross Sections for the Production of Top Quark Pairs and of Additional Jets in Events from Collisions at $\sqrt{s} = 13$ TeV, Physical Review D 97 (11) (Jun. 2018). doi:10.1103/physrevd.97.112003.

[170] ATLAS Collaboration, Search for Squarks and Gluinos in Final States with Jets and Missing Transverse Momentum Using 139 fb^1 of $\sqrt{s} = 13$ TeV pp Collision Data with the ATLAS Detector, Journal of High Energy Physics 2021 (2) (Feb. 2021). doi:10.1007/jhep02(2021)143.

[171] CMS Collaboration, Search for New Particles in Events with Energetic Jets and Large Missing Transverse Momentum in Proton-proton Collisions at $\sqrt{s} = 13$ TeV, Journal of High Energy Physics 2021 (11) (Nov. 2021). doi:10.1007/jhep11(2021)153.

[172] G. Albouy, et al., Theory, Phenomenology, and Experimental Avenues for Dark Showers: a Snowmass 2021 Report, The European Physical Journal C 82 (12) (Dec. 2022). doi:10.1140/epjc/s10052-022-11048-8.

[173] S. Knapen, J. Shelton, D. Xu, Perturbative Benchmark Models for a Dark Shower Search Program, Physical Review D 103 (11) (Jun. 2021). doi:10.1103/physrevd.103.115013.

[174] T. Cohen, M. Lisanti, H. K. Lou, S. Mishra-Sharma, LHC Searches for Dark Sector Showers, Journal of High Energy Physics 2017 (11) (Nov. 2017). doi:10.1007/jhep11(2017)196.

[175] P. Schwaller, D. Stolarski, A. Weiler, Emerging Jets, Journal of High Energy Physics 2015 (5) (May 2015). doi:10.1007/jhep05(2015)059.

[176] CMS Collaboration, Search for Dark-QCD with Emerging Jets in Proton-proton Collisions at $\sqrt{s} = 13$ TeV, Journal of High Energy Physics 2024 (7) (Jul. 2024). doi:10.1007/jhep07(2024)142.

[177] ATLAS Collaboration, Search for Emerging Jets in pp Collisions at $\sqrt{s} = 13.6$ TeV with the ATLAS Experiment (May 2025). arXiv:2505.02429.

[178] ATLAS Collaboration, Search for Resonant Production of Dark Quarks in the Di-jet Final State with the ATLAS Detector, Journal of High Energy Physics 2024 (2) (Feb. 2024). doi:10.1007/jhep02(2024)128.

[179] M. Park, M. Zhang, Tagging a Jet from a Dark Sector with Jet Substructures at Colliders, Physical Review D 100 (11) (Dec. 2019). doi:10.1103/physrevd.100.115009.

[180] T. Cohen, M. Lisanti, H. K. Lou, Semi-Visible Jets: Dark Matter Undercover at the LHC, Physical Review Letters 115 (17) (Oct. 2015). doi:10.1103/physrevlett.115.171804.

[181] ATLAS Collaboration, Search for Non-resonant Production of Semi-Visible Jets using Run 2 Data in ATLAS, Physics Letters B 848 (2024) 138324. doi:10.1016/j.physletb.2023.138324.

[182] CMS Collaboration, Search for Resonant Production of Strongly Coupled Dark Matter in Proton-proton Collisions at 13 TeV, Journal of High Energy Physics 2022 (6) (Jun. 2022). doi:10.1007/jhep06(2022)156.

[183] T. Cohen, J. Doss, M. Freytsis, Jet Substructure from Dark Sector Showers, Journal of High Energy Physics 2020 (9) (Sep. 2020). doi:10.1007/jhep09(2020)118.

[184] D. Kar, S. Sinha, Exploring Jet Substructure in Semi-Visible Jets, SciPost Physics 10 (4) (Apr. 2021). doi:10.21468/scipostphys.10.4.084.

[185] T. Cohen, J. Roloff, C. Scherb, Dark Sector Showers in the Lund Jet Plane, Physical Review D 108 (3) (Aug. 2023). doi:10.1103/physrevd.108.l031501.

[186] E. Bernreuther, T. Finke, F. Kahlhoefer, M. Krämer, A. Mück, Casting a Graph Net to Catch Dark Showers, SciPost Physics 10 (2) (Feb. 2021). doi:10.21468/scipostphys.10.2.046.

[187] F. Canelli, A. de Cosa, L. Le Pottier, J. Niedziela, K. Pedro, M. Pierini, autoencoders for semi-visible jet detection, Journal of High Energy Physics 2022 (2) (Feb. 2022). doi:10.1007/jhep02(2022)074.

[188] T. Faucett, S.-C. Hsu, D. Whiteson, Learning to Identify Semi-Visible Jets, Journal of High Energy Physics 2022 (12) (Dec. 2022). doi:10.1007/jhep12(2022)132.

[189] T. Finke, M. Krämer, M. Lipp, A. Mück, Boosting Mono-jet Searches with Model-agnostic Machine Learning, Journal of High Energy Physics 2022 (8) (Aug. 2022). doi:10.1007/jhep08(2022)015.

[190] K. Pedro, P. Shyamsundar, Optimal Mass Variables for Semivisible Jets (2023). arXiv:2303.16253.

[191] A. Bhardwaj, C. Englert, W. Naskar, V. S. Ngairangbam, M. Spannowsky, Equivariant, Safe and Sensitive — Graph Networks for New Physics, Journal of High Energy Physics 2024 (7) (Jul. 2024). doi:10.1007/jhep07(2024)245.

[192] B. Liu, K. Pedro, Semi-Visible Jets + X: Illuminating Dark Showers with Radiation, Journal of High Energy Physics 2024 (12) (Dec. 2024). doi:10.1007/jhep12(2024)105.

[193] D. Kar, W. Nzuza, S. Sinha, 2B or not 2B, a Study of Bottom-quark-philic Semi-Visible Jets, SciPost Physics Core 7 (4) (Nov. 2024). doi:10.21468/scipostphyscore.7.4.071.

[194] A. Batz, T. Cohen, D. Curtin, C. Gemmell, G. D. Kribs, Dark Sector Glueballs at the LHC, Journal of High Energy Physics 2024 (4) (Apr. 2024). doi:10.1007/jhep04(2024)070.

[195] C. Cazzaniga, A. de Cosa, Leptons Lurking in Semi-Visible Jets at the LHC, The European Physical Journal C 82 (9) (Sep. 2022). doi:10.1140/epjc/s10052-022-10775-2.

[196] H. Beauchesne, C. Cazzaniga, A. de Cosa, C. Doglioni, T. Fitschen, G. G. di Cortona, Z. Zhou, Uncovering Tau Leptons-enriched Semi-Visible Jets at the LHC, The European Physical Journal C 83 (7) (Jul. 2023). doi:10.1140/epjc/s10052-023-11775-6.

[197] C. Cazzaniga, A. Russo, E. Sitti, A. de Cosa, Phenomenology of Photons-enriched Semi-Visible Jets (2024). arXiv:2407.08276.

[198] J. Butterworth, C. Cazzaniga, A. Garcia-Bellido, D. Kar, S. Kulkarni, P. Schwaller, S. Sinha, D. Wilson-Edwards, J. Zurita, Mitp colours in darkness workshop summary report (2023). arXiv:2311.16330.

[199] s-Channel DM Model, https://github.com/smsharma/SemivisibleJets, commit 4e606c4.

[200] ATLAS Collaboration, Differential cross-sections for events with missing transverse momentum and jets measured with the atlas detector in 13 tev proton-proton collisions, Journal of High Energy Physics 2024 (8) (Aug. 2024). doi:10.1007/jhep08(2024)223.

[201] M. L. Mangano, M. Moretti, F. Piccinini, M. Treccani, Matching Matrix Elements and Shower Evolution for Top-pair Production in Hadronic Collisions, Journal of High Energy Physics 2007 (01) (2007) 013–013. doi:10.1088/1126-6708/2007/01/013.